UNIVERSIDADE DE LISBOA
FACULDADE DE CIÊNCIAS
DEPARTAMENTO DE ENGENHARIA GEOGRÁFICA, GEOFÍSICA E ENERGIA

Numerical analysis of cross-ventilation in generic isolated building configurations

João Maria Bravo Vieira Dias

Dissertação de Mestrado Integrado em Engenharia da Energia e do Ambiente

2015

UNIVERSIDADE DE LISBOA
FACULDADE DE CIÊNCIAS
DEPARTAMENTO DE ENGENHARIA GEOGRÁFICA, GEOFÍSICA E ENERGIA

Numerical analysis of cross-ventilation in generic isolated building configurations

João Maria Bravo Vieira Dias

Dissertação de Mestrado Integrado em Engenharia da Energia e do Ambiente

Trabalho realizado sob a supervisão de

Prof. Dr. Ir. Bert Blocken (TU/e)

Prof. Dr. Ir. Guilherme Carrilho da Graça (FCUL)

2015

Abstract

This thesis presents a numerical analysis of cross-ventilation in generic isolated building configurations. This study focuses on understanding how cross-ventilation is affected by changing the length of the building, the number of partitions and the position of the partition opening for a generic building configuration. Firstly the depth of the building was changed (2.5, 5 and 10 times the building height) and it was found that the volume flow rate through the inlet opening was constant, the air exchange rate decreased proportionally with the building depth, the CO_2 concentration and the mean age of air increased with the building depth. The air exchange efficiency was higher in the deepest building and, for this particular case, cross-ventilation was efficient for a building depth ten times the building height. Secondly three different buildings with a partition wall and a door opening were tested for two different building depths. It was concluded that the geometries where the door opening was located close to the side wall (not in front of the inlet/outlet openings) outperformed the other different geometries (including the cases without partition) in terms of mean age of air, CO_2 concentration, volume flow rate, air exchange rate and air exchange efficiency.

Keywords: CFD; Cross-ventilation; Natural ventilation;

Resumo

Esta dissertação apresenta uma análise numérica de ventilação cruzada em diferentes configurações de um edifício genérico e isolado. Este estudo foca-se em perceber como é que a ventilação cruzada é afectada pela alteração do comprimento do edifício, pelo número de partições e pela posição da abertura entre diferentes partições. Primeiramente, a profundidade do edifício foi alterada (para 2.5, 5 e 10 vezes a altura do edifício) e descobriu-se que o caudal de entrada na abertura a montante do edifício é constante, a renovação de ar decresceu proporcionalmente com o aumento do comprimento do edifício, enquanto a concentração de CO_2 e a idade média do ar aumentaram com o aumento do comprimento do edifício. A eficiência de renovação do ar foi mais elevada nos edifícios mais compridos e, para este caso em particular, a ventilação cruzada foi eficaz num edifício com o comprimento igual a dez vezes a sua altura. Em segundo lugar acrescentou-se à geometria anterior uma parede com uma abertura equiavalente a uma porta, em que ambas mudam de posição, e que divide o espaço interior em dois. Três geometrias foram testadas para dois comprimentos do edifício (padrão e 2.5 vezes a altura do edifício). Foi possível concluir que nos edifícios em que a abertura entre as duas divisões está colocada perto da parede lateral do edifício (não estando na direcção da abertura de entrada/saída do ar exterior) melhores resultados foram obtidos quando comparados com as outras geometrias (incluindo os casos sem partição) em relação à idade média do ar, concentração de CO_2, caudal de entrada de ar, renovação de ar e eficiência de renovação de ar.

Palavras-chave: CFD; Ventilação cruzada; Ventilação natural;

Acknowledgments

I would like to thank my home institution coordinator, Professor Guilherme Carrilho da Graça, who gave me the opportunity to study abroad. I would not have had the privilege to work with a great team of professionals in Computational Fluid Dynamics, headed by Professor Bert Blocken, in the Eindhoven University of Technology (TU/e) if it had not been for him.

I would like to express my deepest appreciation to the Building Physics and Services (BPS) department for receiving and helping me during my stay in Eindhoven. I express my genuine gratitude to Professor Bert Blocken for receiving me in his research group and guiding me throughout this thesis. I also want to show my gratefulness to Twan van Hooff and Katarina Kosutova for their availability, for all the sapient advices and critics received along the concretization process.

I would like to thank Pedro who helped during the realization of this work and shared the whole Eindhoven experience with me. I also would like to thank my friends and colleagues that were part of this journey.

At last I want to thank my family for all the support and motivation during my stay in Eindhoven and my girlfriend, Sara, for all the patience, advices and encouragement.

Contents

List of figures

List of tables

1. Introduction

Since the mid-1970s, due to the energy crisis, international communities have made large promises to reduce the use of energy for heating and cooling in buildings. According to the Buildings Performance Institute Europe (BPIE 2011), buildings in Europe represent 40% of total energy consumption and are responsible for 36% of greenhouse gas emissions (GGE). An example of these efforts is the European Commission's target to reduce the GGE by 20% compared to the 1990 levels, achieve 20% of renewable energy sources in the total energy production and level up the energy efficiency by 20%, all three by 2020 (BPIE 2011). To accomplish these targets, buildings have to improve their environmental performance exploiting renewable sources, emphasizing the use of passive and active solar energy solutions, day lighting and natural cooling (Balaras et al. 2007).

Since people spend more than 90% of their time in an indoor environment (a dwelling, a workplace, a transport vehicle) (Awbi 2003), it is also important to ensure that the occupants have the proper indoor condition (e.g. thermal comfort, air quality, etc.) besides the energy problem. Over the last decades, indoor environments have changed due to the increase of energy-saving measures: the thermal comfort has increased due to better insulation and better air-conditioning or heating systems. However, as a consequence, in air-conditioned buildings, a deterioration of the indoor air quality has been registered (Robertson et al. 1985). An example is the appearance of the term "sick building syndrome" (SBS) that has appeared during this energy-saving era (Awbi 2003). The SBS is basically a complaint about the indoor air quality and can be expressed by the sensations of stuffy, stale and unacceptable indoor air, irritation of mucous membranes, headache and/or lethargy. These problems have been associated with poor plant maintenance, high concentrations of internally generated pollutants and low outdoor air supply rates (Awbi 2003).

Therefore new buildings are evolving to accommodate three interrelated requirements (Karava 2008):

- Promote sustainable development through the use of environmentally friendly materials and utilization of renewable energy sources.
- Minimize energy cost for processes such as heating, cooling, ventilating and electrical lighting.
- Enhance indoor environmental quality and comfort which will increase productivity.

Hence, one of the key elements in building performance is the ventilation because it can influence the air quality, the thermal comfort and the energy consumption.

Ventilation can be done by three different methods: mechanical (which consumes energy), natural (which uses wind-induced pressure differences, thermally-induced pressure differences or both) and hybrid ventilation (a combination of mechanical and natural ventilation). Natural ventilation due to its capacity to influence the three requirements stated by Karava (2008) was the one

assessed throughout this thesis. Cross-ventilation in particular was studied in this report (different openings in different façades of the building).

To understand the effects of ventilation inside a building, different methods can be used. One of these methods is numerical simulation using Computational Fluid Dynamics (CFD). However, the accurate modeling of cross-ventilation flows in large openings using CFD software is still a topic of concern. There are difficulties in modeling the interaction at the openings of an enclosure; between the outdoor wind flow around the building and the indoor airflow inside the building (Ramponi & Blocken 2012a). CFD simulations are also very sensitive to the different input parameters that have to be set by the user.

The aim of the present research is to better understand how cross-ventilation is affected by changing the length of the building, the number of partitions and the position of the partition opening for a generic building configuration. This results in the following research question:

How do different building geometries affect cross-ventilation?

The following sub-questions should be answered:

- What is the mean age of air and the CO_2 concentration in different cross-ventilated building geometries?
- What is the air exchange efficiency in different cross-ventilated building geometries?
- What are the limits for cross-ventilation regarding building dimensions for different building geometries?
- How is the flow field affected by the presence of a partition wall in different building geometries?

To answer these questions this thesis was divided in three different sections: the literature study, the validation study and the simulation of different geometries. Firstly different types of ventilation, the methods to evaluate the ventilation performance and the principles of computational fluid dynamics are explained (chapter 2,3), followed by an overview of the previous studies (chapter 4). The second part is the validation study (chapter 5), where a standard building configuration with two opposite openings is simulated and compared with the experimental results by Karava (2008) and Karava et al. (2011). These results are the basis of the numerical simulations. A sensitivity analysis is also performed in this section. In the third part (chapter 6), different building configurations are simulated and the ventilation performance of the building is assessed by different methods (velocity vector fields, volume flow rate, mean age of air, CO_2 concentration, air exchange efficiency and air exchange rate). The conclusions and recommendations for future work are presented in the final chapter of the master thesis (chapter 7).

2. Ventilation

The terms of air-conditioning and ventilation are often used as if they are synonymous. However they have different meanings. Air-conditioning means the heating, cooling and control of moisture in buildings, involving the calculation of the heating and cooling load besides the design of the control systems, ductwork and plant components. On the other hand, ventilation is the provision and distribution of outside air into a building or a room. The purpose of ventilation is to provide acceptable thermal and air quality conditions in the space that is being ventilated, by the correct removing/diluting of the concentration of pollutants generated inside the building. Therefore, ventilation is necessary for both air-conditioned and non-air-conditioned buildings. For the correct operation of a ventilation system it is necessary to ensure that the correct quantity and quality of the outside air is entering the building and the air is being correctly distributed inside the building (air-conditioned system can have an important role at this level). Ventilation can be done by three different methods: natural, mechanical and hybrid (a combination of both) ventilation.

2.1. Mechanical ventilation

Mechanical ventilation refers to providing outside air into a building or room by mechanical fans or blowers (consuming energy). These can be installed directly on windows, walls or doors, or installed in air ducts for supplying/exhausting air into/from a room. Mechanical ventilation is considered to be reliable in delivering the design flow rate, regardless of the impact of the outside environment (temperature, wind) and the airflow path can be controlled. Filtration systems can be coupled to mechanical ventilation, to prevent harmful organisms, particulates, gases, odors and vapors to enter the interior space. On the other hand, the installation, operation and maintenance can have a high cost. Besides, the electrical system risks failure or unexpected working conditions which can lead to the spread of infectious diseases, for example.

2.2. Natural ventilation

Natural ventilation is an important factor to obtain an energy-efficient built environment (Ramponi & Blocken 2012a) and in the development of sustainable healthy indoor environments. Natural ventilation is the air exchange between the outdoor environment and an enclosed or semi-enclosed indoor environment. It can be driven by wind-induced pressure differences, by thermally-induced pressure differences (buoyancy) or by a combination of both. According to Alexander et al. (1997), the natural ventilation systems are usually designed to use the buoyancy force alone because of its straightforward design. However, the wind forces cannot always be neglected because they can have an important impact on the ventilation system. As a consequence, the performance of the system can be affected (Alexander et al. 1997).

Natural ventilation can be used to draw cold outside air into the building to provide free cooling, reducing the cooling energy consumption (i.e. ventilative cooling) (Tzempelikos et al. 2007). Natural ventilation can be used in a hybrid ventilation system (uses passive and active features).

This kind of system uses natural ventilation, for example, in night cooling or pre-cooling of a building which is used to reduce the indoor air temperature and the temperature of the building mass. This will then reduce the cooling load during the day (Spindler & Norford 2009). To maximize the efficiency of the cooling process, the correct understanding of airflows in a room is required. The natural ventilation system should be designed together with the components with exposed thermal mass (floor or ceiling concrete slabs), to place them near the main jet region to increase the heat transfer (Karava et al. 2011).

In natural ventilation systems there are two different design types: single-sided ventilation and cross-ventilation. In single-sided ventilation the wind-driven ventilation flow is dominated by convection and turbulence of the wind. It is caused by the temporal changes in wind speed and direction, and by the building itself and its neighbours. According to Awbi (2003), the maximum distance from the opening(s) in which single-sided ventilation is effective is 2.5 times the ceiling height. Figure 1 shows examples of single sided ventilation.

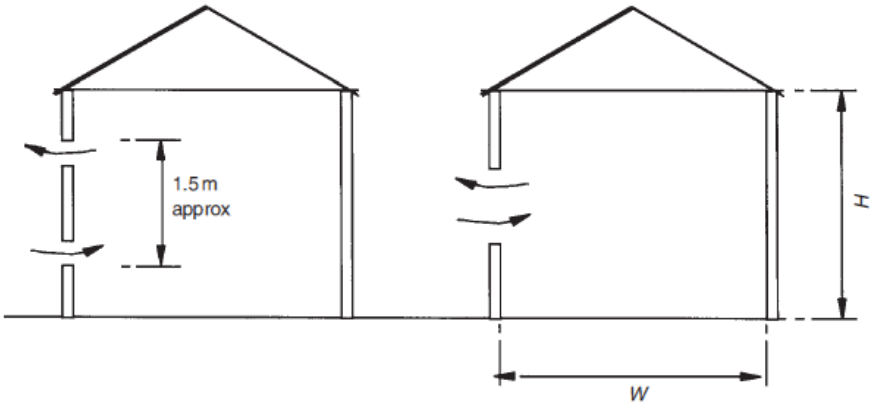

Figure 1 Single-sided ventilation (Awbi 2003).

In cross-ventilation, different openings exist in different façades of the building. The action of wind will generate pressure differences between the various openings and create airflow through an internal space (Jiang et al. 2003). In cross-ventilation, generally a significant conservation of inflow momentum exists with the inlet airflow traveling freely across the room (Carrilho da Graça & Linden 2003). According to Awbi (2003), cross-ventilation should be used with a building depth (distance between the wall with the opening and its opposite wall) superior to 2.5 times the ceiling height, and it is effective till 5 times the ceiling height. Figure 2 shows an example of cross-ventilation. This design is the most efficient but not always applicable. That can occur due to the existence of only one external façade such as in a large office building. Single-sided ventilation is then used instead. Though, this option has a lower airflow rate, so the size and the placement of the opening has to be carefully planned (Jiang et al. 2003).

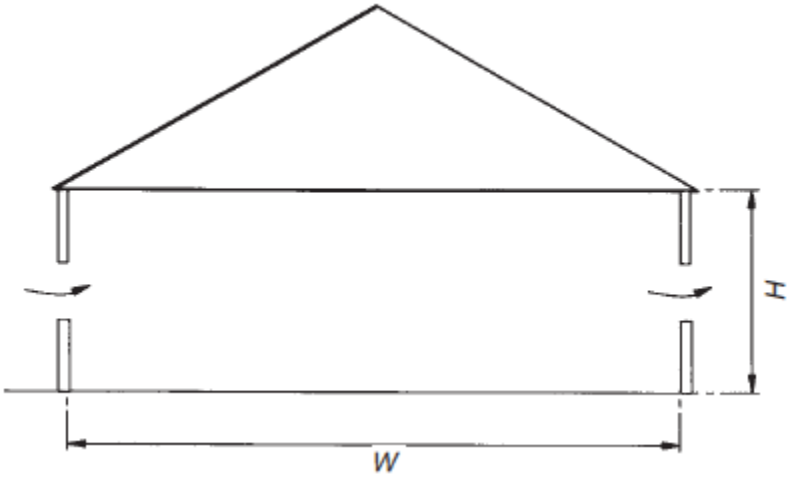

Figure 2 Cross-ventilation (Awbi 2003).

According to Karava et al. (2011), in cross-ventilation higher airflow rates are found in configurations with:

(i) Symmetric openings.
(ii) Inlets located at the mid-height of the building or above.
(iii) Inlet-to-outlet area ratio lower than one (inlet opening smaller than the outlet opening).

These configurations can be used for space or building fabric cooling. However, if natural ventilation is used for thermal comfort, these configurations should be avoided because it may lead to high indoor air velocities. According to the ANSI/ASHRAE (2007) thermal comfort standard, air velocities should be lower than about 0.5 m s^{-1} in the occupied zone. For this reason, when thermal comfort is to be achieved, configurations with the inlet opening larger than the outlet opening should be used (Karava et al. 2011).

2.3. Hybrid ventilation

Hybrid ventilation is a combination between the natural and mechanical ventilation. It uses natural ventilation to provide the desired flow rate. When it is impossible, it relies on the mechanical ventilation to achieve the desired flow. The hybrid ventilation can be a valuable solution in cases when the natural ventilation has problems of lack of air flow control or when there is no temperature control, as it in the case of extreme weather. These systems should be designed to maximize the use of natural conditions and to incorporate the mechanical systems efficiently. Consequently the energy consumption can be minimized and the air quality and comfort could be maximized. There are several methods to apply hybrid ventilation such as the

mechanical air extraction with natural supply inlets, the mechanical air inlet with natural extraction, or mechanical cooling or heating combined with natural ventilation (Awbi 2003).

2.4. Ventilation requirements

An efficient distribution of the fresh air is of major importance to achieve thermal comfort and a good indoor air quality for the well-being of the inhabitants, (Gan 2000). Establishing the correct ventilation airflow is essential to avoid certain illness related to indoor environments such as human transmitted diseases, hypersensitivity reactions to bacteria and fungus, exposure to contaminants and toxic products. Building ventilation implies the management of the incoming fresh air by distributing and circulating it and extracting the air through the envelope, preventing the contamination of the indoor environment (Meiss et al. 2013). The ventilation is less controllable in naturally ventilated buildings when compared to the mechanically ventilated ones. Hence, it is necessary to make a correct design of the natural ventilation system to keep a good air quality inside the building. To ensure this, some parameters can be calculated:

i. The age of air;
ii. The air exchange efficiency or;
iii. The CO_2 concentration

As an example, special attention should be given to the maximum room depth over which fresh air distribution is effective during the design phase (Gan 2000).

During the last 160 years, in the USA, there has been a constant review of the recommended ventilation flow rates for an occupied building. Figure 3 shows these reviews which reflect the lack of knowledge of the optimum flow rates necessary to keep a building with good health and comfort criteria. The constant adjustment of policies can also have origin in constant changes in the building design, lifestyle, technological development or due to the change in the relative cost of energy (Awbi 2003).

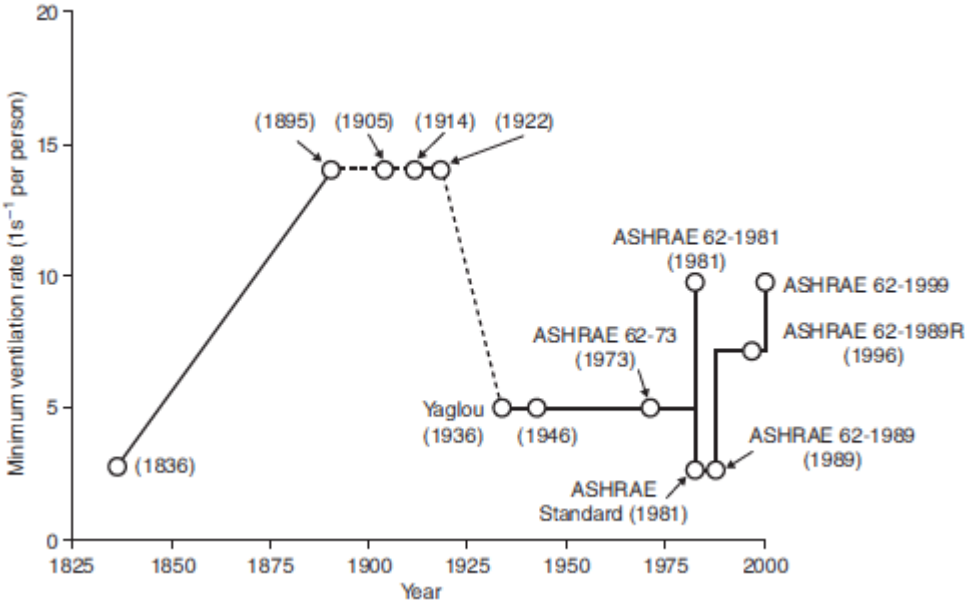

Figure 3 Changes in the minimum ventilation rates in the USA (Awbi 2003).

Nowadays there are recommendations and standards that should be followed during the design of ventilation systems. ASHRAE Standard 62-1999 (1999) gives air flow rate as function of the number of occupants for different type of building uses (Table 1). For different building uses, different occupation criterion exists in the regulations. As example, in The Netherlands the minimum area per person for an office building is 7 m^2 (NEN 1824:2010 2010).

Table 1 Outdoor air supply rates recommended by ASHRAE Standard 62-1999 (1999).

Application	*Estimated maximum occupancy* (*persons per* 100 m^2)	*Required air flow rate* ($l\,s^{-1}$ *per person*)
Office spaces	7	10
Office conference rooms	70	10
Auditoria	150	8
Classrooms	50	8
Dining rooms	70	10
Bars and cocktail lounges	100	15
Ballrooms and discos	100	13
Smoking lounges	70	30*
Hospital patient rooms	10	13
Malls and arcades	20	1
Retail stores	5~30	0.5~1.5+
Swimming pools (pool and deck area)	—	2.5+
Residences (living areas)	—	0.35§

Notes
* Local exhaust recommended.
+ These values are given in $l\,s^{-1}$ per m^2 floor area.
§ This value is given as air change per hour (but not less than 7.5 $l\,s^{-1}$ per person).

2.5. Age of air and air exchange efficiency

To characterize the ventilation effectiveness of fresh air distribution, the local mean age of air (τ) can be used. This is a statistical measure of the time it takes for a parcel of air to reach an arbitrary point after it has entered an enclosure (Sandberg 1981).

Another air quality indicator used in this field is the air exchange efficiency which is defined as the efficiency of airflow flushing a volume with external air (Hang et al. 2009). It represents the ratio between the minimum time for replacing the air in the room (τ_n) and the average time for air exchange (τ_{exe}). The minimum time for replacing the air in the room is the time needed to replace the whole volume using a certain ventilation flow rate and the average time for air exchange is the actual time the air is in the enclosed space. It is known that τ_{exe} is twice the local mean age of air (τ) (Etheridge & Sandberg 1996). It can be represented by Equation (1):

$$\varepsilon_a = \frac{\tau_n}{\tau_{exe}} = \frac{\tau_n}{2\tau} \quad (1)$$

The air exchange efficiency is related to the flow type as Table 2 shows. In an ideal piston flow, the air enters a space at one end, moves through it with the same velocity on parallel paths and the air exchange efficiency is 100%. In a perfect mixed system, where the conditions are uniform throughout the enclosure at a given moment, the air exchange efficiency is 50%. In a short-circuiting situation, where the major part of the flow flushes quickly through a small portion of the volume and only a small part flushes through the entire enclosure, the air exchange efficiency is less than 50% (Hang et al. 2009; Hang and Li 2011).

Table 2 Air exchange efficiency for characteristic room ventilation flow types (Novoselac & Srebric 2003).

Flow pattern	Air exchange efficiency	Comparison with the average time of exchange
Unidirectional flow	0.5 - 1.0	$\tau_n < \tau_{exc} < 2\tau_n$
Perfect mixing	0.5	$\tau_{exc} = 2\tau_n$
Short Circuiting	0 - 0.5	$\tau_{exc} > 2\tau_n$

2.6. Carbon dioxide (CO_2) concentration

There are many types of contaminants and for each one, there exists a different exposure limit depending on the duration a person is exposed to the pollutant (Awbi 2003). When designing a ventilation system, it is necessary to identify the contaminants, the sources and the acceptable concentrations in indoor air, so the proper flow rate can be specified to dilute or extract these contaminants.

One of these contaminants is carbon dioxide (CO_2) and in a building it is mainly produced by human respiration. CO_2 is a way to measure the staleness of indoor air due to the fact that it

cannot be filtered, adsorbed or absorbed, contrasting with other contaminants. According to Fanger et al. (1988), CO_2 is not a good predictor of air quality perceived by people entering a space, and for this reason special attention should be given to the proper design of the ventilation systems.

CO_2 is present in the outdoor air in a volume average of 0.04% and the expired air contains 4.4% by volume of CO_2. According to Awbi (2003), the rate of production of CO_2 by respiration is related to the metabolic rate of a person (Equation (2)), where G is the CO_2 production in l h^{-1}, M the metabolic rate (W m^{-2}) and A is the body surface area (m^2). As an example, an average sedentary adult (M = 70 W m^{-2} and A = 1.8 m^2) produces 18 l h^{-1} of CO_2.

$$G = \frac{4 \times 10^{-5} MA}{3600} \tag{2}$$

The maximum recommended concentration of CO_2, for 8h occupation is 0.5%. Although it is known that concentrations over 0.1% can cause discomfort and headache (Sundell 1982).

After analysing these numbers it is possible to understand that the CO_2 concentration has an impact in the air quality of a room. For this reason it is important to take into account the population density, the outdoor flow rate and the efficiency of the ventilation system during the design phase. In Table 3, it is possible to observe the outdoor flow rates necessary to maintain 0.5% and 0.25% CO_2 concentration for different metabolic rates, assuming a perfect mixing of the CO_2 with the room air. When this perfect mixing does not occur, higher values of ventilation rate should be used.

Table 3 Outdoor air requirements for respiration (BS 5925 1991).

Activity (adult male)	*Metabolic rate, M* (W)	*Flow rate to maintain room CO_2 concentration at a given value assuming 0.04% CO_2 in fresh air* ($l\,s^{-1}$)	
		0.5% CO_2	0.25% CO_2
Seated quietly	100	0.8	1.8
Lightwork	160–320	1.3–2.6	2.8–5.6
Moderate work	320–480	2.6–3.9	5.6–8.4
Heavy work	480–650	3.9–5.3	8.4–11.4
Very heavy work	650–800	5.3–6.4	11.4–14.0

Note
These values are based on CO_2 production rate of 7.2×10^{-5} M ($l\,s^{-1}$).

3. Methods for predicting ventilation performance for buildings

The ventilation performance usually can be predicted or evaluated by analytical and empirical solutions, experimental measurements (small and full scale) and computer simulations (multizone models, zonal models and computational fluid dynamics).

Analytical models are the oldest method to predict ventilation performance. In the present days, the contributions for research literature are minimal due to the fact that it has been developed for decades. Although, it is still very useful nowadays due to its simplicity, rich in physical meaning and little computer requirements. Analytical models are derived from fundamental equations of fluid dynamics, heat transfer and chemical-species conservation equations, and use simplifications in the geometry and thermo-fluid boundary conditions to calculate the solutions. Empirical models, as the analytical models, are derived from conservation equations. Often, these models were developed using data from experimental measurements or advanced computer simulations to obtain coefficients that make empirical models successfully work. Empirical models are effective, cost-cutting tools to predict ventilation performance. As the analytical models, empirical models are very case dependent and their contribution to the research literature in the last few years has been scarce after a few decades of development. However, these methods are less suitable for practical applications in specific environments (van Hooff et al. 2011) and its capabilities to determine the room airflow in different types of openings, in complex geometries or with different heat sources are doubtful (van Hooff 2012).

Small-scale experimental models use measuring techniques to predict or evaluate ventilation performance of a reduced-scale building or room. These models are effective and economical to use when comparing to the full-scale experimental models. Nevertheless, attention has to be given to guarantee that important dimensionless flow parameters are equal to the ones existing in the real buildings or rooms. It can also be challenging to scale down complex flow geometry. According to Chen (2009), these models were mainly used to validate analytical, empirical or numerical models, which were then scaled up to real buildings to study the ventilation performance. The full-scale experimental models, as the small-scale ones, are usually used to validate numerical models (mainly CFD models) and then to predict ventilation performance or design ventilation systems. The full-scale experimental models can be divided in laboratory experiment or *in-situ* measurements. These models give the most realistic prediction of ventilation performance for buildings (Chen 2009). On the other hand, these experiments are very expensive, time consuming and are not free from errors.

The multizone network models are mostly used to predict air exchange rates and airflow distributions between zones of a building and between the building and the outdoors, with or without mechanical ventilation systems. These models assume that the momentum effect can be neglected. Uniform air temperature and uniform chemical-species concentration in a zone are also assumed. The multizone models seem to be the only tool to obtain meaningful results for predicting ventilation performance in an entire building (Chen 2009). Zonal models divide a room into a limited number of cells to calculate the temperature in each cell, in opposite to the well-mixing assumption of the multizone network models. Also, these models predict temperatures in

large indoor spaces or in rooms with stratified ventilation system. These models do not solve the momentum equation therefore they are mainly used for flows with weak momentum forces in the room air.

3.1. Computational Fluid Dynamics (CFD)

Computational Fluid Dynamics (CFD) refers to solving and analyzing fluid flow problems numerically. CFD solves a set of partial differential equations for the conservation of mass (continuity equation), momentum (Navier-Stokes equations), energy, chemical-species concentrations and turbulence quantities. CFD models have become increasingly used in predicting ventilation performance despite of still having some uncertainties in the models. It requires appropriate knowledge on fluid mechanics and demands high computer resources because of i) the awareness of the power of these models is increasing; ii) the increase in the computational resources and; iii) the increasing availability of user-friendly software interfaces. The importance of CFD in all domains of engineering has been increasing and its use for studying the indoor air quality or thermal comfort are examples of its significance. The study of indoor air quality with CFD models is generally divided in three categories (Chen 2009):

- indoor air quality studies in spaces with non-uniform distributions of contaminant concentrations;
- natural ventilation designs;
- investigations on stratified indoor environments.

The use of CFD models in ventilation performance of indoor environments have been largely studied due to difficulty in predicting it with other models (Chen 2009). Example of this is the design of natural ventilation which is very challenging because of the constant change of wind speed and direction resulting from the impact of adjacent buildings (Chen 2009). Additionally there are difficulties in modeling the interaction at the openings of an enclosure; between the outdoor wind flow around the building and the indoor airflow inside the building (Ramponi & Blocken 2012b).

As stated before, CFD is a powerful tool but only if used correctly. Otherwise it can be a dangerous tool giving incorrect results and for this reason many professionals mistrust CFD results. It is necessary to always question the accuracy and reliability of the CFD results because CFD results are wrong until proven otherwise (Blocken 2014).

3.1.1. Fundamental equations

There is a set of fundamental equations that are the basis of CFD: the continuity equation (Equation (3)) and the momentum equations known as the Navier-Stokes equations (in modern CFD literature, the Navier-Stokes equations may refer to the entire system of equations for the solution of the viscous flow: continuity, momentum and energy). The Navier-Stokes equations are three coupled, non-linear second order partial differential equations describing the fluid flow. For

an incompressible, viscous, isothermal flow of a Newtonian fluid, the equations are given by Equation (4)-(6).

$$\frac{\partial \rho}{\partial t} + \frac{\partial}{\partial x}(\rho u) + \frac{\partial}{\partial y}(\rho v) + \frac{\partial}{\partial z}(\rho w) = 0 \quad (3)$$

x: $$\frac{\partial u}{\partial t} + \left\{u\frac{\partial u}{\partial x} + v\frac{\partial u}{\partial y} + w\frac{\partial u}{\partial z}\right\} = -\frac{1}{\rho}\frac{\partial p}{\partial x} + \nu\left\{\frac{\partial^2 u}{\partial x^2} + \frac{\partial^2 u}{\partial y^2} + \frac{\partial^2 u}{\partial z^2}\right\} \quad (4)$$

y: $$\frac{\partial v}{\partial t} + \left\{u\frac{\partial v}{\partial x} + v\frac{\partial v}{\partial y} + w\frac{\partial v}{\partial z}\right\} = -\frac{1}{\rho}\frac{\partial p}{\partial x} + \nu\left\{\frac{\partial^2 v}{\partial x^2} + \frac{\partial^2 v}{\partial y^2} + \frac{\partial^2 v}{\partial z^2}\right\} \quad (5)$$

z: $$\frac{\partial w}{\partial t} + \left\{u\frac{\partial w}{\partial x} + v\frac{\partial w}{\partial y} + w\frac{\partial w}{\partial z}\right\} = -\frac{1}{\rho}\frac{\partial p}{\partial x} + \nu\left\{\frac{\partial^2 w}{\partial x^2} + \frac{\partial^2 w}{\partial y^2} + \frac{\partial^2 w}{\partial z^2}\right\} + g \quad (6)$$

x, *y*, *z*: Cartesian co-ordinates

u, *v*, *w*: velocities along the Cartesian axes x, y, z [m s^{-1}]

p: pressure [Pa]

v: kinematic molecular viscosity [m^2 s^{-1}]

ρ: density [kg m^{-3}]

g: gravitational acceleration [m s^{-2}]

There are three main methods to predict the turbulent flow: Direct Numerical Simulation (DNS), Large Eddy Simulation (LES) and Reynolds-Averaged Navier-Stokes equations (RANS). In the first method - DNS - the Navier-Stokes equations are solved for all the motions in the turbulent flow. This method is only used with low Reynolds numbers and simple geometries, due to its high demand of computer resources. In LES, the Navier-Stokes equations are filtered, separating the large-eddies from the small turbulent eddies, removing these ones. The largest scale motions of the flow are solved and the small-scale motions are modeled by a subgrid-scale model. This method is less accurate than DNS but more accurate than the RANS. In RANS method, the equations are derived by averaging the Navier-Stokes equations. In this method, only the mean flow is solved while all scales of turbulence have to be modeled using the so-called turbulence models. The RANS method has been the most widely used in the field of numerical computation of air flow inside buildings.

3.1.2. Reynolds-Averaged Navier-Stokes equations – turbulence models

As aforementioned, the RANS methods require the modeling of all scales of turbulence. As a consequence of the averaging process, Reynolds stresses are created and the RANS equations do

not form a closet set. Hence, approximations have to be made using turbulence models. A given turbulence model is unable to fully represent all turbulent flows therefore different turbulent models have been developed and they should be carefully chosen for each different case. There are two main eddy-viscosity turbulence models: the *k-ε* model and the *k-ω* model and each one has different revised versions (i.e. RNG *k-ε* or SST *k-ω*).

In the k-ε models (in the standard and in the revised ones) there are two transport equations to represent the turbulent properties of the flow. In these equations there are two transported variables: the turbulent kinetic energy, *k*, and the turbulent dissipation rate, *ε*. In general, the revised models of the standard *k-ε* model are more reliable and accurate for a wider range of flows than the standard *k-ε* model. For example, the renormalization group (RNG) *k-ε* model includes additional terms and functions in the transport equations of *k* and *ε*, and it was developed to account for the effect of smaller scales of motion. This model has a good performance in indoor air simulations (Ramponi & Blocken 2012b).

In the *k-ω* models (standard and in the revised ones) there are two transport equations to represent the turbulent properties of the flow. In these equations there are two transported variables: the turbulent kinetic energy, *k*, and the specific dissipation rate, *ω*. The *k-ω* model is well suited for simulating flow in the viscous sub-layer. The shear stress transport (SST) *k-ω* model is an example of a revised version of the standard *k-ω* model. The SST *k-ω* model is a combination of the *k-ω* and the *k-ε* model, with the first one modeling flows near the walls and the second one in the free steam.

In indoor air flow modeling, the RNG *k-ε* model has a better performance than the standard *k-ε* model (Ramponi & Blocken 2012b; Evola & Popov 2006; Mistriotis et al. 1997; Bartzanas et al. 2007; Kobayashi, T. et al. 2009) and the SST *k-ω* model has been found to perform even better than the RNG *k-ε* (Ramponi & Blocken 2012b).

3.1.3. Computational domain and grid

In the preprocessing of a CFD study a geometrical model of the building is made and it is placed in a computational domain, which is then meshed and on which boundary conditions are applied. The computational domain in the CFD simulation for building engineering represents the built area that is investigated. Meshing the computational domain consists on the division of the domain in a large number of control volumes or cells. There are two main types of mesh structures: structured meshes and unstructured meshes (Figure 4). The first ones are quadrilateral cells in 2D and hexahedral cells in 3D (the domain is divided in rectangular areas) and are usually used for simple geometries. The unstructured meshes are composed by triangular and/or hexahedral cells in 2D and tetrahedral, prism, pyramid and/or hexahedral cells in 3D and, in general are used in complex geometries. They can be automatically generated with grid generation software but this often provides poor grid quality. When meshing a domain it is recommended that a maximum expansion rate of 1.2-1.3 is used between cells.

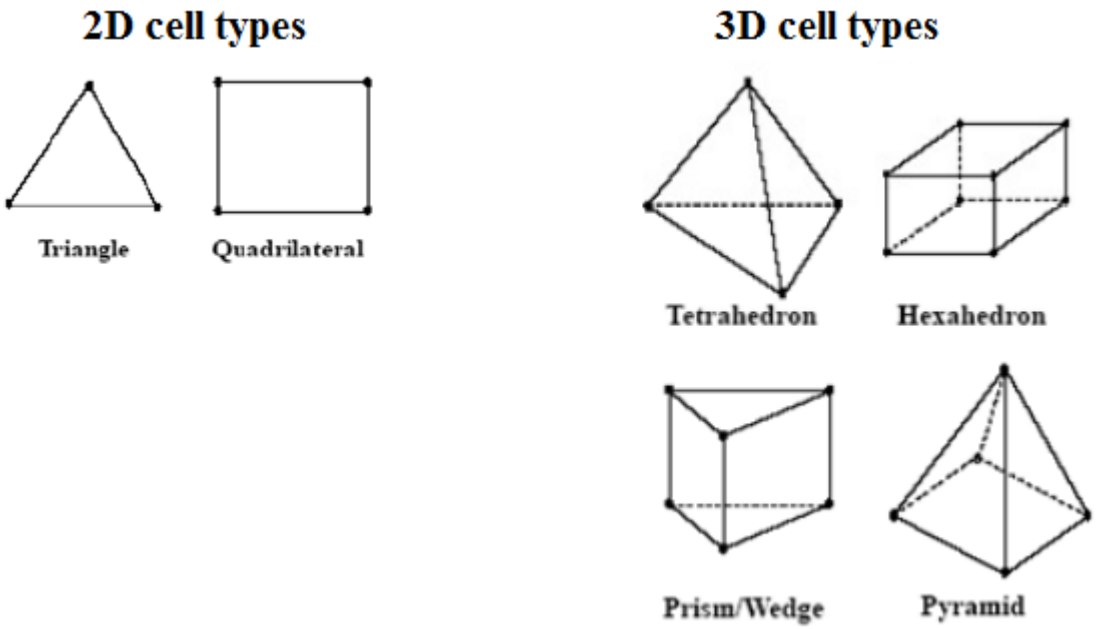

Figure 4 Different types of control volumes or cells (Ansys 2009).

The computational domain in the CFD simulation for building engineering represents the built area under investigation. The most used discretization technique, due to its versatility, is the control volume method. In this method, each cell of the computational domain is a finite volume, and in its centers the governing equations and the equations of the turbulence model are solved. It is necessary to accurately model the areas where the flow has a bigger impact and in the areas of interest, on which the higher level of detail (higher number of cells) should be present. In buildings, where the areas of interest are usually situated, at least 10 cells should be used per building side, as a starting grid resolution (Franke et al. 2007). Therefore, it is important to perform a grid-sensitivity analysis to understand the impact of the mesh resolution on the results (Franke et al. 2007).

It is necessary to guarantee that the computational domain is large enough to avoid the influence of the boundaries (inlet, outlet, bottom, top and sides of the domain) on the flow around the buildings. According to the best practice guidelines (Franke et al. 2007; Tominaga et al. 2008), the size of the computational domain should be 5 times the building height (*5H*) or more away from the building to the sides and to the top of the building. The outflow boundary condition should be set at least *15H* behind the building to allow the flow re-development. The distance between the inlet boundary and the building should be *5H* (Franke et al. 2007; Tominaga et al. 2008). Blocken et al. (2007a,b) recommended a reduction of this inlet distance from *5H* to *3H* of the building height to limit the development of unintended streamwise gradients.

3.1.4. Boundary conditions

In simulating of the lower parts of the atmospheric boundary layer (ABL) (0-200m) an accurate description of the flow near the ground surface is required. To describe this flow it is required to have the inlet profiles of the mean wind velocity, turbulent kinetic energy, turbulence dissipation rate (k-ε models) and specific dissipation rate (k-ω models), which are generally fully developed, neutrally stratified and should represent the roughness characteristics of the terrain upstream of the inlet plane. To define these profiles it is necessary to have the vertical profiles of mean wind speed (U) and streamwise turbulence intensity (I_u), which can be obtained from the measured data when available.

The inlet profile of the mean wind velocity (U) is described by the logarithmic law (Equation (7)), where u^* is the friction velocity (represents the magnitude of de fluctuations in the velocity, in the turbulent boundary layer), k is the von Karman constant (0.42), z the height coordinate and z_0 is the aerodynamic roughness length.

$$U(z) = \frac{u^*}{k} \ln\left(\frac{z + z_0}{z}\right) \tag{7}$$

The vertical distribution of the turbulent kinetic energy (k), measure of the energy associated with the turbulent fluctuations in the flow, can be calculated using Equation (8), where the standard deviations of the turbulent fluctuations (σ) in the three directions are needed (u, v, w).

$$k(z) = \frac{1}{2}(\sigma_u^2(z) + \sigma_v^2(z) + \sigma_w^2(z)) \tag{8}$$

The standard deviations of the turbulent fluctuations are related to the turbulence intensity: $I = \frac{\sigma}{U}$. However, only the streamwise turbulence intensity component (I_u) is usually measured and assumptions for the other two components have to be made:

- **Assumption 1.** $\sigma_u^2 \gg \sigma_v^2 \approx \sigma_w^2$, which results in:

$$k(z) = \frac{1}{2}(I_u(z)\, U(z))^2 \tag{9}$$

- **Assumption 2.** $\sigma_u^2 \approx \sigma_v^2 + \sigma_w^2$, which results in:

$$k(z) = (I_u(z)\, U(z))^2 \tag{10}$$

- **Assumption 3.** $\sigma_u^2 \approx \sigma_v^2 \approx \sigma_w^2$, which results in:

$$k(z) = \frac{3}{2}(I_u(z)\, U(z))^2 \tag{11}$$

In conclusion, the relationship between the turbulent kinetic energy (k), the streamwise intensity component (I_u) and the wind speed (U) is given by Equation (12), where a is equal to 0.5, 1 or 1.5. The best practice guidelines by Tominaga et al. (2008) recommend the use of a = 1.

$$k(z) = a\,(I_u(z)\, U(z))^2 \tag{12}$$

The vertical profile of the turbulence dissipation rate (ε) is defined by Equation (13), where z_0 is the aerodynamic roughness length. The specific dissipation rate (ω), which is derived from the turbulence dissipation rate (ε) and from the turbulent kinetic energy (k), is given by Equation (14), where C_μ is an empirical constant considered equal to 0.09.

$$\varepsilon(z) = \frac{(u^*)^3}{k(z + z_0)} \tag{13}$$

$$\omega(z) = \frac{\varepsilon(z)}{C_\mu k(z)} \tag{14}$$

It is also necessary to do an accurate description of the flow near the ground surface. Blocken et al. (2007b) described four requirements that should be satisfied, when the wall roughness is expressed by an equivalent sand-grain roughness height (k_s):

1. A high mesh resolution should exist in the vertical direction adjacent to the bottom of the computational domain;
2. The ABL flow should be horizontally homogenous on the upstream and downstream regions of the computational domain;
3. The distance from the bottom of the domain to the centre point of the wall adjacent cell (y_p) should be larger than the roughness height (k_s), $y_p > k_s$;
4. The relationship between the sand-grain roughness height (k_s) and the corresponding aerodynamic roughness length (z_0) should be known.

Blocken et al. (2007b) derived this relation and for Fluent (a commercial CFD software) is expressed by Equation (15), where C_s is the roughness constant.

$$k_s = \frac{9.793\ z_0}{C_s} \tag{15}$$

The selection of the correct k_s and C_s values should be carefully taken into account, because of their importance to reduce unintended streamwise gradients in the flow profiles in the simulation.

4. Overview of previous studies

4.1. Wind tunnel studies

Wind tunnel studies to examine cross-ventilation flow characteristics in a single-zone building were conducted by Karava (2008) and Karava et al. (2011). The wind tunnel experiments were done with a method based on particle image velocimetry (PIV). This method is based on non-intrusive measurements and it allows to obtain whole field functions unlike other wind tunnel techniques which are limited to single-point intrusive measurements (Karava et al. 2011).

Within this study, the wind tunnel experiments were performed in the Boundary Layer Wind Tunnel of the Building Aerodynamics Lab at Concordia University (Stathopoulos 1984), which dimensions are 12 meter long and a cross section of 1.8 x 1.8 m^2. Building models with a scale 1:200 with the dimensions *W x D x H* = 100 x 100 x 80 mm^3 (full scale dimensions of 20 m x 20 m x 16 m) were built with sheets of 2 mm cast transparent polymethylmethacrylate (PMMA). Different configurations were tested, changing the position of the windows (in opposite or adjacent walls and near the bottom, in the middle and near the top of the walls) and different opening areas (wall porosity, $w.p. = A_{opening}/A_{wall}$, between 2.5% and 25%). In all these configurations the window height was fixed (18 mm) changing only the length. The different configurations are shown in Figure 5 and in Table 4.

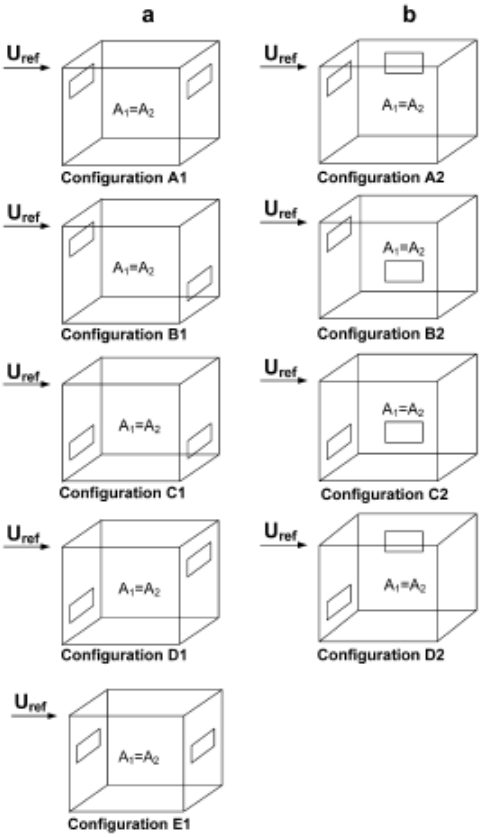

Figure 5 Opening configurations considered for studying the effect of wall porosity and opening location on ventilation flow rate (Karava et al. 2011).

Table 4 Study considerations and range of variables (Karava et al. 2011).

Configuration	Opening location (height above ground)		A_1 (%)	A_2 (%)	A_1/A_2
	Inlet, mm	Outlet, mm			
Leeward outlet					
A1	57	57	5, 10, 20	5, 10, 20	1
B1	57	20	5, 10, 20	5, 10, 20	1
C1	20	20	5, 10, 20	5, 10, 20	1
D1	20	57	5, 10, 20	5, 10, 20	1
A1	57	57	5	20, 10	1/4, 1/2
A1	57	57	10	20, 5	1/2, 2
A1	57	57	20	10, 5, 2.5	2, 4, 8
C1	20	20	5	20, 10	1/4, 1/2
C1	20	20	10	20, 5	1/2, 2
C1	20	20	20	10, 5, 2.5	2, 4, 8
Side-wall outlet					
A2	57	57	2.5, 5, 10, 20	2.5, 5, 10, 20	1
B2	57	20	2.5, 5, 10, 20	2.5, 5, 10, 20	1
C2	20	20	2.5, 5, 10, 20	2.5, 5, 10, 20	1
D2	20	57	2.5, 5, 10, 20	2.5, 5, 10, 20	1

The experiments were performed with a maximum wind-tunnel speed of 8.9 m s^{-1} and an open terrain was simulated with a roughness length (z_0) of 0.005 m. The incident velocity and turbulence intensity were measured with a hot-film probe at the building position and are shown in Figure 6. At the building height (H = 80 mm) a reference mean wind speed and a streamwise turbulence intensity were measured, being U_{ref} = 6.97 m s^{-1} and TI = 10%.

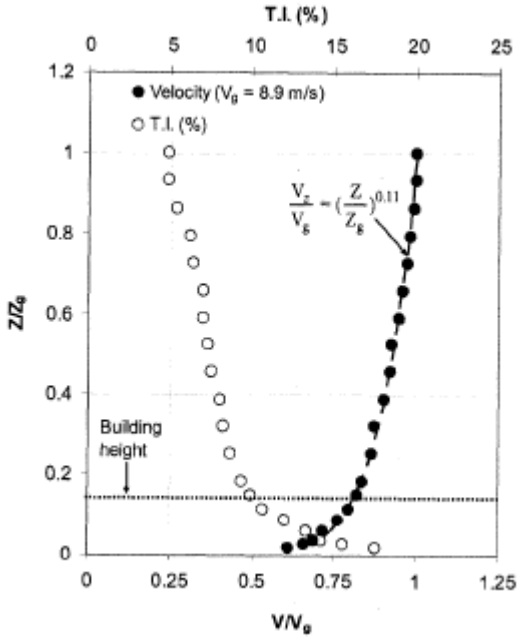

Figure 6 Velocity and Turbulence intensity profiles considered for the PIV measurements (Karava 2008).

In the referred works, basic airflow features were examined in the building space, which can be helpful in the development of models for natural ventilation analysis and design. Figure 7 shows an example, where the x-component of the velocity (normalized by the velocity at the building height) on the center-line directly between the openings. A comparison between the values of PIV data for measurements in the horizontal and vertical plane and single-point hot-film data is shown and it can be noticed that there is a good agreement between both PIV measurements (horizontal and vertical plane). Instead, the hot-film measurements tend to overestimate the velocity near the inlet opening and in the center of the building, which can be justified by high turbulence intensities (hot-film measurements cannot distinguish between the mean velocity and the fluctuating components of the velocity, which exists in highly turbulent flows) in this flow region (over 30%). Figure 8 shows the cross sectional view of the mean velocity vector field on a vertical mid-plane. It can be seen that the main jet passes through the center of the opening, while there are slower moving zones above and below this flow region. After the inlet region, the main jet is accelerated and has a downwards direction caused by the location of the opening (in the mid-height of the building) and by the existence of an upstream recirculating flow (standing vortex) near the ground outside the building model. There is also a recirculation zone below the inlet jet. In the central region the flow decelerates and it accelerates again at the outlet opening. At this opening, the jet is directed upwards, due to the existence of a recirculation flow in the wake region of the building. Although, not all the jet exits the building. Some of the faster moving flow goes up to the ceiling where it travels in the opposite direction of the flow until it reaches the windward façade, being directly downwards.

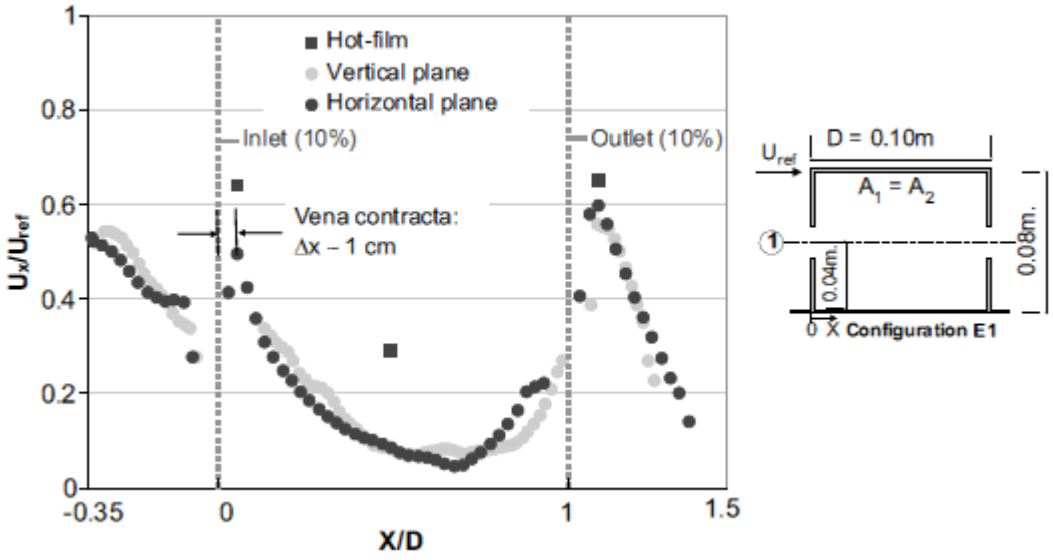

Figure 7 Profile of x velocity component on the center-line directly between the inlet and outlet openings (PIV measurements on a horizontal and vertical plane and single-point hot-film data) (Karava et al. 2011).

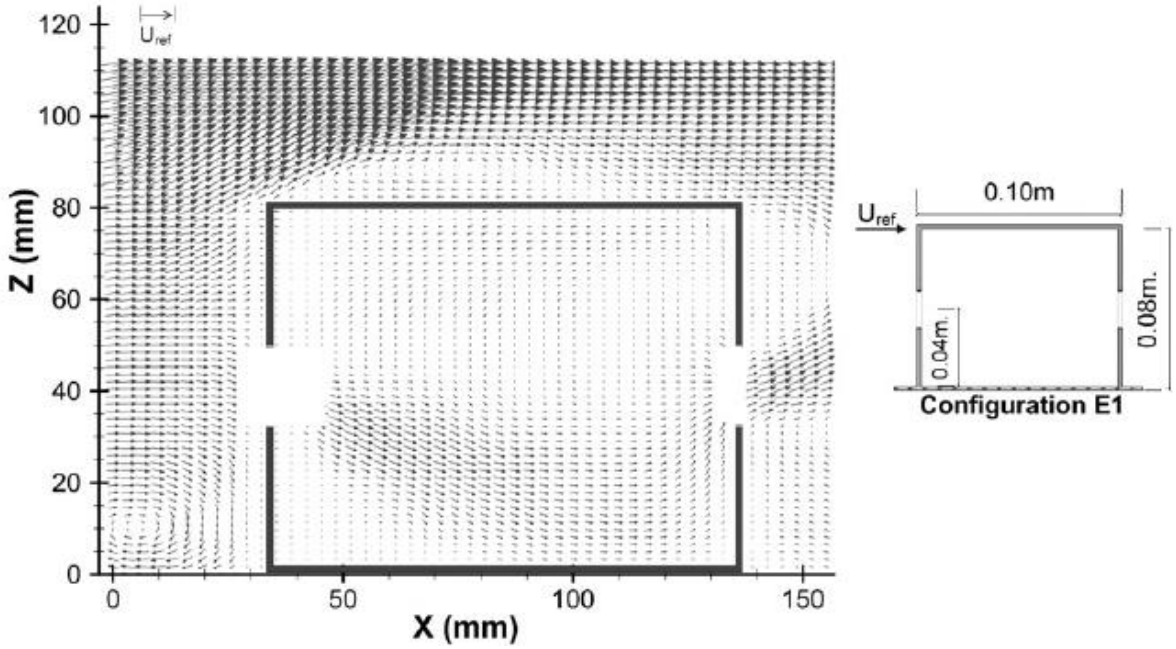

Figure 8 Cross-sectional view of mean velocity vector field on a vertical mid-plane with 10% wall porosity (Karava et al. 2011).

The flow was also studied for the other building configurations. Karava (2008) and Karava et al. (2011), when studying the different building configurations, concluded that configurations with higher airflow rates in cross-ventilation are found in cases of:

(i) Symmetric openings.
(ii) Inlets located at the mid-height of the building or above.
(iii) Inlet-to-outlet area ratio lower than one (inlet opening smaller than the outlet opening).

These configurations can be used for space or building fabric cooling. On the other hand, if thermal comfort is the objective of the cross-ventilation, configurations with the inlet opening larger than the outlet opening should be used (Karava et al. 2011). In all the different configurations, two different zones are found: the main jet and the recirculation zone. These two zones are essential when designing systems which take into account the local heat transfer inside the room.

Chu et al. (2010) made an experimental study of wind-driven cross-ventilation in partitioned buildings. This study was conducted in an open-circuit, blowing wind tunnel. It consisted in testing a cubic shape building with square-shaped openings with different diameters, with a partitioned plate on the middle of the room with different opening positions and diameters (Figure 9). In this study, it was found that the inlet velocity increases as the porosity of the internal wall increases. Although when the internal porosity is over 10% the inlet velocity stabilizes at a constant value of $u_1/U = 0.5$, where u_1 is the average velocity at the inlet opening and U is the external wind velocity.

It was concluded that the maximum ventilation rates were obtained when the inlet and outlet openings had the same size, regardless of the internal partition. It was also concluded that the ventilation rate of the partitioned buildings was always smaller compared to a building without internal partitions, due to the fact that the partitions reduced the pressure difference between the interior and the exterior of the building. This paper concludes, then, that the openings (inlet, outlet and interior) can control the ventilation rate in the building.

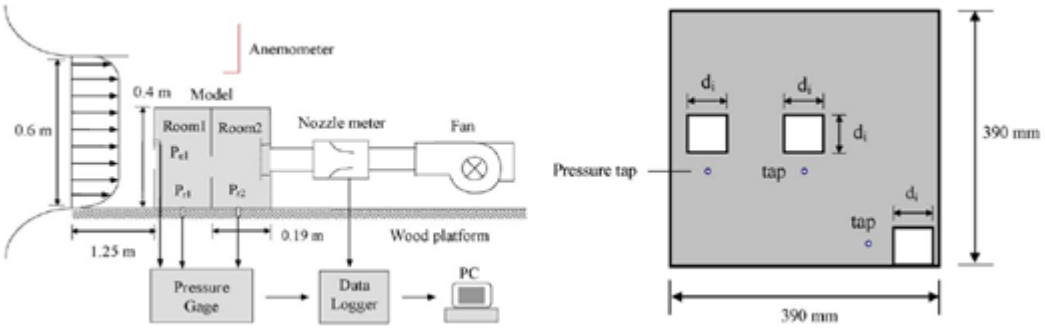

Figure 9 Schematic diagram of experimental setup (left). Geometry of internal partition wall (right).

Bangalee et al. (2013) and Chu and Chiang (2013) performed wind tunnel studies to compare with CFD simulations. The first used flow visualization (to observe the three-dimensional and turbulent flow), PIV measurements (to measure the velocity flow fields, similar to the work of Karava (2008) and Karava et al. (2011)). While the second performed a wind tunnel experiment using the flow condition and building dimensions used by Karava (2008) and Karava et al. (2011). Further information on their works can be found in the next section.

4.2. CFD studies

Based on the work by Karava (2008) and Karava et al. (2011) several CFD studies have been performed. Ramponi and Blocken (2012a), studied the impact of different building opening configurations: two different wall porosity ratios (5% and 10%) and different facing opening positions (in the center and near the ground of the building). The results showed the importance of choosing the appropriate grid resolution and the necessity to use at least second-order accurate discretization schemes to reduce the effect of numerical diffusion. The study concluded the importance of choosing the correct amount of physical diffusion due to its impact on the results.

Ramponi and Blocken (2012b) performed a set of simulations to analyze and evaluate the impact of different computational parameters on coupled CFD simulations of wind-induced cross-ventilation. In this study the openings (both with 10% wall porosity) were situated on the center of the two opposite walls (Figure 10). The dimensions of the computational domain were based on the best practice guidelines by Franke et al. (2007) and Tominaga et al. (2008) apart from the upstream length that was reduced to 3 times the building height to avoid the development of unintended streamwise gradients (Blocken et al. 2007a,b). Thus the width of the computational domain had a cross section defined as $W_D = W + 10H$ and the height defined as $H_D = H + 5H$, where

W is the width of the building and *H* the building height. The computational grid was created based on the surface-grid extrusion technique developed by van Hooff & Blocken (2010), using a maximum stretching ratio of 1.2 controls the cells surrounding the building model. The roughness length was equal to 0.025 mm, the sand-grain roughness height and the roughness constant were calculated using the Equation (15), and were equal to k_s = 0.28 mm and C_s = 0.874. The simulations were performed with Fluent 6.3.26, and the reference case solved the 3D steady RANS equations with the SST *k-ω* model. In the reference case, a SIMPLE algorithm was used for pressure-velocity coupling, and second order discretization schemes were used. The value of *a* in the turbulent kinetic energy equation was assumed to be 1, and the simulation was stopped when convergence was reached.

Six parameters were tested in this work by Ramponi and Blocken (2012b), and are resumed in Table 5:

- the size of the computer domain, changing the width ($W_D = W + 2d$, where d is the distance from the side walls and the roof to the side and top of the computational domain) and the height ($H_D = H + d$) of the computational domain. The best practice guidelines used in the reference case outperformed the other cases when comparing with the experiments by Karava (2008) and Karava et al. (2011), showing that the results are independent of the cross-sectional dimensions;
- the computational grid resolution analysis showed a good grid convergence between the two higher grid resolutions and also accurate results compared to the experimental ones;
- the inlet turbulent kinetic energy of the atmospheric boundary layer analysis revealed a significant impact of this parameter on the results, being the simulations which used a = 1 that had the best performance, comparing to the results of a = 0.5 (underestimated) and a = 1.5 (overestimated);
- different turbulence model were tested and the SST *k-ω* model was the one with the best results followed by the RNG *k-ε* model;
- the importance of using the appropriate discretization scheme (second-order) was proven;
- the convergence criteria analysis showed that a sufficiently stringent convergence criteria should be used (the ones suggested by the CFD codes are often insufficient).

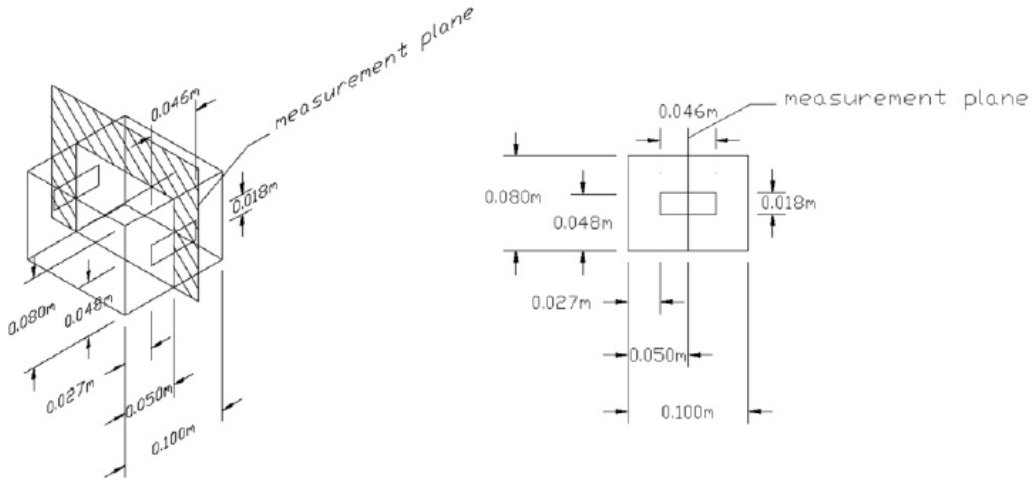

Figure 10 Building model and measurement plane used for PIV measurements by Karava et al. (2011).

Table 5 Overview of computational parameters for sensitivity analysis with indication of the reference case (Ramponi & Blocken 2012b).

	Computational domain size (Section 4.1)	Computational grid resolution (Section 4.2)	Turbulent kinetic energy (Section 4.3)	Turbulence models (Section 4.4)	Discretization schemes (Section 4.5)	Level of iterative convergence (Section 4.6)
Ref. case	$H_D = 5 \times H$	**575,247**	$a = 1$	**SST $k-\omega$**	**2nd order**	**Conv.**
	$H_D = 4 \times H$	314,080	$a = 0.5$	S$k-\varepsilon$	1st order	10^{-4}
	$H_D = 3 \times H$	144,696	$a = 1.5$	R$k-\varepsilon$		10^{-3}
	$H_D = 2 \times H$			RNG $k-\varepsilon$		10^{-2}
	$H_D = 1 \times H$			S$k-\omega$		
				RSM		

Bangalee et al. (2013) performed a study using flow visualization (to observe the three-dimensional and turbulent flow), PIV measurements (to measure the velocity flow fields, similar to the work of Karava (2008) and Karava et al. (2011)) and CFD techniques (to predict the internal flow patterns and the ventilation flow rates). A good agreement between the different data was achieved. The flow fields of four different building configurations (Figure 11) were also compared. The numerical simulations were performed assuming that the system is steady, incompressible, viscous, turbulent, non-buoyant and three dimensional. Water was considered as the working fluid (25ºC and 1 atm), using the RNG *k-ε* turbulence model with a fully structured grid. This study concluded that using multiple openings on both sides of the room increases the ventilation flow rate and ensures a better interior air replacement. Moreover, for fixed wall porosities higher flow rates are obtained when the openings are located in the middle of the walls (the ventilation rate for Case 2 is 34% smaller than for Case 1). Although it is important to notice that the interior air replacement is higher for Case 2 (with oblique opening positions) comparing to Case 1 (facing opening positions) due to the higher interaction of the entering flow and the interior air.

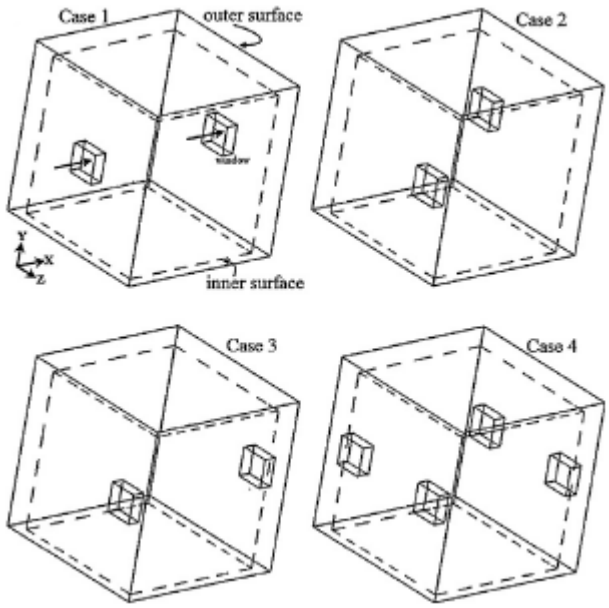

Figure 11 Schematic view of the four different building configurations (Bangalee et al. 2013).

A study about wind-driven cross-ventilation with internal obstacles was performed by Chu and Chiang (2013). In this study a wind tunnel experiment was performed and compared with LES results. A series of simulations were performed changing, one by one, the height (*h*), the width (*b*) and the location (*X/L*) of the obstacle (Figure 12). The building dimensions used were 10 x 10 x 10 m^3 (*W x L x H*). It had two square-sized equal openings at the center of the façades with 2 x 2 m^2 (wall porosity of 10%). It was seen on the results of the two first series that the ventilation rate decreased when the blockage ratio increased. As an example the ventilation rate decreased 20% when the blockage ratio was over 75%. When the location of the obstacle was changed, it was seen that the ventilation flow rates diminished when the obstacle was closer to the inlet/outlet walls, which can be justified by the increase of the flow resistance when the obstacle is near the openings. Another important conclusion was the impact of only 5% on the ventilation rate when the blockage ratio was 30%, thereby obstacles can be neglected when blockage ratio is inferior to that value.

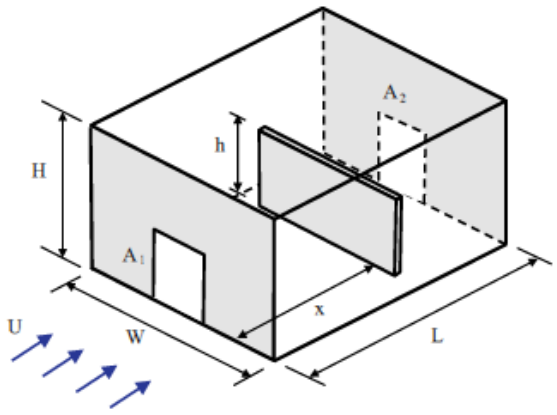

Figure 12 Schematic diagram of the full-scale building with a vertical partition inside (Chu & Chiang 2013).

5. Validation study

This chapter focuses on the numerical simulations that are used for the validation of the numerical model. It focuses on a simple geometry of a generic isolated building subjected to wind-induced cross-ventilation. The numerical simulations are based on the wind tunnel experiments by Karava (2008) and Karava et al. (2011), described in the previous chapter, and their results are used for the validation. The impact of the oscillatory behavior of the residuals, a grid sensitivity analysis and the influence of the upstream length of the domain were tested to understand the impact of these parameters on the numerical simulations.

The building model had a scale of 1:200 and had dimensions 0.1 x 0.1 x 0.08 m^3 (width x depth x height). The walls and the ceiling had a thickness of 2 mm and the windows were located on the center of the walls that were in the flow direction. The windows had the dimensions of 0.046 x 0.018 m^2 (width x height) corresponding to 10% wall porosity.

5.1. CFD simulations

5.1.1. Computational domain and grid

The computational domain used on the simulations was based on the best practice guidelines by Franke et al. (2007) and Tominaga et al. (2008): 5 times the building height (*5H*) from the sides and the top of the building, 15 times the building height (*15H*) behind the building (in the outflow direction) and 5 times the building height (*5H*) from the inlet of the domain till the building. Although, instead of this last guideline, 3 times the building height (*3H*) was used as the distance between the inlet and the building (Blocken et al. 2007a,b) (only in the sensitivity analysis, section 5.3.3, *5H* was tested). The total dimensions of the domain were 0.9 x 1.54 x 0.48 m^3 (width x depth x height).

The computational grid was constructed using the software Gambit 2.4.6 and was built using the surface-grid extrusion technique by van Hooff and Blocken (2010) resulting in a fully structured grid (composed only by hexahedral cells), shown in Figure 13. In this technique the ground plane grid was firstly built and meshed and then, as the name suggests, extruded in the vertical direction. The edges were meshed using exponential and bi-exponential growth ratio, with the second one used on the edges of the building and to the edges parallels to it. The grid had a total of 443,580 hexahedral cells, with the interior of the room and the windows accounting for a total of 42,900 hexahedral cells. The number of nodes on the building edges was 49 on the width direction, 37 on the depth direction and 46 on the vertical direction, accounting with 4 nodes in each wall of the building, which ensures a good grid resolution (Franke et al. 2007). The height of the first cell in the vertical direction was equal to 0.0007 m and, as a consequence, y_p = 0.00035 m (half of the first cell height in the vertical direction).

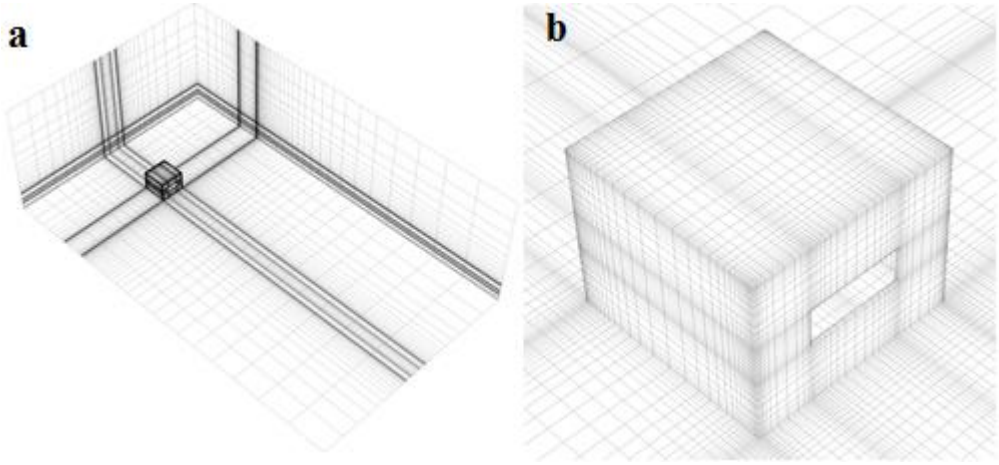

Figure 13 Computational grid (443,580): (a) Perspective of the inlet, bottom, side and building of the computational domain; (a) Perspective view of the building and ground surface grid.

5.1.2. Boundary conditions

The boundary conditions used on these simulations were defined based on the vertical streamwise profiles of turbulence intensity I_u and mean wind speed U, measured by Karava (2008) and Karava et al. (2011), being at the building height (0.08 m): TI = 10% and U_{ref} = 6.97 m s^{-1} (Figure 6). The inlet wind velocity profile was defined using the logarithmic law (Equation (7)), where the roughness length (z_0) was equal to 0.025 mm. The turbulent kinetic energy was then defined using Equation (12), where a equals to 1 (Ramponi and Blocken 2012a,b; Tominaga et al. 2008). The turbulence dissipation rate was defined using Equation (13) and subsequently the specific dissipation rate using Equation (14). The inlet profiles can be seen in Figure 14. For the ground plane, to ensure the effects of the upstream roughness on the development of the flow, boundary conditions were imposed based on the standard wall functions by Launder and Spalding (1974) with roughness modification by Cebeci and Bradshaw (1977). The sand-grain roughness height, k_s, was considered equal to 0.3 mm and was defined based on the height of the first cell (y_p = 0.7 mm), due to the necessity to ensure that the sand-grain roughness height was smaller than half of the first cell height in the vertical direction ($k_s < y_p$) (Blocken et al. 2007a,b). The roughness constant was calculated using Equation (15), C_s = 0.816. To the top and to the sides of the computational domain symmetry boundary conditions were aplied. This way it was ensured that zero normal velocity and zero normal gradient for all variables were applied. On the outlet zero static pressure was applied and standard wall functions were applied to the walls of the building, with k_s = 0 corresponding to a smooth wall.

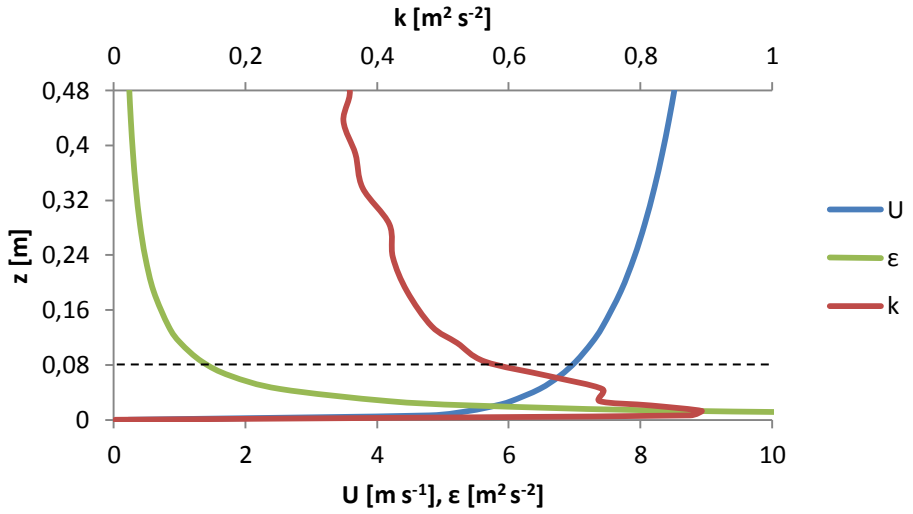

Figure 14 Inlet profiles of mean wind speed (U), turbulent kinetic energy (k) and turbulence dissipation rate (ε).

5.1.3. Other computational parameters and settings

The computational simulations were performed using the commercial code ANSYS Fluent 12.1.4. This software was used to solve the 3D steady RANS equations with the shear-stress transport (SST) *k-ω* turbulence model as recommended by Ramponi and Blocken (2012a). The SIMPLE algorithm was used for pressure-velocity coupling. Second-order discretization schemes were used for the viscous and convection terms of the governing equations and second order was also used for pressure interpolation. The simulation was assumed to be converged when all the residuals had leveled off: the *x*, *y* and *z* velocities had reached values below 10^{-6}, the turbulent kinetic energy had reached values below 10^{-5} and the continuity and the specific dissipation rate had got to values below 10^{-4}. The residuals can be seen in Figure 15 and show an oscillatory behavior. To avoid inaccurate results due to the existence of oscillations, the results can be averaged over a certain number of iterations. This will be discussed in chapter 5.3.1.

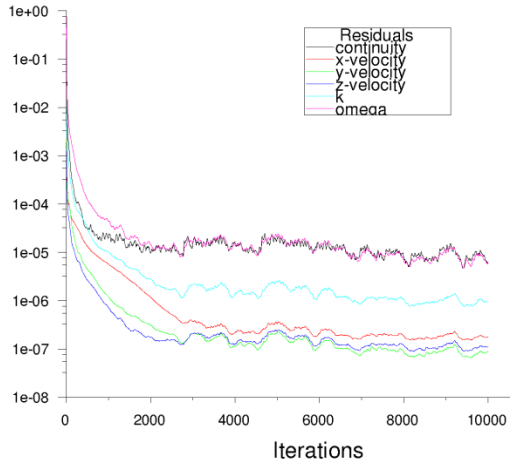

Figure 15 Scaled residuals monitored during 10,000 iterations.

5.2. Results and comparison with PIV experiments

After the simulation had converged, the results were obtained and compared with the experimental results by Karava et al. (2011) and Karava (2008) to validate this reference case. The results were compared in two different ways: comparing the velocity vector fields at a vertical and at a horizontal center plane of the building, and comparing the streamwise wind speed ratio along the centerline of the building.

In Figure 16 it is possible to observe the velocity vector field on the vertical mid-plane for the PIV experiments and for the simulation results. It can be seen that the main jet passes through the center of the inlet opening, experiences acceleration after the window with a downward direction, decelerates in the center of the building and accelerates again at the outlet opening being directed on the upward direction after leaving the building. In addition it is possible to observe before the inlet opening two slower moving zones located above (directed to the roof of the building) and below (creating a standing vortex near the ground) of the main jet. The existence of this standing vortex combined with the position of the inlet opening (in the center of the inlet wall) is the reason to the downwards direction of the flow when it enters the building. A small recirculation zone is also noticeable inside the building near the inlet window below the main jet. On the leeward wall, some of the jet remains inside the building and is directed to the top, travelling subsequently to the windward wall (in opposite to the main flow) where it drops and joins the main jet. After the leeward opening, below the main jet is possible to observe a recirculating zone, originated by an under pressure zone which is caused by the presence of the building (Beranek and Van Koten 1979). On the roof of the building a separation zone is clearly depicted.

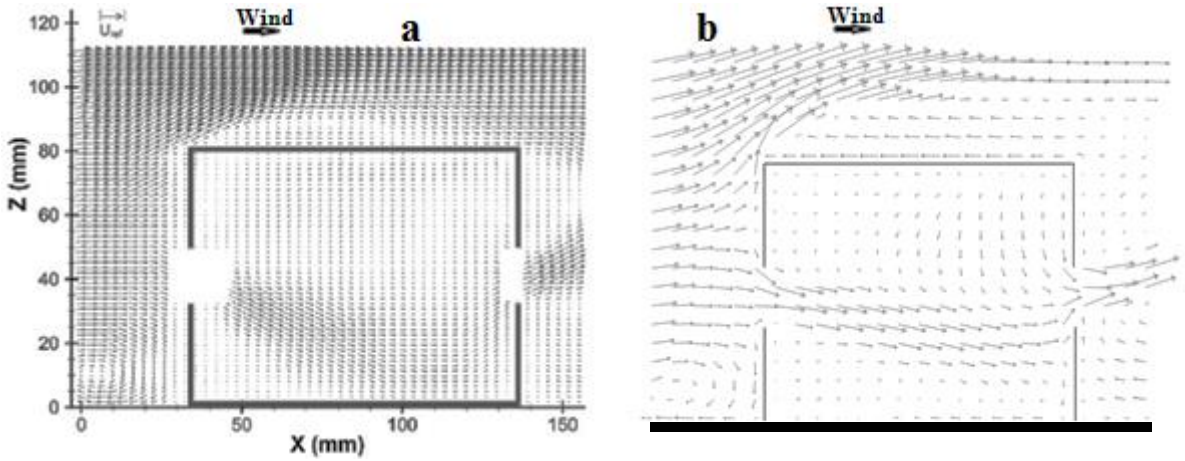

Figure 16 Comparison of the velocity vector fields on the vertical mid-plane between: (a) the PIV measurements and (b) the CFD simulation on the vertical mid-plane scaled by a factor of 8.

In Figure 17, the velocity vector field on the horizontal mid-plane of the building (h = 0.04 m) is shown for the PIV experiments and for the numerical simulation results. The main jet passing right through the two openings is clearly visible. It is also possible to observe two slow moving zones on both sides of the jet, driven by the main jet, and that near the side-walls they have an opposite direction to the main jet. It can be seen that the flow is symmetric, considering that it is divided by the center of the building openings. Outside the building a separation zone is seen on both windward corners of the building. On the PIV experiments, shadows originated by the building edges (due to the fact that the edges are not transparent and the laser sheet cannot pass through) can be seen in the PIV image, on the zones with the dashed circles. When the flow leaves the room, it can be seen that it tends to the right side of the figure (left side of the flow path, close up view in Figure 18) as in the CFD simulation (although clearer in this case). The difference can be explained by the fact that the flow is not steady and it is constantly changing (which can be verified by the oscillatory behavior of the residuals) and, if the simulation were stopped at a different time, a different flow field would be obtained (although very similar). To avoid this oscillatory behavior of the flow, the results could have been averaged over a certain number of iterations. In this study, however, the results presented were not averaged and were obtained from the moments where convergence was assumed to be achieved.

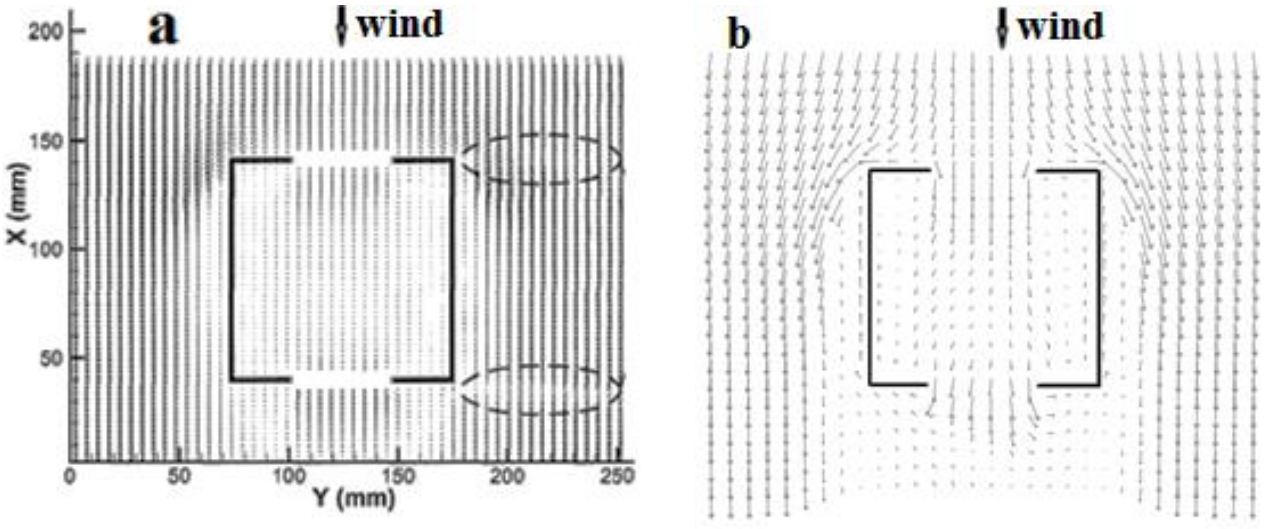

Figure 17 Comparison of the velocity vector fields on the horizontal mid-plane (h = 0.04 m) between (a) the PIV measurements and (b) the CFD simulation scaled by a factor of 8.

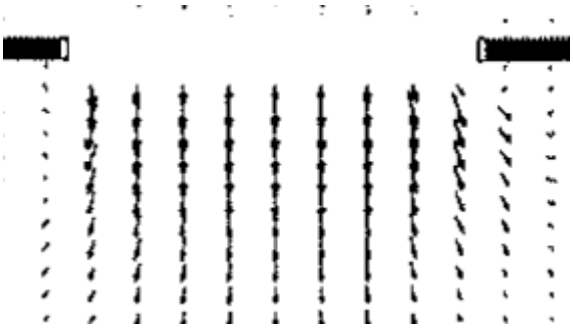

Figure 18 Close up view of the velocity vector field after the outlet opening in the PIV measurements.

Figure 19 shows the streamwise wind speed normalized by the reference velocity (U_{ref} = 6.97 m s^{-1}) on a center-line passing between the two openings. It is possible to observe that the numerical model tends to overestimate the velocity, mainly around the openings which can be explained by the fact that the PIV experiments in those zones are subjected to reflection and shading effects. The overall flow shows a good agreement between the two sources of results. The minimum values of velocity ratio are similar and the behavior of the flow is well reproduced, both inside and outside of the building model.

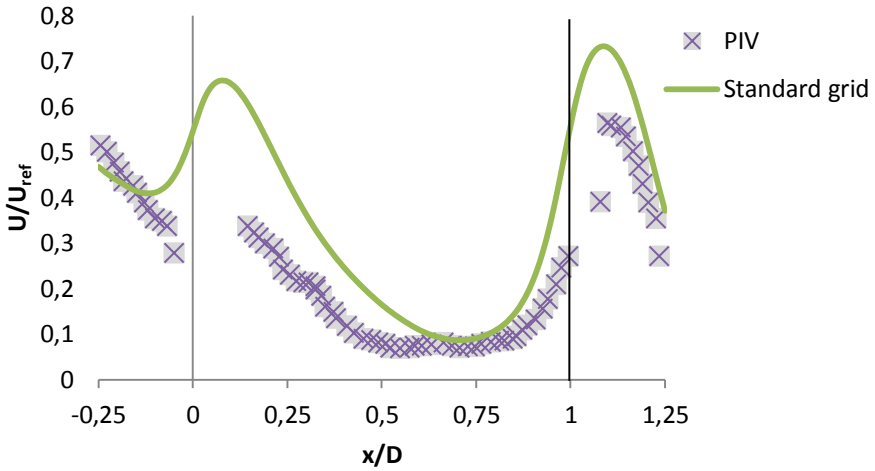

Figure 19 Comparison between the PIV measurements and the CFD simulations for the streamwise wind speed normalized by the reference velocity, on a center-line passing between the two openings (h = 0.04 m).

5.3. Sensitivity analysis

Beyond the comparison with the PIV measurements, three different sensitivity analyses were performed to ensure that the grid and the computational parameters chosen were the most accurate. For this reason the impact of the oscillations on the streamwise wind speed, a grid-sensitivity analysis and a test on the impact of the size of the upstream length of the domain (distance from the inlet of the computational domain to the building) were performed.

5.3.1. Oscillatory behavior of the residuals

In order to understand the impact that the oscillations visible in the residuals have on the simulation results a sensitivity study was performed. In this sensitivity study, the results of the streamwise wind speed normalized by the reference velocity on a center-line passing between the two openings were registered for every 40 iterations after convergence was reached (10k iterations) for 440 iterations.

In Figure 20 the results can be seen for the PIV measurements, the 10k iterations (standard building case), 360 iteration after convergence was reached (where the most different results were obtained) and for the average of the 440 iterations done after the convergence was reached. The results of the 360 iteration case show a better agreement with the PIV measurements compared to the average of the 440 iterations and even better compared to the results of the standard case. Although, when compared the average of the 440 iterations and the standard case only a slightly different is visible.

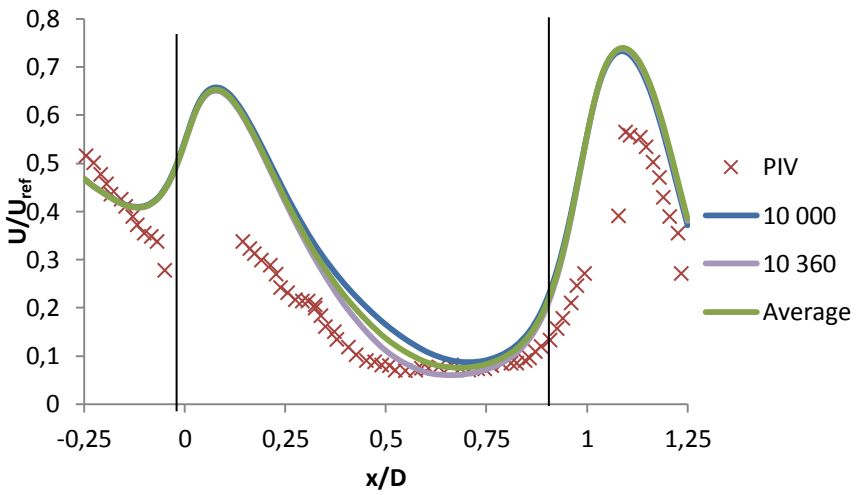

Figure 20 Comparison between the PIV measurements and the different CFD simulations for the streamwise wind speed normalized by the reference velocity, on a center-line passing between the two openings (h = 0.04 m).

5.3.2. Grid-sensitivity analysis

A grid-sensitivity analysis was performed to ensure that the grid resolution had no impact on the computational results. Two different grids were constructed based on the grid previously used, which will be called from now on standard grid (443,580 cells). The grids were obtained either by coarsening or refining the number of nodes of the standard grid with a factor of $\sqrt{2}$ in each direction, resulting in a factor of, approximately, 2.8 in the total number of cells of the domain. The coarser grid had a total of 153,303 cells and the finer grid a total of 1,216,068 cells. In Figure 21 the three different grids utilized during this analysis are shown.

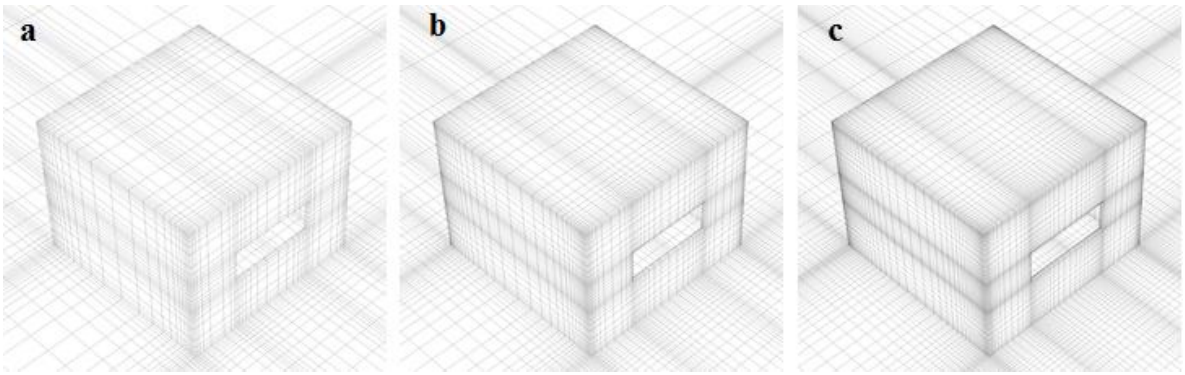

Figure 21 Perspective view of the building and ground surface grid: (a) Coarser grid with 153,303 cells; (b) Standard grid with 443,580 cells; (c) Finer grid with 1,216,068 cells

In Figure 22 are shown the results for the three different grids of the streamwise wind speed normalized by the reference velocity (U_{ref} = 6.97 m s^{-1}) on a center-line passing between the two openings. The three grids show really similar results, with the standard and the finer grid having a perfect match. Small discrepancies can be seen between the coarser and the other two grids. The

coarser grid tends to under predict the flow, being most pronounced on the region after the inlet opening and after the outlet region. In terms of the volume flow rate on the inlet opening, the deviation between the standard grid and the coarser grid is less than 3%.

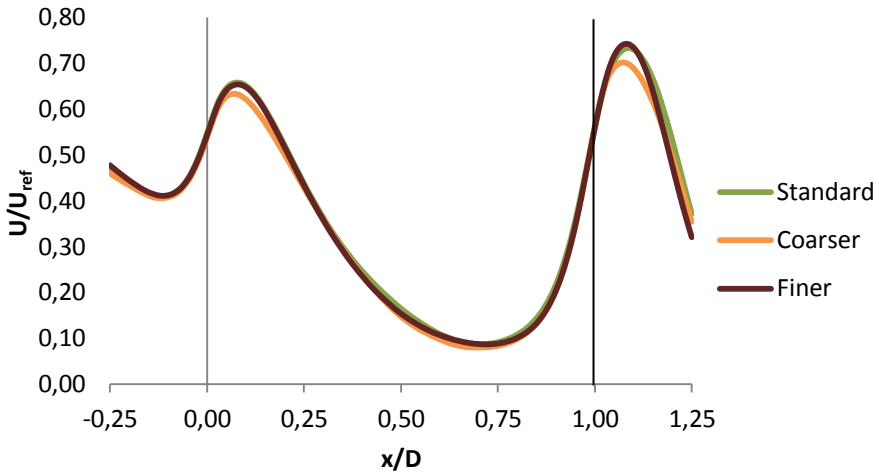

Figure 22 Comparison of the streamwise wind speed normalized by the reference velocity, on a center-line passing between the two openings (h = 0.04 m) for the three different grids.

5.3.3. Upstream length of the domain

A test on the impact of the size of the upstream length of the domain, distance between the inlet of the computational domain and the building, was performed to ensure that the dimension chosen for the standard grid was the most accurate. For this reason a different grid was constructed following the best practice guidelines (Franke et al. 2007; Tominaga et al. 2008), considering the upstream length of the domain to be 5 times the building height (*5H*), instead of the 3 times the building height (*3H*) used in the standard grid as was recommended by Blocken et al. (2007a,b). The resulting grid can be seen in Figure 23, with the grid with *5H* accounting a total of 448,788 hexahedral cells.

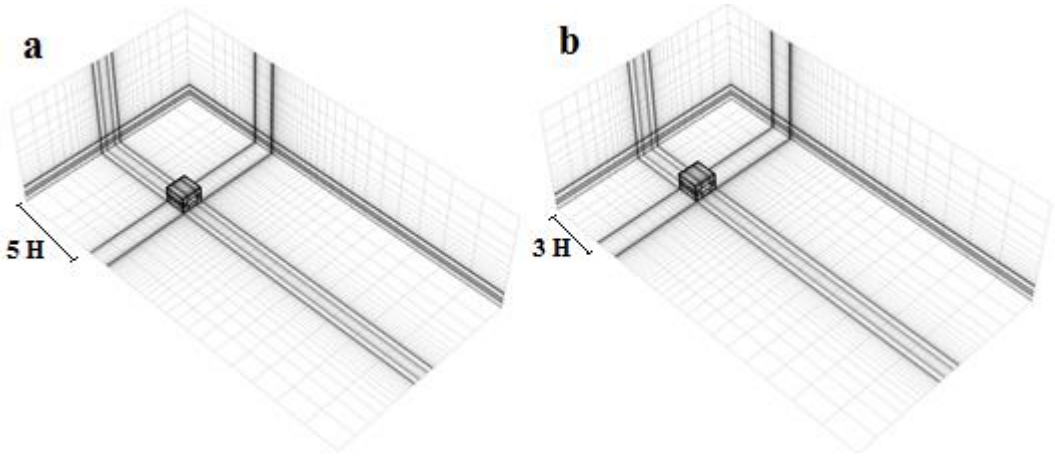

Figure 23 Perspective of the inlet, bottom, side and building of the computational domain: (a) Upstream length of the domain equal to 5H; (b) Standard grid with upstream length of the domain equal to 3H.

In Figure 24 is shown the comparison between the two different grids, *3H* (standard) and *5H* grid, of the streamwise wind speed normalized by the reference velocity on a line passing between the centers of the two openings. It is seen that the grid with the biggest length between the inlet of the domain and the building tends to overpredict the velocity on the center of the building (between *x/D* = 0.4 and *x/D* = 0.8) being on the rest of the line very similar to the values obtained with the standard grid. There is a slight exception after both openings where the *5H* grid under predicts the flow. The volume flow rates on the inlet opening were also compared and the results showed that the grid with the biggest upstream length of the domain under predicts the volume flow rate in less than 3% comparing to the standard case.

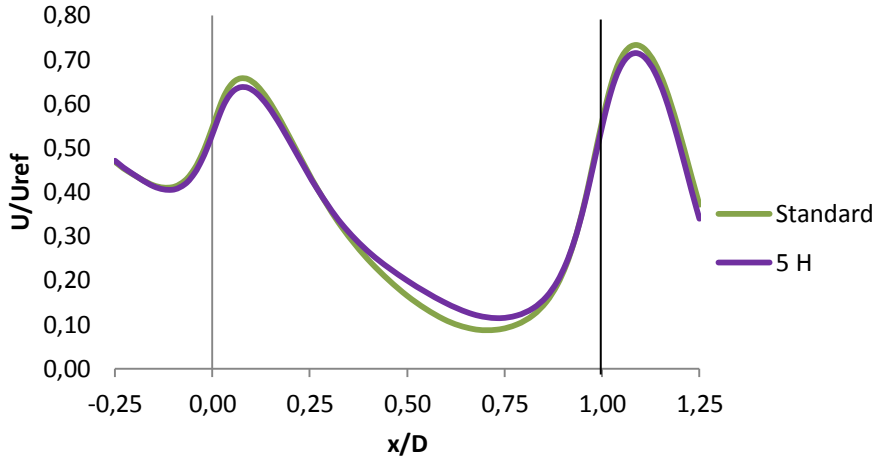

Figure 24 Comparison of the streamwise wind speed normalized by the reference velocity, on a center-line passing between the two openings (h = 0.04 m) for the standard grid (3H) and the 5H grid.

5.4. Discussion and conclusions

The validation study showed a good agreement between the CFD simulations and the PIV measurements. Although, as noted, small differences exist between those two, which can be explained by the fact that the PIV measurement have some inaccuracies due to reflections and shading effects, as was reported by Karava et al. (2011) and Karava (2008).

The results from the comparison between the numerical simulations and the PIV measurements indicate that the computational domain and the computational parameters and settings used in the CFD simulations were correctly chosen. Also three different sensitivity analysis studies were performed. The first one with the intent to understand the impact of the oscillations (seen in the residuals) in the streamwise wind speed, the second to understand if the grid resolution chosen was the most correct and the third to understand if the upstream length of the computational domain should be 3 or 5 times the building height. On the first, it was concluded that the oscillation can have an impact on the streamwise wind speed (seen in the difference between the standard case and the 360 iteration case). However, when averaging the results over a certain number of iterations this impact is substantially reduced (as could be seen in the difference

between the average and the two other cases). On the second study, it was concluded that the grid resolution chosen in the standard case (which was used to do the comparison with the PIV measurements) was correct due to its high level of agreement with the coarser grid and even higher level of agreement with the finer grid. Regarding the last sensitivity study it was concluded that the upstream length of the computational domain should be 3 times the building height, as used in the standard case, due to its higher accuracy on predicting the flow.

It can be concluded that the grid resolution and the computational parameters and settings used in this study had a good agreement with the PIV measurements. Therefore the information collected in this chapter will be used in the next phase of this thesis.

6. Different building geometries

In this chapter a series of simulations of different building geometries were performed to understand how the building geometries affect cross-ventilation. Two different kinds of modifications were applied to the building: changing the building depth based on the height (H) of the building (2.5 *H*, 5 *H* and 10 *H*) and dividing the building into two different zones linked by a door opening (in the center, near the inlet window and near the left side wall). Due to the high velocities verified inside the building used on the validation case, the wind profile was scaled to reduce these velocities. The different building geometries were analyzed and compared based on the values obtained of the volume flow rate, the CO_2 concentration, the mean age of air and the air exchange efficiency.

To better understand the meaning of the values obtained during the post processing of the simulations, the building was scaled using a factor of 30 resulting in a building with dimensions 3.0 x 3.0 x 2.4 m^3 (width x depth x height) for the standard case. The walls and the ceiling had a thickness of 0.06 m, and the windows were located in the center of the walls that were in the flow direction. The windows had the dimensions of 1.38 x 0.54 m^2 (width x height), corresponding to 10% wall porosity. The partitioned wall had a thickness of 0.06 m and the door opening located in it had dimensions 0.9 x 2.0 m^2 (width x height) leading to a wall porosity of 26.7%.

6.1. CFD simulations

6.1.1. Computational domain and grid

The computational domains used in this chapter were defined using similar values to the ones used in the validation study (chapter 5.1.1): 5 times the building height (*5H*) from the sides and the top of the building, 15 times the building height (*15H*) behind the building (in the outflow direction) (Franke et al. 2007; Tominaga et al. 2008) and 3 times the building height (*3H*) was used as the distance between the inlet and the building (Blocken et al. 2007a,b). The total dimensions of the domain varied with the building depth: 27 x 46.2 x 14.4 m^3 for the standard case; 27 x 49.2 x 14.4 m^3 for the case with the building depth 2.5 times the building height; 27 x 55.2 x 14.4 m^3 for the case with the building depth 5 times the building height; 27 x 67.2 x 14.4 m^3 for the case with the building depth 10 times the building height.

The computational grid was constructed using a similar procedure to the one used in the validation study (chapter 5.1.1). The software Gambit 2.4.6 was used to build a fully structured grid using the surface-grid extrusion technique by van Hooff and Blocken (2010). The edges were meshed using exponential and bi-exponential growth ratio, being the second one utilized on the edges of the building and to the edges parallel to it. In Table 6 it is possible to observe the total number of cells for the different building geometries. The different meshes were constructed using the same ratio of nodes per length of the edge used in the validation case. The height of the first cell in the vertical direction was equal to 0.021 m and as a consequence y_p = 0.0105 m (half of the first cell height in the vertical direction).

Table 6 Total number of cells for the different building geometries simulated.

	Standard				2.5 H				5 H	10 H
	Simple	Door			Simple	Door			Simple	Simple
		Center	Inlet	Side		Center	Inlet	Side		
Cells	443,580	560,888	566,770	853,176	583,998	737,348	737,348	853,176	869,676	1,431,348

6.1.2. Boundary conditions

The boundary conditions used in these simulations were defined based on the streamwise vertical profiles of turbulence intensity I_u and mean wind speed U, measured by Karava (2008) and Karava et al. (2011), being at the building height (0.08 m): TI = 10% and U_{ref} = 6.97 m s^{-1} (Figure 6). Although, since lower velocities were desired inside the building, the reference velocity was set to be 1.5 m s^{-1} at the building height (0.08 m corresponding to 2.4 m in the scaled version). This way the velocities inside the room would be closer to the values recommended by the ANSI/ASHRAE (2007) thermal comfort standard, which states that air velocities should be lower than about 0.5 m s^{-1} in the occupied zone. The inlet wind velocity profile was defined using the logarithmic law (Equation (7)), where the roughness length (z_0) was equal to 0.75 mm (applying a scaling factor of 30 on the original roughness length, 0.025 mm). With the wind velocity profile, the turbulent kinetic energy was defined, using Equation (12), where a equals to 1 (Ramponi and Blocken 2012a,b; Tominaga et al. 2008). The turbulence dissipation rate was then defined using Equation (13), followed by the specific dissipation rate (Equation (14)). The inlet profiles can be seen in Figure 25. For the ground plane, to ensure the effects of the upstream roughness on the development of the flow, boundary conditions were imposed based on the standard wall functions by Launder and Spalding (1974) with roughness modification by Cebeci and Bradshaw (1977). The sand-grain roughness height, k_s, was considered equal to 0.009 m and was defined based on the height of the first cell (y_p = 0.021 m), due to the necessity to ensure that the sand-grain roughness height was smaller than half of the first cell height in the vertical direction ($k_s < y_p$) (Blocken et al. 2007a,b). The roughness constant was then calculated using Equation (15), equals to C_s = 0.816. To the top and to the sides of the computational domain symmetry boundary conditions were aplied. It ensured that zero normal velocity and zero normal gradient for all variables were applied. On the outlet zero static pressure was applied and standard wall functions were applied to the walls of the building, with k_s = 0 corresponding to a smooth wall.

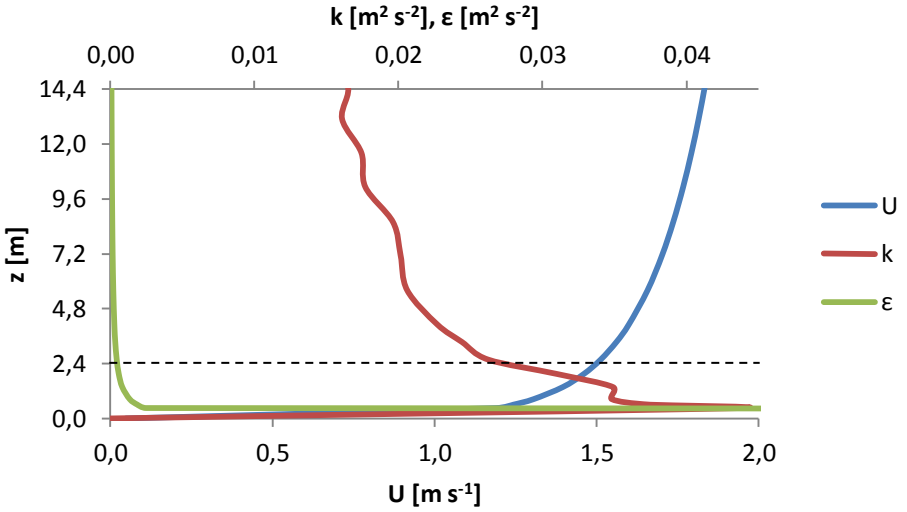

Figure 25 Scaled inlet profiles of mean wind speed (U), turbulent kinetic energy (k) and turbulence dissipation rate (ε).

6.1.3. Other computational parameters and settings

The computational simulations were performed using the commercial code ANSYS Fluent 12.1.4, with the exception of the simulations of the mean age of air which were performed using ANSYS Fluent 14.0. The first was used to solve the 3D steady RANS equations with the shear-stress transport (SST) *k-ω* turbulence model as recommended by Ramponi and Blocken (2012a). The SIMPLE algorithm was used for pressure-velocity coupling. Second order discretization schemes were used for the viscous and convection terms of the governing equations and second order was also used for pressure interpolation. The simulation was assumed to be converged when all the residuals had leveled off: the *x*, *y* and *z* velocities had reached values below 10^{-6}, the turbulent kinetic energy had reached values around 10^{-5} and the continuity and specific dissipation rate reached values around 10^{-4}.

6.1.4. Mean age of air, air exchange efficiency and CO_2 concentration

After the CFD simulations had converged, two different simulations were performed: the first to determine the mean age of air in the interior of the building and the second to determine the CO_2 concentrations in the computational domain. To determine the mean age of air inside the building an user-defined function (UDF) was used. The simulations used second order discretization schemes and were performed till convergence was achieved (approximately 100 iterations) and with the flow and turbulence equations disabled. The air exchange efficiency was then calculated using (1), where τ_n is the area-weighted average of the mean age of air on the outlet opening and τ the mean age of air in the building.

To determine the CO_2 concentration the species transport model was used. At the inlet of the domain the inlet flow was considered to have a constant value of 400 ppm of CO_2 and inside the building a constant releasing source of CO_2 of 5.5 x 10^{-7} kg m^{-3} s^{-1}. This value was calculated using Equation (16) and considering that an average sedentary adult (M = 70 W m^{-2} and A = 1.8 m^2) produces 5.04 m^3 s^{-1} of CO_2 ((2)), an occupation of 7 m^2 per person (NEN 1824:2010 2010) and a density of CO_2 equal to 1.7878 kg m^{-3} (value used by ANSYS Fluent 12.1.4).

$$Source = G \times \rho_{CO_2} \times \frac{Area_{surface}}{Area_{person}} \times \frac{1}{Volume} \quad (16)$$

The simulations used second order discretization schemes and were performed till convergence was achieved (about 400 iterations) and with the equations of the flow and turbulence disabled.

6.2. Different building depth

In order to understand the impact of the building depth on cross-ventilation, four different building configurations were simulated:

- standard case with 3 meters depth (similar to the building used on chapter 5);
- 2.5 times the building height corresponding to a depth of 6 meters;
- 5 times the building height (the limit for cross-ventilation accordingly to Awbi (2003)) corresponding to 12 meters depth;
- 10 times the building height corresponding to a depth of 24 meters.

To better understand and compare the different building depth simulations, several values (volume flow rate, air exchange rate, CO_2 concentration, mean age of air and air exchange efficiency) and images (CO_2 concentration and velocity vector fields at different positions of the room) were used. The velocity vector fields shown in this chapter are all scaled by a factor of 8.

6.2.1. Standard building

Figure 26 shows the velocity vector field in the vertical mid-plane. It can be seen that this velocity vector field is similar to the ones in Figure 16, despite the fact that the building had been scaled by a factor of 30 and the inlet wind profile had also been scaled. Figure 27 shows the velocity vector field on the horizontal mid-plane (*h* = 1.2 m). As in the vertical mid-plane velocity vector field, the resulting image is similar to the one shown in the validation case (Figure 17), with all the main features of the flow clearly depicted. This shows that the scaling of the two components had no impact on the flow field inside and near the building, other than the absolute values of velocities registered.

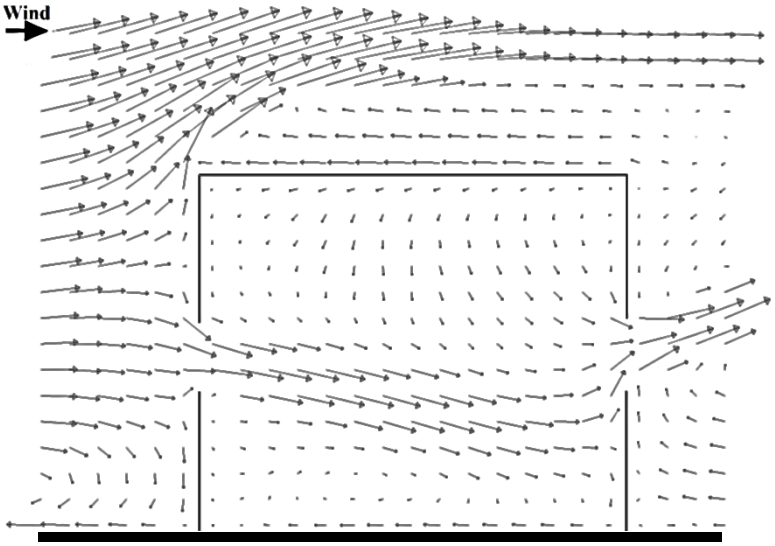

Figure 26 Velocity vector field on the vertical mid-plane of the standard building depth.

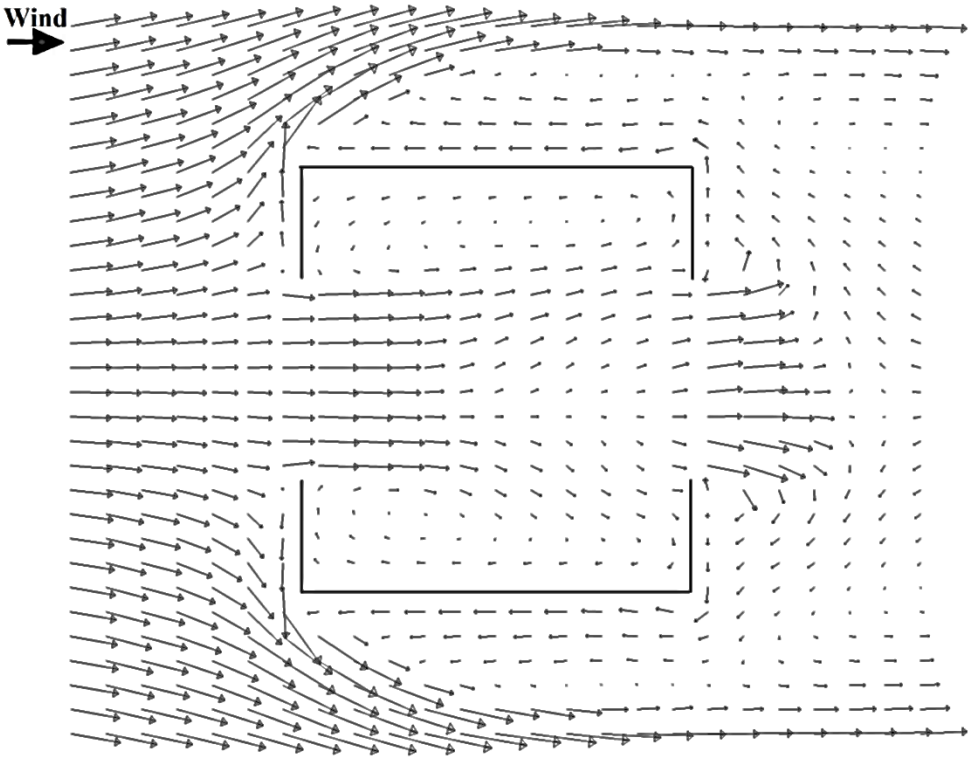

Figure 27 Velocity vector field on the horizontal mid-plane (h = 1.2 m) of the standard building depth.

The volume flow rate at the inlet opening was 0.539 $m^3 s^{-1}$, which corresponds to an air exchange rate (ratio between the volume flow rate entering in the building and the volume of the building, and is expressed in air exchanges per hour, ACH) of 100 ACH. The mean age of air registered inside the building was 34.4 seconds and the area-weighted average of the mean age of air on the outlet opening equal to 34.2 seconds, resulting in an air exchange efficiency (ratio between the minimum time for replacing the air in the room and the actual time the air is in the room) of 49.7%. The CO_2

concentration inside the room was 415 ppm (only 15 ppm higher than the outside concentration), although values of 427 ppm were registered. As can be seen in Figure 28 and Figure 29 the CO_2 concentration is dependent of the flow entering the building. The outlet air enters the building and is directed downwards, being in this regions registered the lowest values of CO_2 (similar to the values registered outside of the building, approximately 400 ppm). The flux continues with a downward direction till the outlet window, where it leaves the room and is directed upwards. The existence of this downward direction flux, leads to the existence of lower concentrations of CO_2 in the second half of the building near the ground surface, compared to the rest of the building. The existence of two recirculation zones, reported in chapter 5.2 and also visible in Figure 27, is also noticeable by the existence of two zones with higher concentrations of CO_2: one, smaller, below the inlet window and the other above the main jet (Figure 28a-c). On the horizontal planes (Figure 29a-c) it is possible to see that the flow is symmetric, considering the center of the building openings, as previously reported (chapter 5.2 and Figure 27). Although, at 1.7 m (Figure 29d) the flow is asymmetric, with registered higher concentrations at the left side of the building close to the inlet wall. This asymmetry can be caused by the oscillatory converge observed in the residuals and the fact that the results were not averaged. This behavior can make the flow to tend more to the left or to the right side of the building depending on the instant when the results were collected and for this reason an asymmetric concentration of CO_2 is visible.

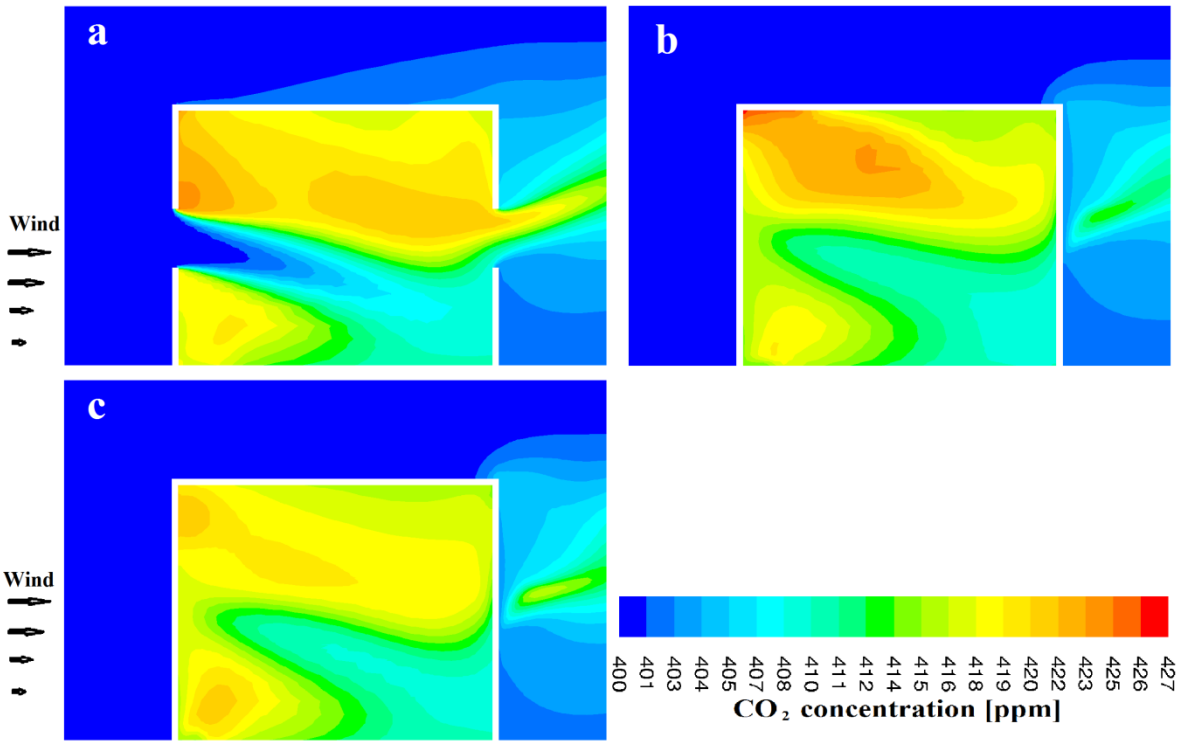

Figure 28 CO_2 concentration on the standard building depth: (a) Vertical center mid-plane; (b) Vertical left-plane (0.75 m to the left of the mid-plane); (c) Vertical right-plane (0.75 m to the right of the mid-plane).

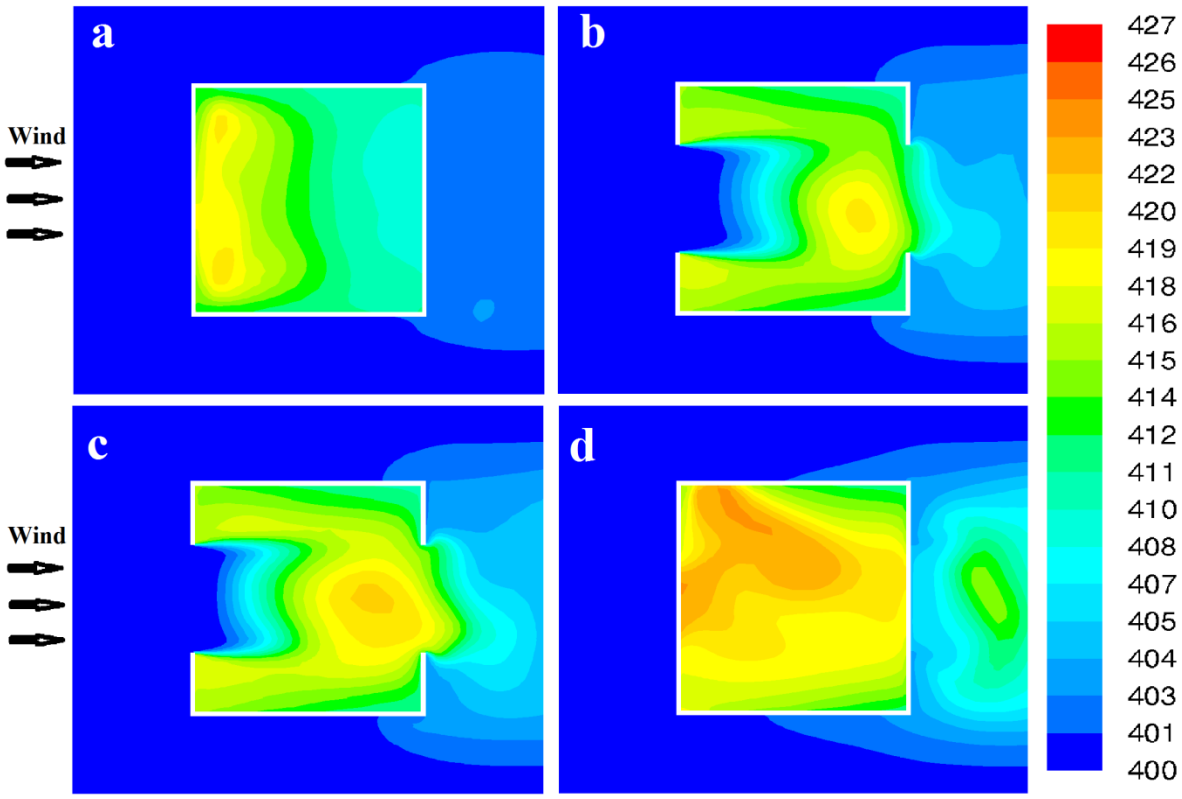

Figure 29 CO_2 concentration on the standard building depth: (a) Horizontal 0.1 m plane; (b) Horizontal 1.1 m plane; (c) Horizontal mid-plane (1.2 m); (d) Horizontal 1.7 m plane.

6.2.2. 2.5 times the building height

Figure 30 shows the velocity vector field on the vertical mid-plane. It can be seen that the main jet enters the room through the inlet window, where it obtains acceleration and is directed downwards. In the middle of the building the main jet has already decelerated and travels near the ground till the outlet wall. Subsequently it is directed to the outlet opening, leaving the building and being accelerated with an upward direction. The flow that does not leave the room is directed to ceiling, circulating till the inlet wall where it drops and joins the main jet, forming a recirculation zone with its center in the middle of the building. Recirculation zones are also seen near the ground before the inlet opening, below the main jet just after the inlet opening and after the outlet window also below the main jet (similar to the ones present in the standard case, Figure 26).

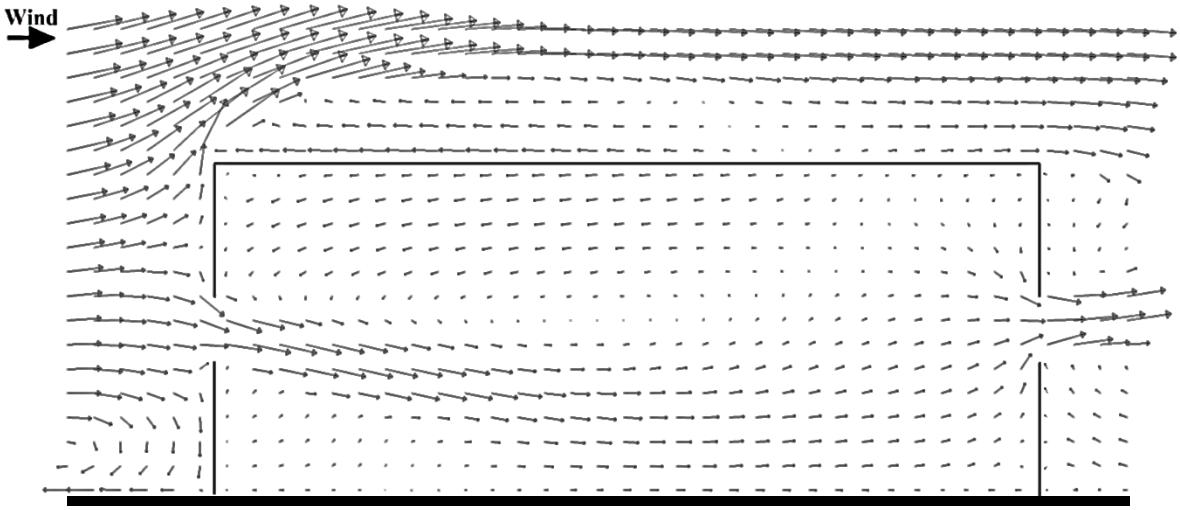

Figure 30 Velocity vector field on the vertical mid-plane of the 2.5 H building depth.

In Figure 31, the velocity vector field on the horizontal mid-plane of the building (h = 1.2 m) is represented. It can be seen that, contrary to the standard building case (Figure 27) the flow inside the building is asymmetric (probably due to the existence of an oscillatory behavior of the flow, which is reported in the residuals). The flow, after being accelerated when entering the building, suffers a deceleration and is directed to the left side of the building, traveling near the left side wall till it is close to the outlet wall. At this point it is directed to the outlet window, accelerating when passing through it, being higher velocities registered on the left side of the opening. It can be seen a small recirculation zone between the main jet and the outlet wall. Two other small recirculating regions can be found just after the inlet opening on both sides of the inlet wall, being more noticeable on the right side of the building. On the center of the building is observed a recirculating zone that on the right side of the building is directed to the inlet window. On the right side of the building is also possible to see another recirculation zone, formed between the right side wall (flowing to the outlet wall) and the flow affected by the recirculation zone existing on the center of the building (flowing to the inlet wall).

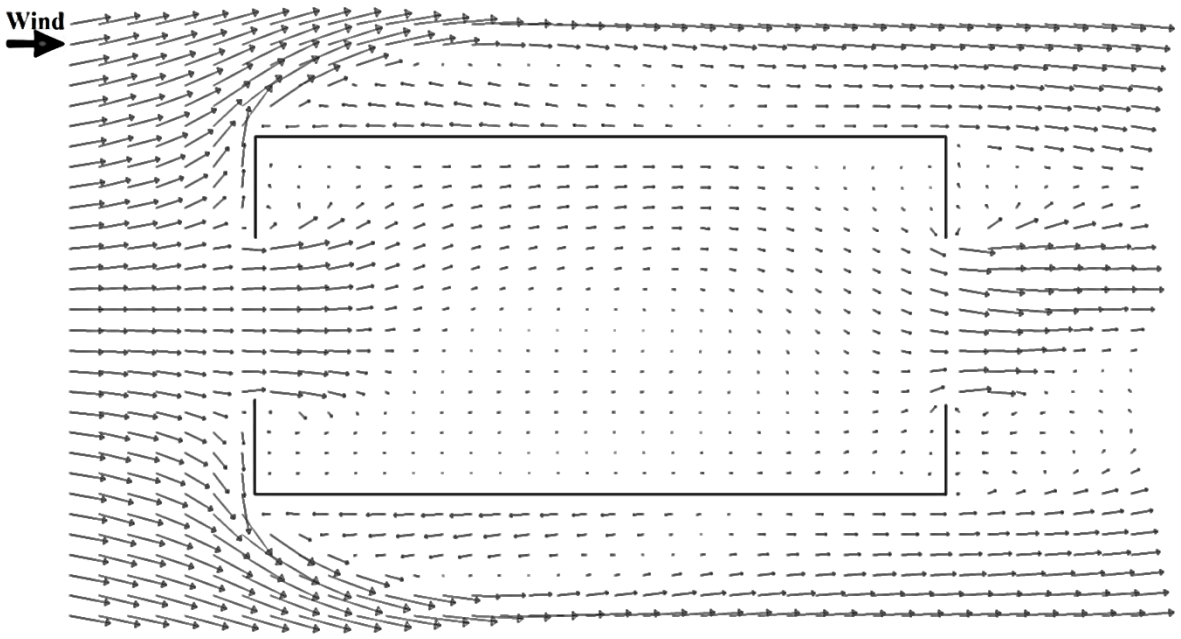

Figure 31 Velocity vector field on the horizontal mid-plane (h = 1.2 m) of the 2.5 H building depth.

On the inlet opening a volume flow rate of 0.528 m^3 s^{-1} was registered, resulting on an air exchange rate of 48 ACH. The mean age of air inside the building was 68.1 seconds, and on the outlet opening an area-weighted average of 70.0 seconds was reported, resulting on an air exchange efficiency of 51.4%. The average concentration of CO_2 inside the room was 431 ppm with a maximum value of 462 ppm being registered. In Figure 32 is possible to observe the CO_2 concentration in different planes of the building. It can be seen the impact that the flow jet entering the room and the flow patterns discernable inside the room have on the CO_2 concentration. The lowest values of CO_2 are found on the inlet opening and just after it, on the downwards direction (following the same pattern as the main jet). The highest concentrations of CO_2 can be found on the left side of the inlet wall either at the top or at the bottom of the building. It can be observed a clear difference between the left side (Figure 32b) and the right side (Figure 32c) planes. On the left side higher concentrations are found, predominantly on the top and bottom corners of the building. On the other hand, on the mid-height of the building due to the existence of high velocities, lower concentration values are found (also observed in Figure 32e-f). On the right side of the building the flow has a clear downward direction. This leads to lower concentration values near the ground and to higher circulation of the air through this entire building zone, leading to lower concentrations when comparing to the left side (Figure 32d,g). It is interesting to notice that the flow on the right side of the building (where lower concentrations are found) has a bigger component on the vertical plane, while the left side of the building (where higher concentrations are detected) has a bigger component on the horizontal plane (mid-height).

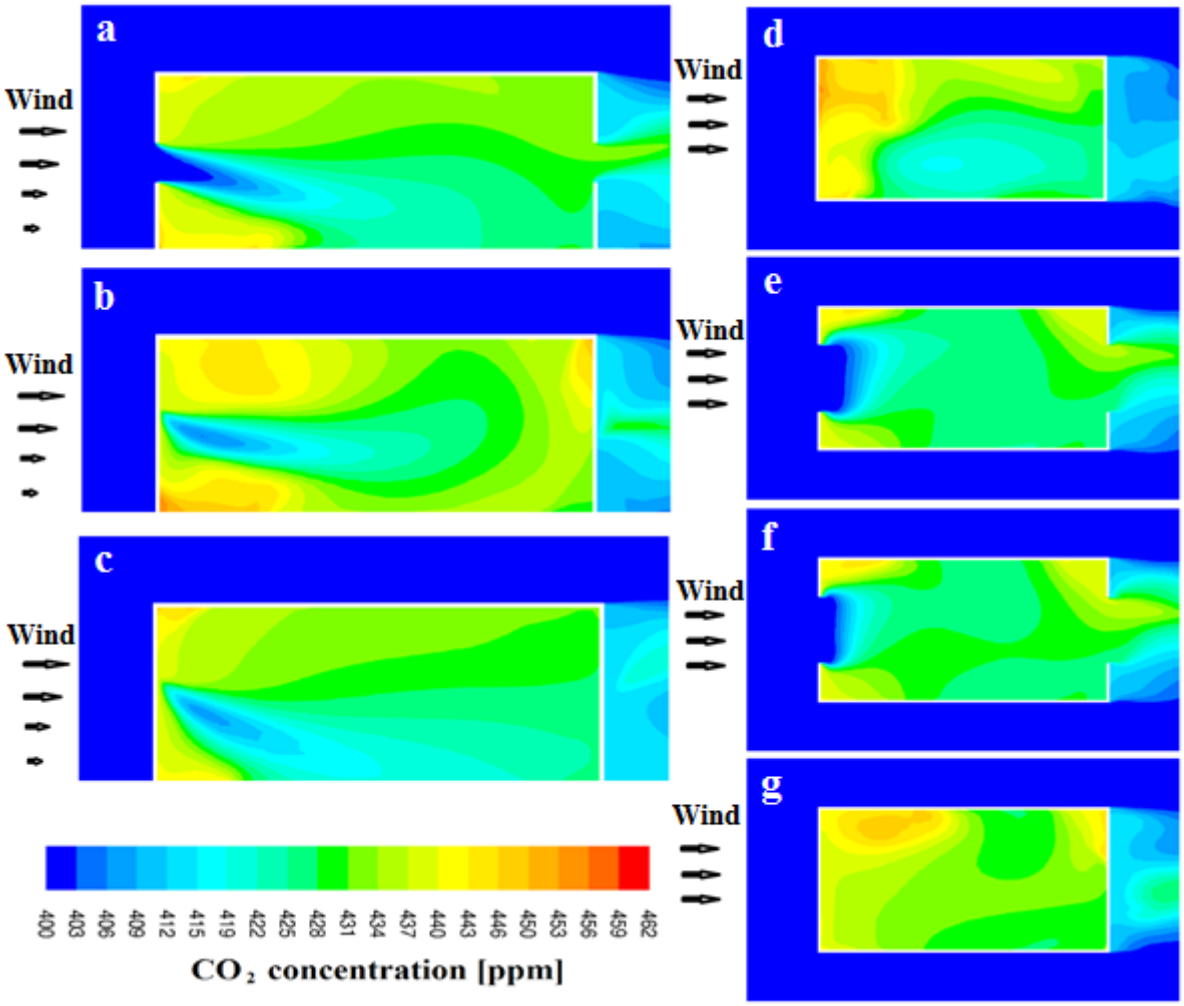

Figure 32 CO_2 concentration on the 2.5 H building depth: (a) Vertical center mid-plane; (b) Vertical left-plane (0.75 m to the left of the mid-plane); (c) Vertical right-plane (0.75 m to the right of the mid-plane); (d) Horizontal 0.1 m plane; (e) Horizontal 1.1 m plane; (f) Horizontal mid-plane (1.2 m); (g) Horizontal 1.7 m plane.

6.2.3. 5 times the building height

In Figure 33 the velocity vector field on the vertical mid-plane is shown. The main jet has a similar pattern when entering the room as the other two cases, being accelerated and directed downwards. Then, it starts to decelerate and flows near the ground surface in the direction of the outlet wall. When it is close to inlet wall the main jet is directed upwards in the direction of the opening, where it accelerates and leaves the room with an upward direction. In the inlet half of the building at mid-height a recirculation zone is depicted, with the upper part of the flow directed to the inlet wall. On the beginning of the outlet half at the top of the building, a region with really low velocities is seen and after this region, closer to the inlet wall, the flow starts to accelerate and is directed to the outlet wall joining the main jet. Slow moving zones are also found in the corners, except on the top of the inlet wall, where a recirculation zone is clearly depicted. As in the last two cases, the recirculation zones on the outside of the building below the main jet (either on the inlet wall or on the outlet wall) can be seen.

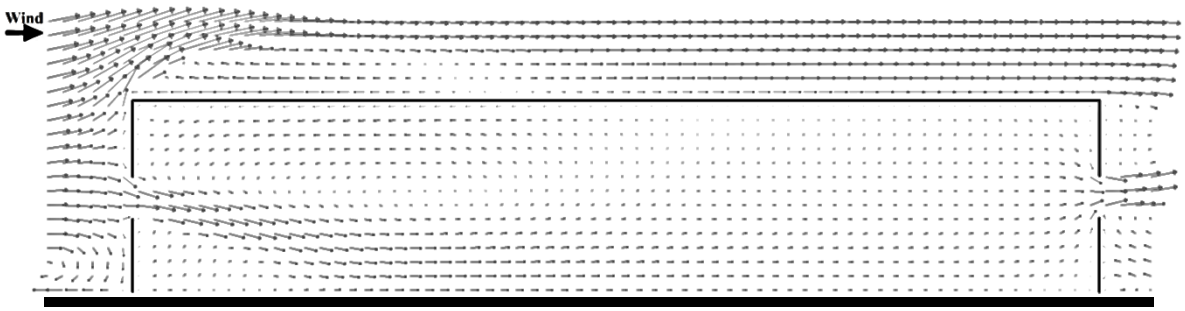

Figure 33 Velocity vector field on the vertical mid-plane of the 5 H building depth.

The velocity vector field on the horizontal mid-plane (*h* = 1.2 m) is represented in Figure 34. As in the previous case (Figure 31), the flow is asymmetric (possibly caused by the oscillatory behavior of the flow) and when it enters the building it accelerates and tends to the left. This jet, then, starts to decelerate and flows to the outlet wall traveling near the left side wall till the middle of the building. At this point, part of the flow tends to the center of the building while the flow closer to the wall continues to decelerate until it reaches really low velocities. On the center of the inlet half of the building (on the same place reported in Figure 33) a slow moving zone exists, probably due to the fact that it is situated at the center of the standing vortex previously reported. On this slow moving zone, it is possible to observe a small recirculation zone. The flow that enters from the right side of the opening is directed to the right side of the inlet wall with low velocities, traveling subsequently till the right side wall, starting then to flow to the outlet wall. The flow travels close to the wall and starts to accelerate until it is near the outlet wall. At this point, the flow is directed to the leeward opening leaving the room and joining the flow that comes from the center of the building. When it passes through the outlet opening the flow accelerates and leaves the building with higher velocities on the left side of the opening. A recirculation zone can also be seen on the left corner of the inlet wall.

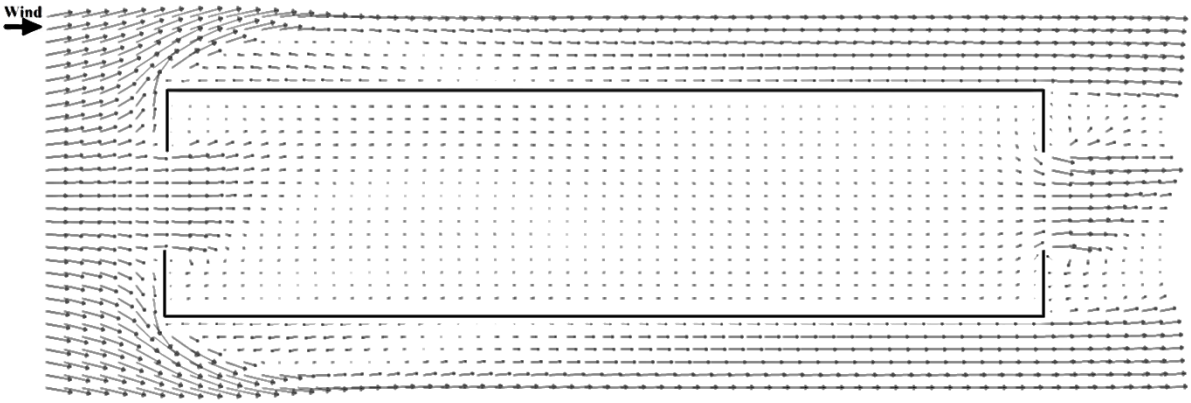

Figure 34 Velocity vector field on the horizontal mid-plane (h = 1.2 m) of the 5 H building depth.

A volume flow rate of 0.531 m^3 s^{-1} was obtained on the inlet opening of the building, corresponding to an air exchange rate of 24 ACH. The average mean age of air inside the room was 110.7 seconds and on the outlet opening an area-weighted average of 138.5 seconds was obtained, leading to an air exchange efficiency of 62.6%. The concentration of CO_2 on the building

had an average value of 450 ppm and a maximum value of 537 ppm. In Figure 35 the CO_2 concentration on different planes of the building is represented. The highest CO_2 concentration values are found on the left side of the outlet half of the building (Figure 35b,d-g), and the lowest values are found near the inlet wall, in the region affected by the main jet and on the right side of the building (Figure 35c) mainly near the ground surface. On the left side wall at 1.2 m height (Figure 35f) it is possible to see that the zone where the highest values are found is the same zone where really low velocities were seen in Figure 34. It is possible to see that the zones with the highest velocities are zones with the lowest concentrations in its surroundings (center of the left side wall, center of right side wall or ground surface a bit after the inlet opening).

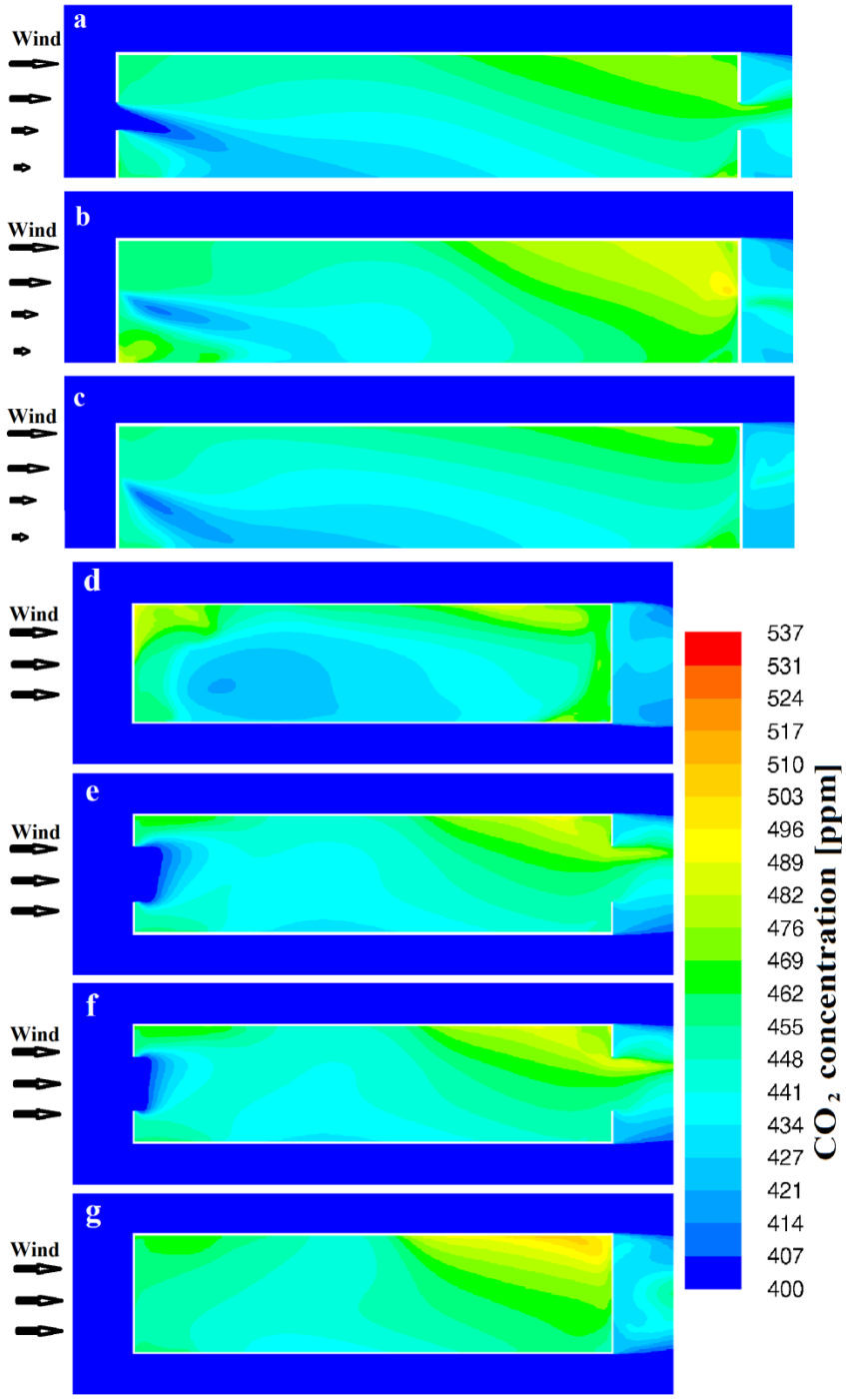

Figure 35 CO_2 concentration on the 5 H building depth: (a) Vertical center mid-plane; (b) Vertical left-plane (0.75 m to the left of the mid-plane); (c) Vertical right-plane (0.75 m to the right of the mid-plane); (d) Horizontal 0.1 m plane; (e) Horizontal 1.1 m plane; (f) Horizontal mid-plane (1.2 m); (g) Horizontal 1.7 m plane.

6.2.4. 10 times the building height

The velocity vector field on the vertical mid-plane is shown in Figure 36. As in the other cases, the main jet accelerates when it enters in the building and is directed downwards. Next, it decelerates and flows close to the ground surface. At 4.8 m (2 *H*) depth the jet starts to flow on the upwards

direction and at 9.6 m (4 *H*) all flow on this plane of the building starts to flow in the outlet direction. Lower velocities are registered on the top of the building till the 12 m (5 *H*) depth of the building. From this point and till near the outlet opening constant velocities are found, then the flow accelerates and is directed to the opening. This is not verified at the top and bottom of the building where lower velocities are found. After leaving the room the flow is directed upwards, as in the other cases. At mid height just after the inlet of the building a big recirculation zone is depicted. Above this area, near the top of the building the flow is directed to the inlet wall, being observed another recirculation on the corner of the building.

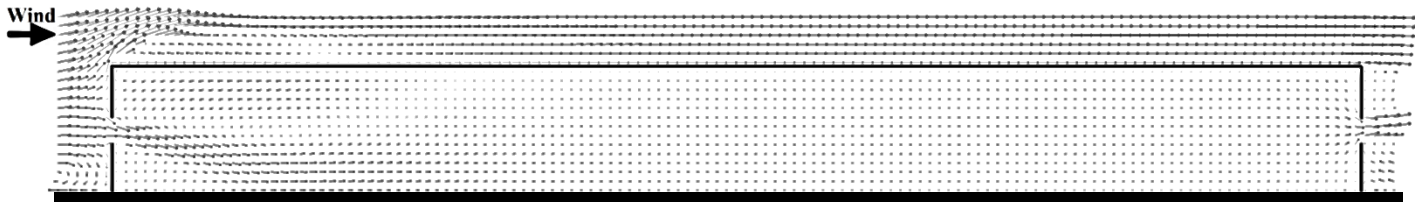

Figure 36 Velocity vector field on the vertical mid-plane of the 10 H building depth.

In Figure 37 the velocity vector field on the horizontal mid-plane (*h* = 1.2 m) can be seen. The flow is asymmetric (probably due to the oscillations existent in the flow, seen in the residuals), as in the last two cases. The flow is accelerated when enters the building and flows with higher velocities to the right side of the building while is in deceleration. This jet travels on the right side of the building close to the right side wall until 4.6 m (1.9 *H*) depth of the building, being then directed to the center from where it continues to decelerate to the outlet wall. Near to the right side wall, from the same depth and till 17.8 m (7.4 *H*) depth, a zone with low velocities can be seen, beginning then to accelerate to the outlet wall. The flow that enters from the left side of the inlet opening is directed with low velocities to the left side of the inlet wall. It is then directed to the left side wall and subsequently travels to the outlet wall, starting to accelerate at 1.7 meters (0.7 *H*) depth of the building. At the middle of the building this flow traveling near the left side wall starts to slowly decelerate. Near the outlet wall all the flow is directed to the outlet opening, accelerating when leaving the building, and being registered higher velocities on the right side of the building. As in the last case, a slow moving zone exists after the inlet opening on the same place of the recirculation zone existent on the vertical mid-plane (Figure 36).

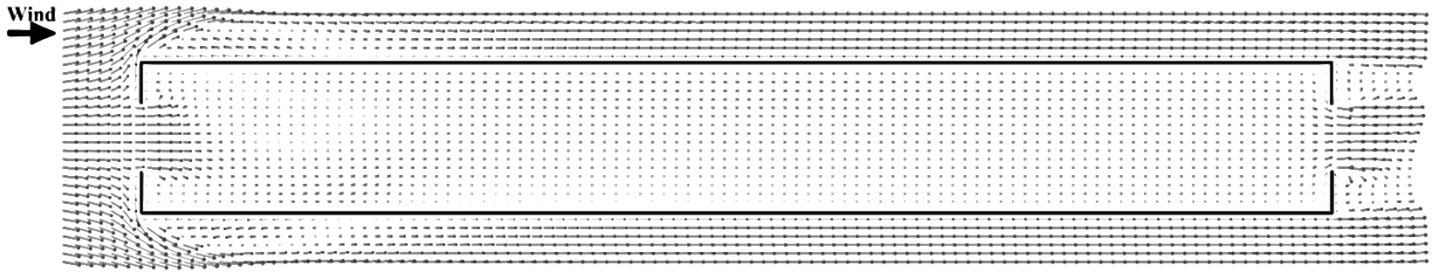

Figure 37 Velocity vector field on the horizontal mid-plane (h = 1.2 m) of the 10 H building depth.

On the inlet opening a volume flow rate of 0.531 m^3 s^{-1} was reported, leading to an air exchange rate of 12 ACH. The mean age of air inside the building was 174.9 seconds and the registered area-

weighted average of the outlet opening was 276.3 seconds. This results in an air exchange efficiency of 79%. The CO_2 concentration inside the room had an average value of 479 ppm, although values up to 678 ppm were registered inside the building. In Figure 38 the contours of CO_2 concentration on different planes of the building are represented. Contrasting with the last two cases, the highest values of CO_2 concentration are found on the right side of the building. This can be explained by the fact that the jet tends to the opposite side of the last two cases. For the same reason, the lowest values of CO_2 are found on the left side of the building near the ground surface (in opposite to the registered on the last two cases), as can be seen by the highest depth of penetration of the exterior CO_2 concentration seen in Figure 38b. As shown on the mid-plane of the building (Figure 38f) the outside air penetrates deeper into the left side of the building but, due to the existence of a zone with really low velocities on this side (Figure 37), higher concentration of CO_2 are also registered in the left side. The opposite occurs on the right side wall, where lower velocities are registered on the inlet of the building and higher velocities are registered a bit after the opening, resulting on lower concentration of CO_2 alongside this wall.

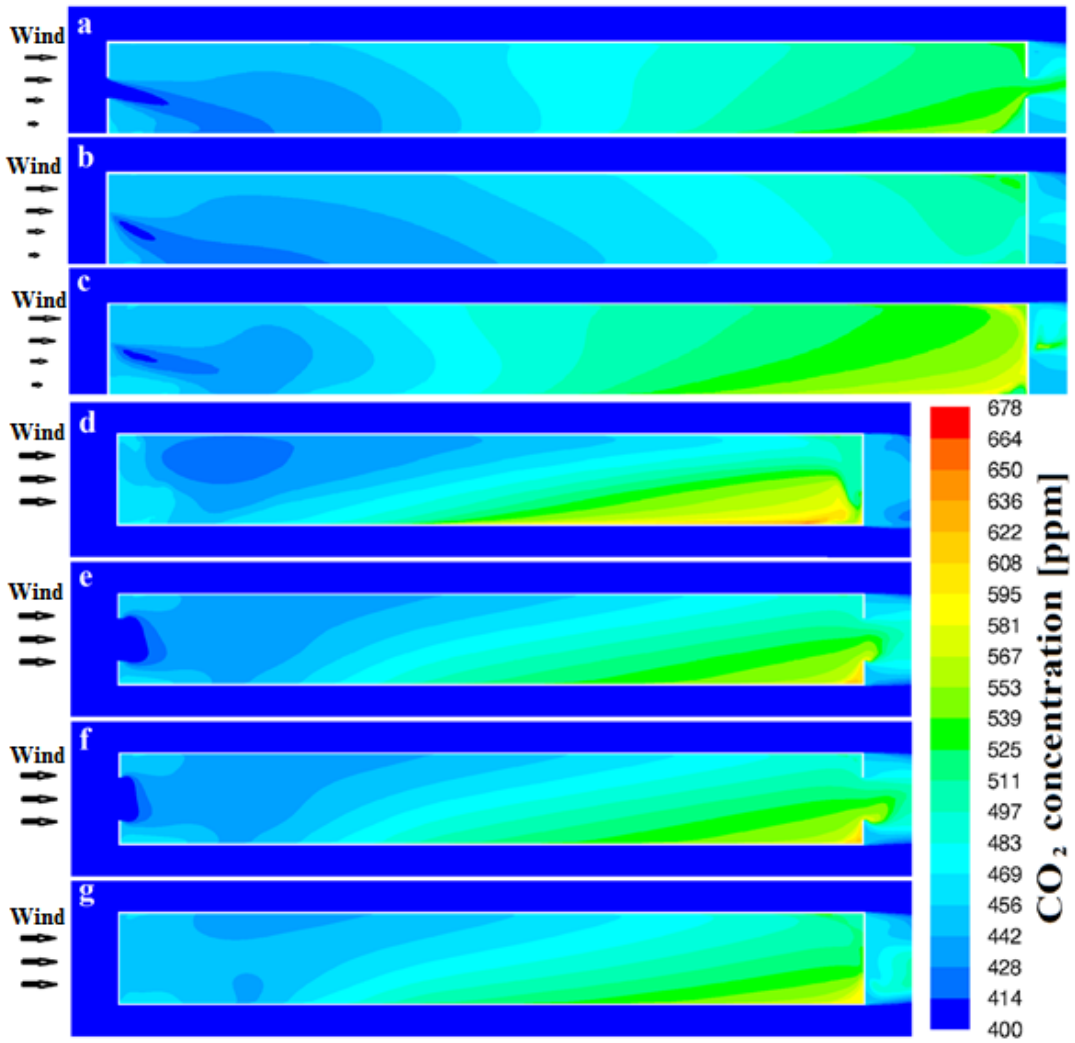

Figure 38 CO_2 concentration on the 10 H building depth: (a) Vertical center mid-plane; (b) Vertical left-plane (0.75 m to the left of the mid-plane); (c) Vertical right-plane (0.75 m to the right of the mid-plane); (d) Horizontal 0.1 m plane; (e) Horizontal 1.1 m plane; (f) Horizontal mid-plane (1.2 m); (g) Horizontal 1.7 m plane.

6.2.5. Discussion and conclusions

Four different building depths (doubling the building depth in relation to the previous building) were tested and different results were obtained. In Table 7 a summary of the different parameters assessed during the post processing of the CFD simulations is shown. It can be observed that the mean age of air increases with the depth of the building, although not with the same proportion as the building depth increase, with the exception of the first two building. The fact that the mean age of air increases in a minor proportion than the building depth, leads to higher air exchange efficiencies in the deepest buildings. From the air exchange efficiency results it can be seen that the flow evolves from a perfect mixed system type (50% efficiency) to an ideal piston type flow (100% efficiency), with the increasing depth of the building. This disproportion can also be seen on the average CO_2 concentration inside the building. On the other hand and due to the fact that the volume flow rate is relatively constant for the four cases, the air exchange rate decreases

proportionally with the increasing depth. The air exchange rate and the average CO_2 concentration are represented in Figure 39.

In the different figures shown for the four different building depths different flow patterns were observed. In the standard case the flow is symmetric on the horizontal mid-plane with two recirculation zones on both sides of the building, except when it leaves the room and is directed to the right side of the building. On the other three cases the flow on the horizontal mid-plane is asymmetric, which can be caused by the oscillatory behavior of the flow, as previous explained. For the 2.5 *H* and 5 *H* cases the flow enters and exists the building mainly by the left side, while on the 10 *H* building it occurs by the right side. The highest concentrations of CO_2 are found on the top left of the building near the inlet wall for the standard building case. On the 2.5 *H* building, in addition to the standard case zones, the highest CO_2 concentration values are found on the bottom left of the building. On the 5 *H* case the highest concentration values are found on the top left of the building near the outlet opening. On the 10 *H* building the highest values are found on the right side of the building near the outlet wall, mainly near the ground. In Figure 40 the local maximum and the average CO_2 concentration are shown for four different building depths. It is possible to see that the local maximum value of CO_2 concentration increases with a substantial higher rate compared to the average concentration.

Accordingly to the results previously shown it is possible to observe that the natural ventilation is still effective after the limit of 5 *H* assumed by Awbi (2003), as can be observed by the values obtained for the different cases of mean age of air, air exchange efficiency and CO_2 concentration for this particular case. Although, the volume flow rate does not suffer any significant variation between the different depths and as a consequence the air exchange rate diminishes with the increasing depth of the building. For this reason, the building depth at some point will lead to low air exchange rates, which has an impact on the air quality inside the building. This effect will be more notorious if lower velocities exist (after the inlet opening velocities of 1 m s^{-1} are still registered) which leads to lower volume flow rates on the building. To reduce the velocities inside the building it could be interesting to test different wall porosities. Although, special attention should be taken due to the fact that smaller and larger openings, compared to the one used in this thesis, could lead to an increase of the velocities registered inside the building, as was reported by Karava (2008) and Karava et al. (2011).

Table 7 Mean age of air, air exchange efficiency, CO_2 concentration, volume flow rate and air exchange rate for the four building depths.

	Mean age of air [s]	Air exchange efficiency [%]	CO_2 [ppm]	Volume flow rate [$m^3 s^{-1}$]	Air exchange rate [ACH]
Standard	34.4	50%	415	0.539	100
2.5 H	68.1	51%	431	0.528	48
5 H	110.7	63%	450	0.531	24
10 H	174.9	79%	479	0.531	12

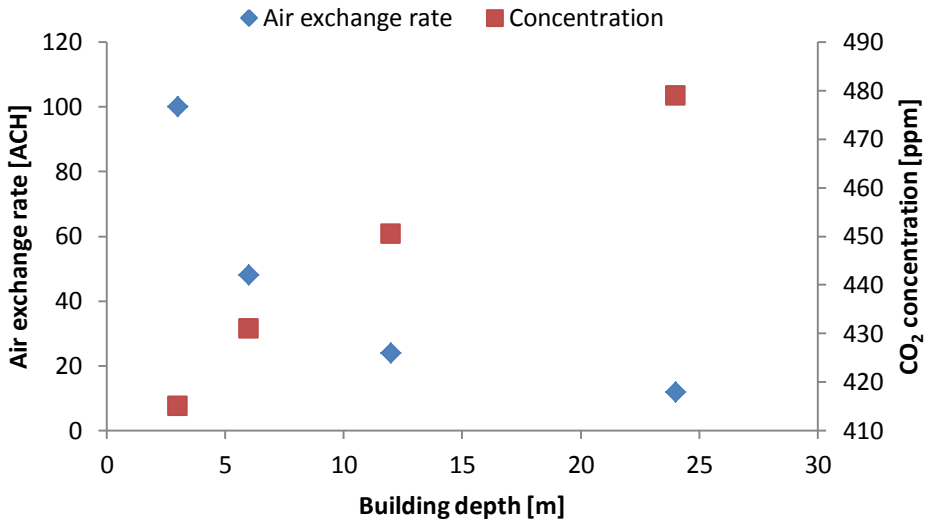

Figure 39 Air exchange rate and average CO_2 concentration for the four different depths.

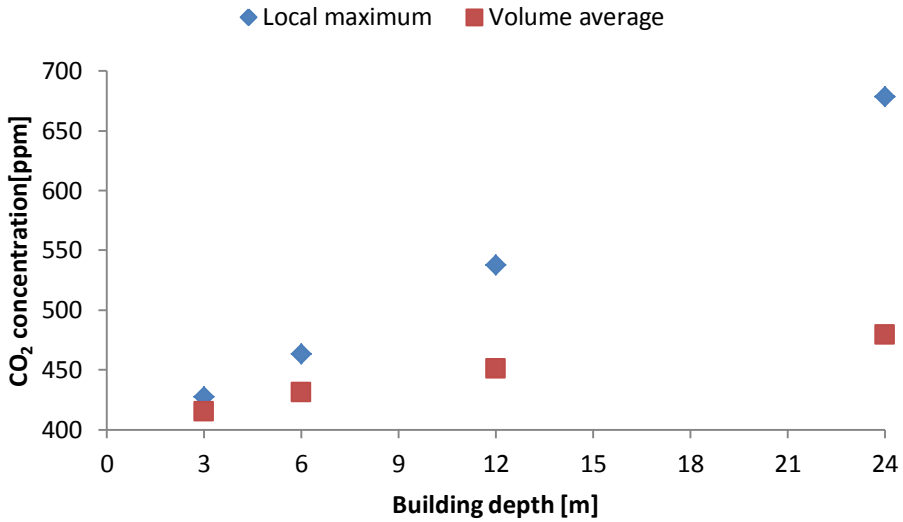

Figure 40 Local maximum and volume average CO_2 concentration for the four different depths.

6.3. Partitioned building

In order to understand the impact of different building configurations, four different building geometries were constructed and simulated for two different building depths. The first case is the standard building with no partition in its interior and the other three cases had a partition located at different positions: one with a partition with a door situated in the center of the building; other with the door just after the inlet opening (between the first and second quartiles); and the last case with the door on the left side of the building (with its center between the first and second quartile starting on the left side wall). The different geometries can be seen in Figure 41. These four different configurations were simulated for the standard building depth and for the 2.5 *H*

building depth, although the results for the buildings without partition were already presented. On the post processing of the simulations the same parameters as used in chapter 6.2 were collected and used for the comparison of the different cases.

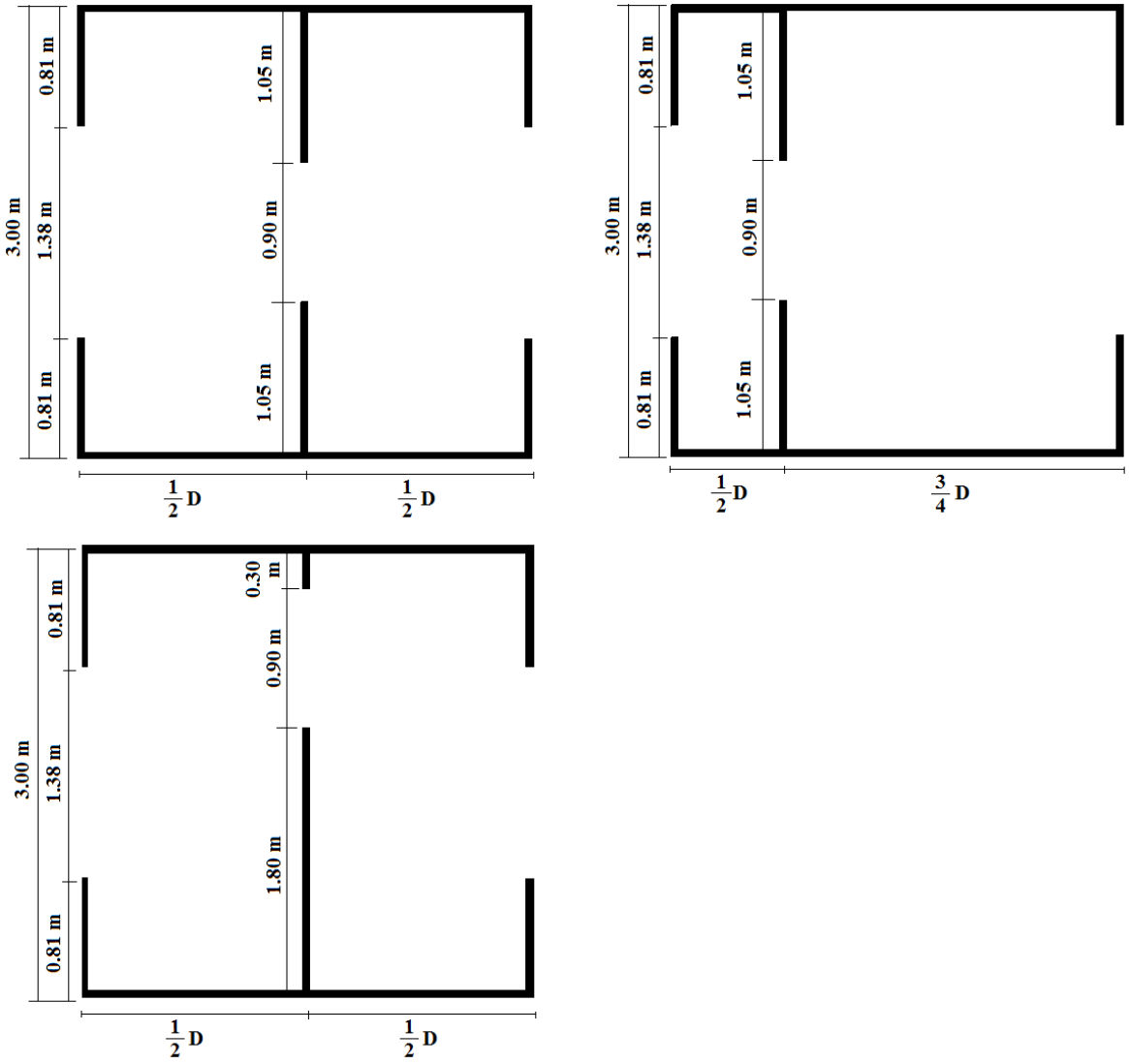

Figure 41 Blueprint at mid-height for the three different configurations.

6.3.1. Standard depth

The results of the standard building depth can be seen in chapter 6.2.1.

6.3.1.1. Door opening in the center of the building

In Figure 42 the velocity vector field on the vertical mid-plane is shown. It is possible to observe that the flow enters in the room, accelerates and is directed downwards, as in the standard building case. Although, unlike the standard case, when the main flow reaches the door zone it is again accelerated and looses part of its downwards direction being then directed to the leeward opening. A recirculation zone is depicted over the main jet before the door oppening, and a smaller one is also visible on the top of the first room (over the first one). Near the ground level a

recirculation zone is visible on the second room, which is formed by the flow that is directed downwards on the outlet wall. On the upper part of the outlet room all the air flows in the direction of the outlet wall, being directed then to the outlet opening, where it joins the main jet and leaves the room directed upwards.

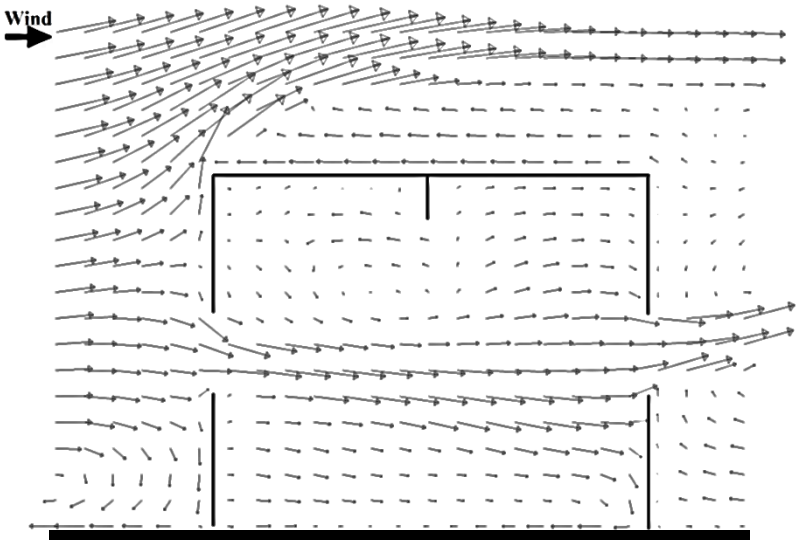

Figure 42 Velocity vector field on the vertical mid-plane of the standard building depth with a door in the center of the building.

In Figure 43 the velocity vector field on the horizontal mid-plane can be seen. It is clearly visible that the flow is symmetric considering the center of the building openings. The flow that enters the room is accelerated and directed to the outlet opening. Although, only part of it passes throught the door and travels to the outlet room. The rest of the flow is directed to the wall that separates the two rooms and its directed to the sides where two recirculation zones are formed (one on the left side, one on the right side). In both sides of the second room is possible to observe that the flow comes from the outlet wall near the outlet opening, circulates around the surrounding walls and then joins the main flow that leaves the room symmetrically.

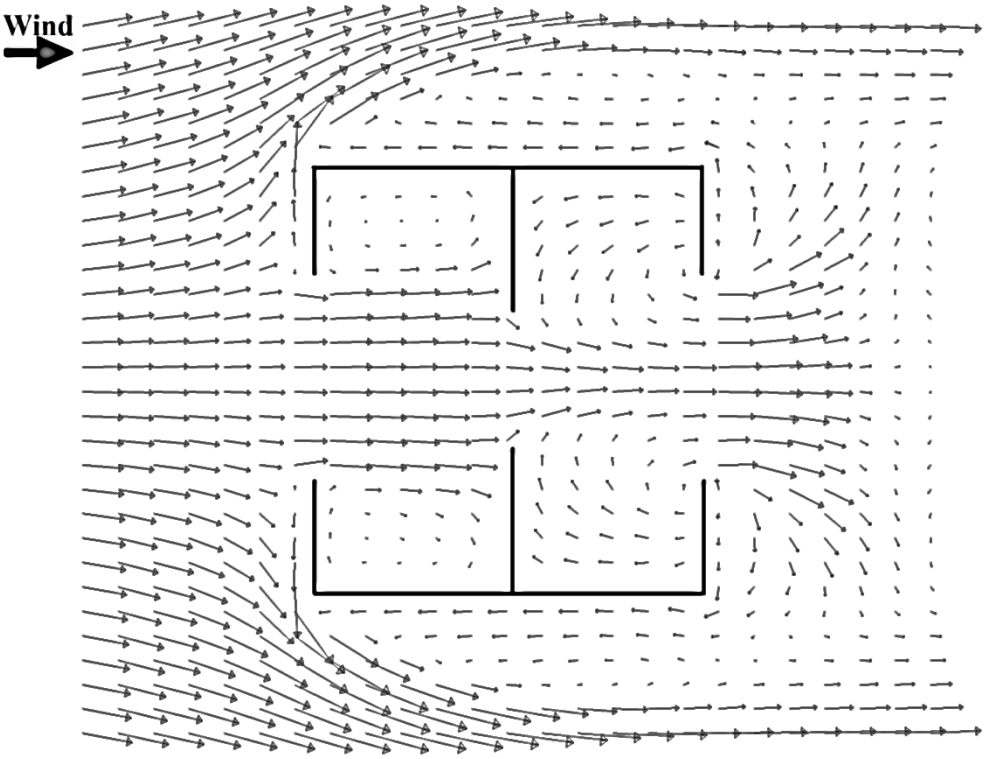

Figure 43 Velocity vector field on the horizontal mid-plane (h = 1.2 m) of the standard building depth with a door in the center of the building.

The volume flow rate registered on the inlet opening was 0.560 m^3 s^{-1} corresponding to an air exchange rate of 105 ACH, which is higher than in the standard case. The average mean age of air inside the inlet room was 35.4 s, in the outlet room 38.0 s and the average of the building was 36.7 seconds. The area-weighted average of the mean age of air on the outlet opening was equal to 33.2 seconds, resulting in an air exchange efficiency of 45.3%. The CO_2 concentration was almost equal on both rooms, being registered 416 ppm in the inlet room, 417 ppm in the outlet room and an average of 416 ppm in the entire building. The maximum concentration registered inside the room was 426 ppm. In Figure 44 and Figure 45 it is possible to observe the CO_2 concentration in different planes of the building. The lowest values of CO_2 are found on the central plane (Figure 44a) where the highest velocities were registered. In this plane, the highest values are found on the inlet room over the main jet and close to the top, where a recirculation zone was clearly visible. The symmetry previously reported is noticeable (Figure 44b-c and Figure 45a-d). The highest concentrations values are mostly found in the outlet room on the sides of the outdoor opening. Although in the inlet room high values are also found near the top of room, as previously reported.

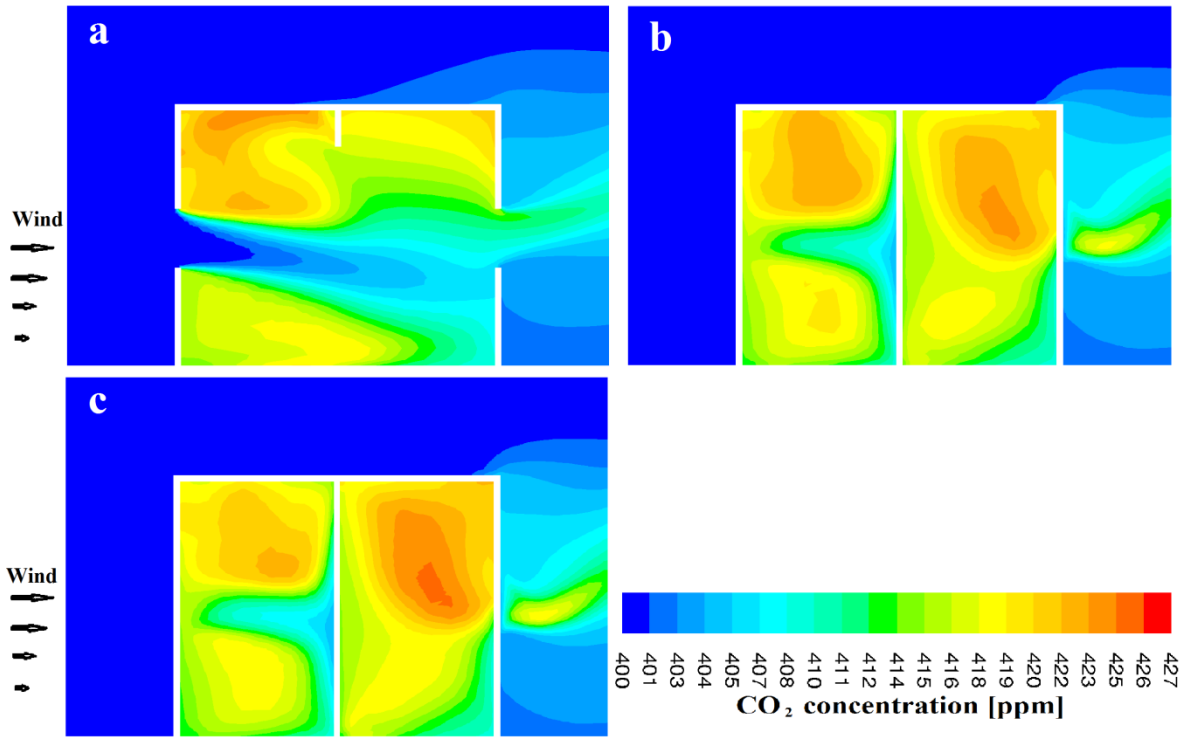

Figure 44 CO_2 concentration on the standard building depth with a door in the center of the building: (a) Vertical center mid-plane; (b) Vertical left-plane (0.75 m to the left of the mid-plane); (c) Vertical right-plane (0.75 m to the right of the mid-plane).

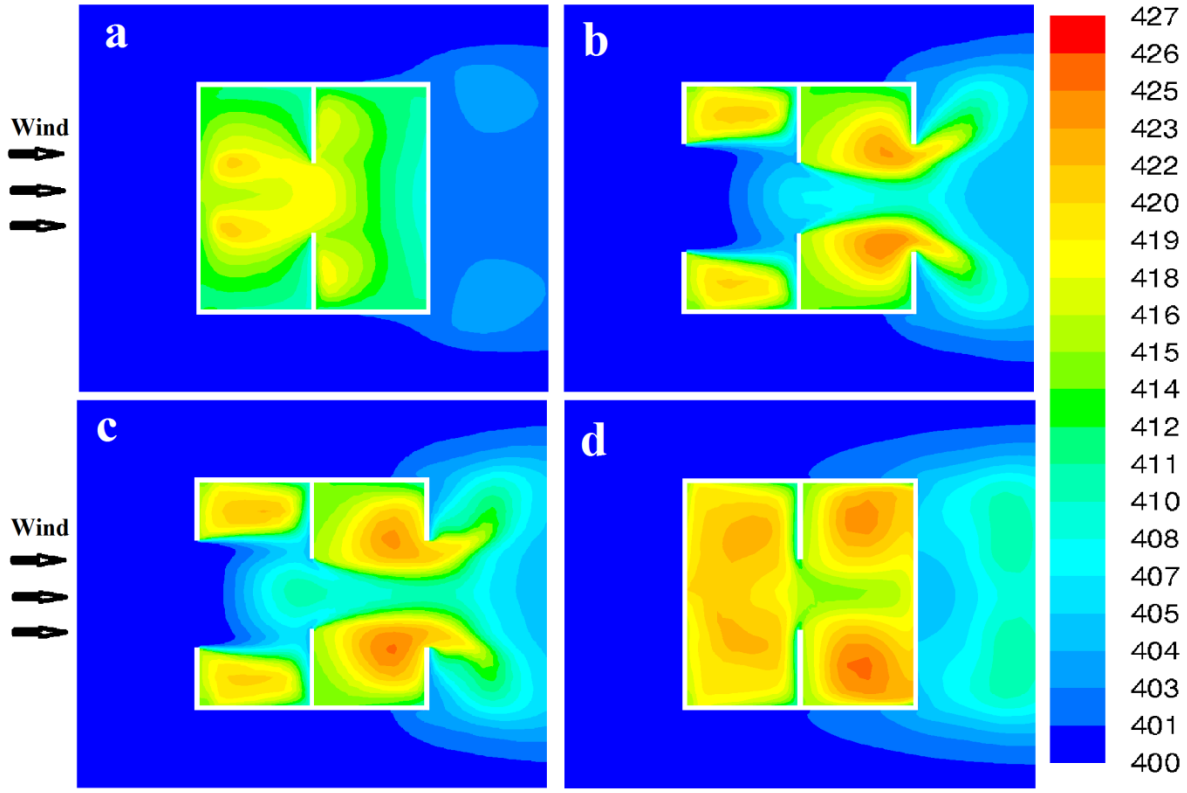

Figure 45 CO_2 concentration on the standard building depth with a door in the center of the building: (a) Horizontal 0.1 m plane; (b) Horizontal 1.1 m plane; (c) Horizontal mid-plane (1.2 m); (d) Horizontal 1.7 m plane.

6.3.1.2. Door opening near the inlet opening

The velocity vector field on the vertical mid-plane is shown in Figure 46. It can be seen that the air enters the room and suffers acceleration with a downward direction. It then passes through the door opening (which is just 0.75 m after the inlet wall) accelerating once again and being directed to the outlet wall. Most of this jet passes then to the outside through the leeward opening. However, the rest of this jet travels to the lower part of the outlet wall being then directed to the ground, where a recirculation zone is formed. Another recirculation zone is visible on the top of the first room, formed by the air that enters in this room coming from the second room. The rest of the air that enters from the second room to the first room is directed downwards joining the main jet. On the top of the outlet room a zone with low velocities is found on the top just after the door opening. From this zone, the flow suffers accelerations and is directed to the first room and in the direction of the outlet wall. When it gets close to the outlet wall it is directed downwards joining the main jet and leaving the room.

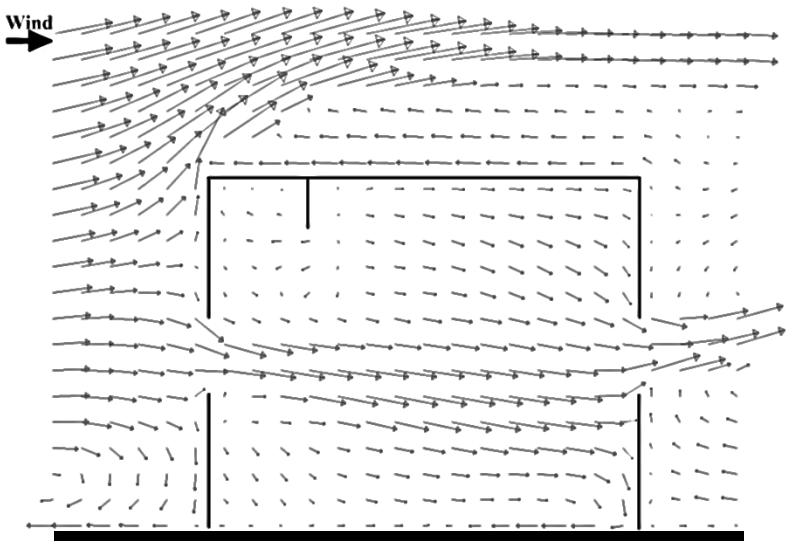

Figure 46 Velocity vector field on the vertical mid-plane of the standard building depth with a door near the inlet of the building.

In Figure 47 the velocity vector field on the horizontal mid-plane of the building is shown. As in the last case, it is visible that the flow is symmetric on both sides of the room. The main jet enters the room being accelerated and then part of it passes through the opening and the other stays in the inlet room. The flow that passes is accelerated again and continues to the leeward opening leaving the room. The part that does not pass through the door opening is directed to both sides of the inlet room, where recirculation zones are formed (one in each side). On the outlet room, two other recirculation zones are clearly depicted on both sides of the building. These are formed by the air that does not leave the room and is directed to the sides of the outdoor opening.

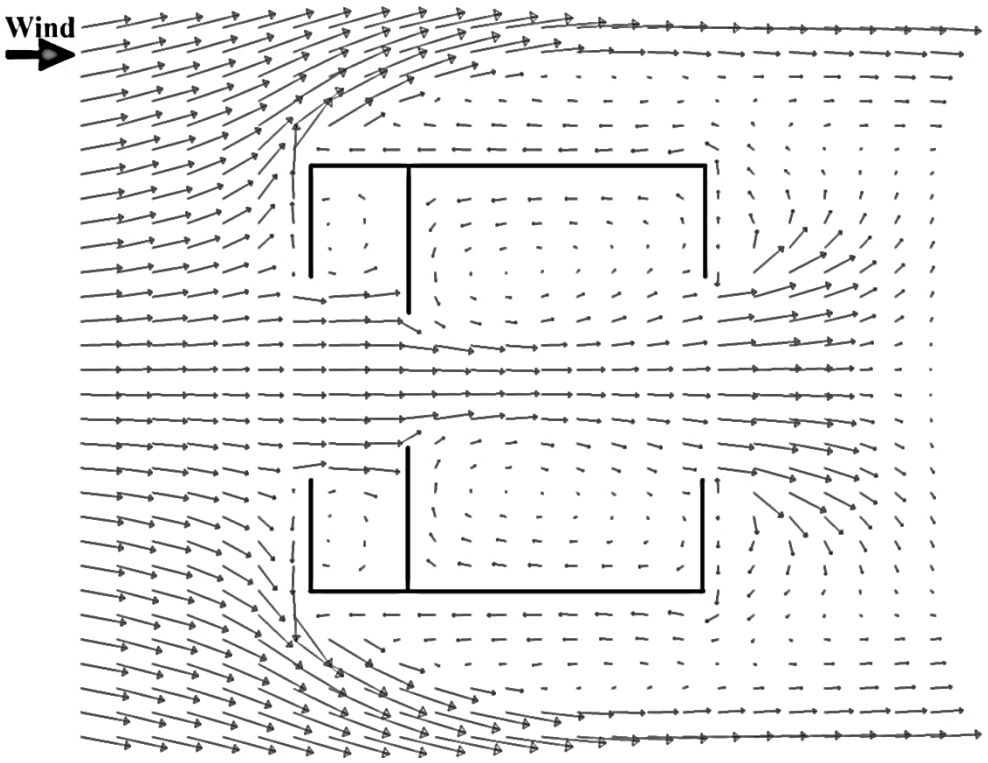

Figure 47 Velocity vector field on the horizontal mid-plane (h = 1.2 m) of the standard building depth with a door near the inlet of the building.

The volume flow rate registered passing through the inlet window was 0.557 m^3 s^{-1} leading to an air exchange rate of 105 ACH, which is similar to the case with the door in the center of building. The average mean age of air registered in the inlet room was 24.2 s, in the outlet room 32.5 s and a total of 30.5 s was registered on the whole building. On the outlet opening, the area-weighted average of the mean age of air was 33.5 s, therefore the air exchange efficiency of the building was 55.0%. The CO_2 concentration registered in the inlet room was 411 ppm, in the outlet room 415 ppm and an average of 414 ppm was registered for the entire building. The maximum value registered inside the room was 425 ppm. The CO_2 concentration on different planes of the building can be seen in Figure 48 and Figure 49. As in the previous case, the lowest values of CO_2 can be found on the central plane of the building where higher velocities are registered (Figure 48a and Figure 49b,c). The highest values are found on the top of the second room near the outlet wall (Figure 48b,c Figure 49d) being registered slightly higher values on the left side of the building. The symmetry existent in the mid-plane of the horizontal velocity vector field is also clearly visible in Figure 48 and Figure 49.

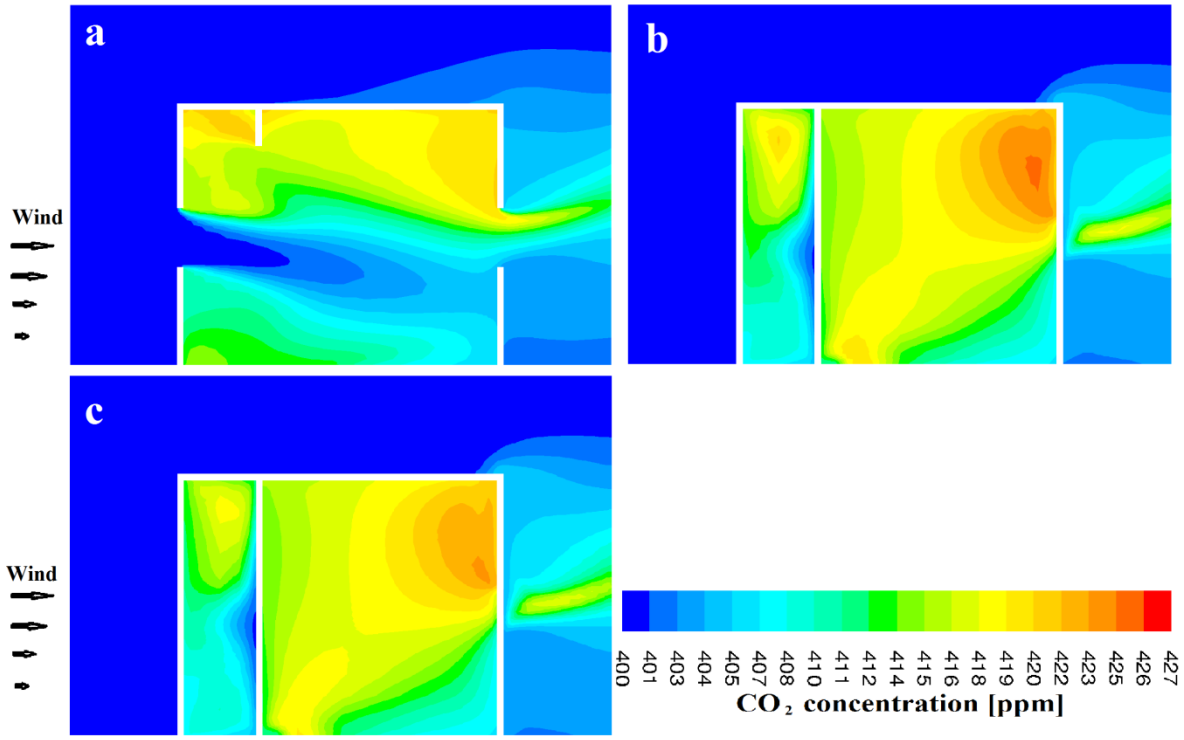

Figure 48 CO_2 concentration on the standard building depth with a door near the inlet of the building: (a) Vertical center mid-plane; (b) Vertical left-plane (0.75 m to the left of the mid-plane); (c) Vertical right-plane (0.75 m to the right of the mid-plane).

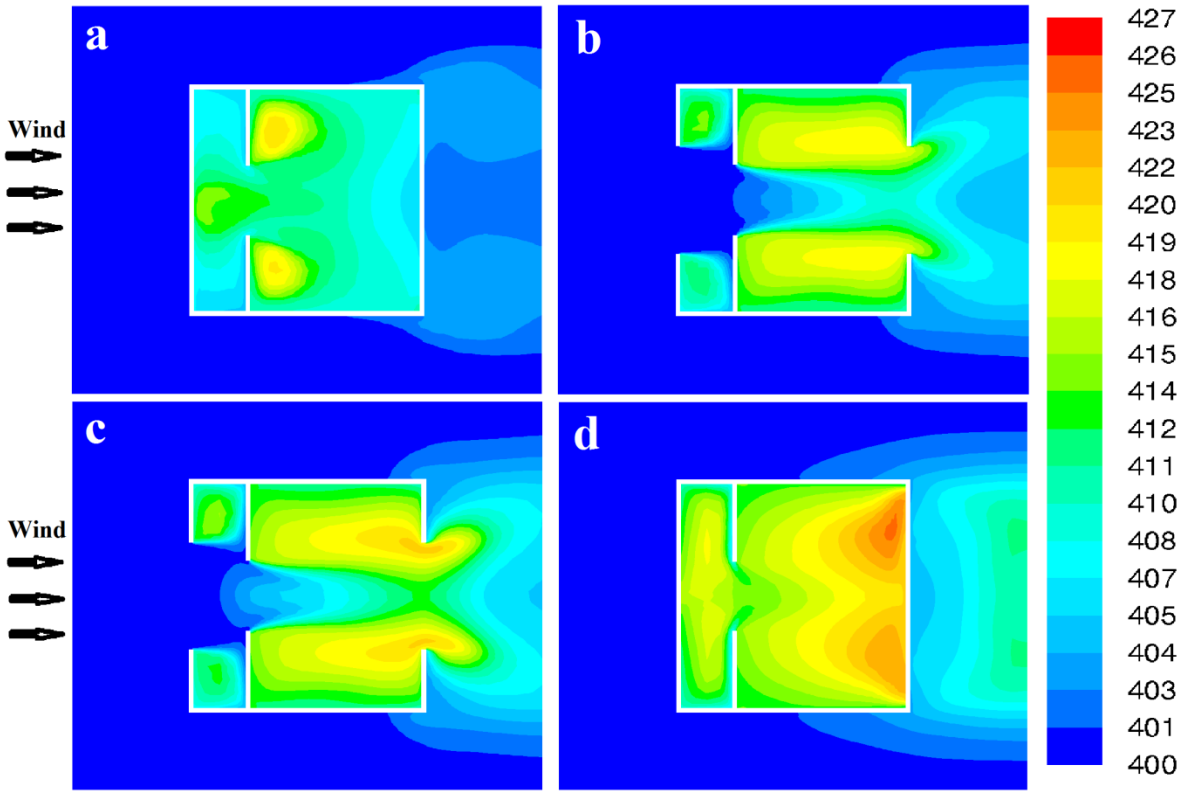

Figure 49 CO_2 concentration on the standard building depth with a door near the inlet of the building: (a) Horizontal 0.1 m plane; (b) Horizontal 1.1 m plane; (c) Horizontal mid-plane (1.2 m); (d) Horizontal 1.7 m plane.

6.3.1.3. Door opening near the left side wall

In Figure 50 the velocity vector field on the vertical mid-plane of the building is shown. This plane does not intercept the door opening which is situated near the left side wall (center of the door opening is 0.75 m apart from the left side wall). It is possible to observe that the flow enters in the inlet opening and is slightly directed downwards until it reaches the partition wall. At this point, part of the flow is directed upwards and the other part is directed downwards, forming two different recirculation zones with its centers close to the top and bottom surfaces. In the outlet room, a zone with low velocities is depicted at the height of the top of the opening and where a small recirculation zone can be seen. Near the leeward wall is possible to observe that the air is directed to the top of the building and to the outlet opening. The one which is directed to the top is either directed to the separation wall where it accelerates and is directed downward, or is directed to the outlet wall being then directed to the outside of the room. The flux that is directed downward then joins the flow that is directed to the leeward opening (just below the recirculation zone). Near the ground is possible to see that low velocities are found close to the separation wall and that from this point the flow accelerates in the direction of the outlet wall and finally is directed to the outside of the room. The flow leaves the room with an upward direction, as in the other cases.

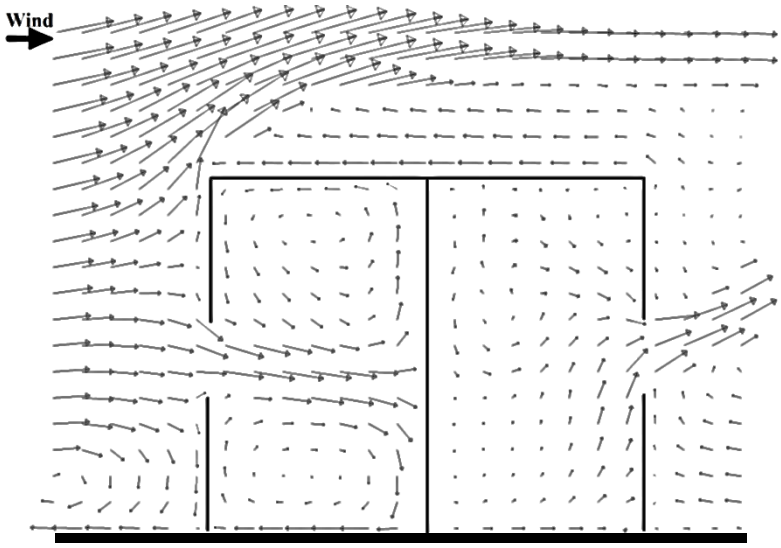

Figure 50 Velocity vector field on the vertical mid-plane of the standard building depth with a door near the left side wall.

The velocity vector field on the horizontal mid-plane of the building is shown in Figure 51. It can be seen that the flow accelerates when it enters the building. The flow then collides against the wall being partly directed to the left side of the building and partly directed to the right side. On the right side of the inlet room, a recirculation zone is formed. On the left side the jet flushes to the door opening entering in the outlet room. In this room, part of the flow is immediately directed to the outdoor opening leaving the room and other part forms a recirculation zone in the center of the room just on the left side of the door opening. On the right side of the outlet room a small recirculation zone can be seen close to the outlet wall. Just before this zone is possible to observe a zone where the flow is accelerated and is directed to the center of the building. The flow is then directed to the partition wall where it continues to accelerate and starts to be directed to the outlet opening where it finally leaves the room. When leaving the room the flow flushes with higher velocities to the right side of the building. The flow that leaves the room by the left side is directed to the outlet wall, and a recirculation zone is visible on the left side just after the opening.

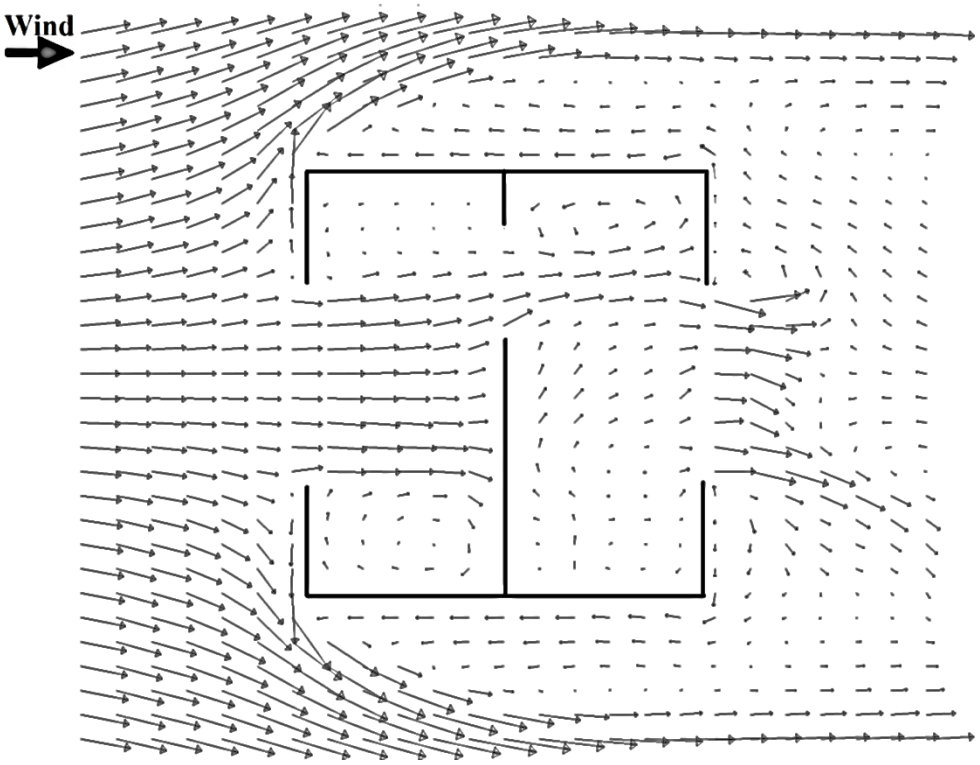

Figure 51 Velocity vector field on the horizontal mid-plane (h = 1.2 m) of the standard building depth with a door near the inlet of the building.

On the inlet opening a volume flow rate of 0.514 m^3 s^{-1} was registered resulting in a total air exchange rate of 97 ACH. The average mean age of air in the inlet room was 23.3 s, in the outlet room 36.3 s and averaging a total of 35.9 second in the entire building. In the outlet opening a total area-weighted average of 35.9 seconds was recorded, leading to an air exchange efficiency of 60.3%. Regarding the CO_2 concentration the maximum value registered inside the building was 427 ppm. An average of 411 ppm was registered on the inlet room, 416 ppm on the outlet room and an average of 413 ppm was registered for the entire building. In Figure 52 and Figure 53 the CO_2 concentration in the different planes of the building is shown. It is possible to observe that the highest concentration values can be found on the right side of the building (Figure 52c) either on the bottom (Figure 53a) or on the top (Figure 53d). The lowest concentration values can be found on the inlet room just after the opening at mid-height of the building. It is interesting to observe that the flow entering by the right side of the inlet opening as a highest depth of penetration compared to the one entering by the left side (Figure 53b,c). It is also interesting to notice that low CO_2 concentration values are found on the inlet room, meaning that the flow entering in the division is being well mixed with the air already on it.

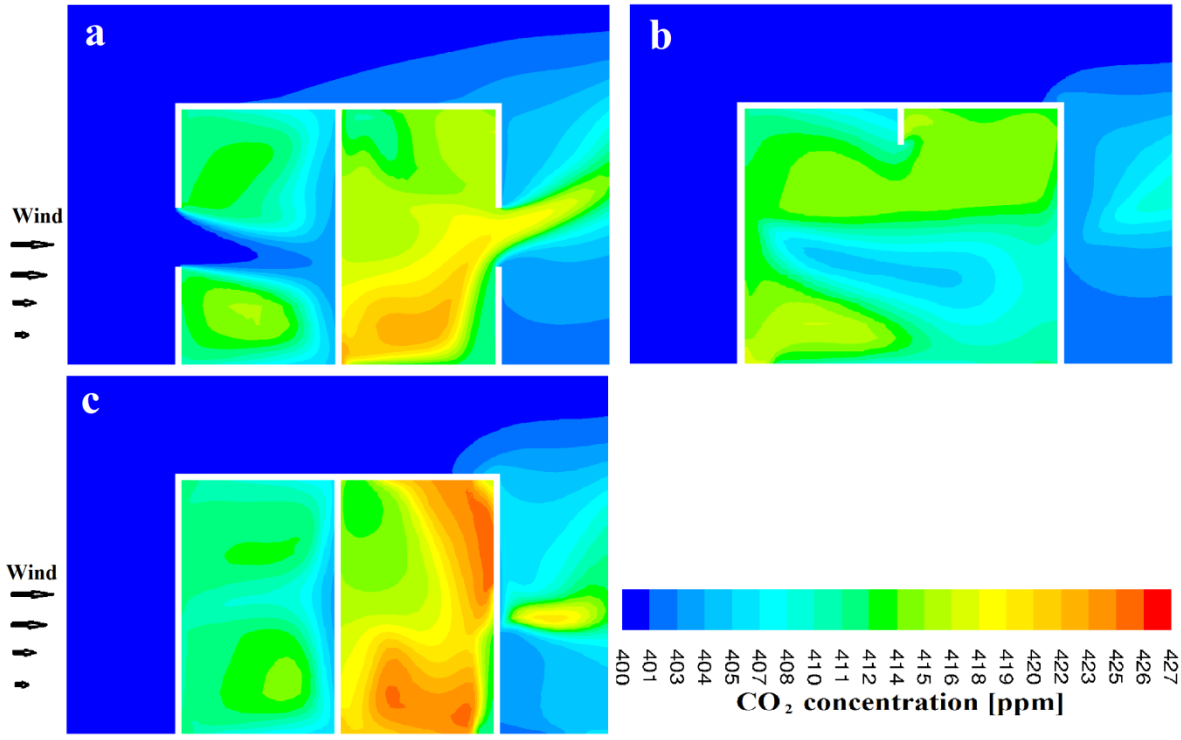

Figure 52 CO_2 concentration on the standard building depth with a door near the left side wall: (a) Vertical center mid-plane; (b) Vertical left-plane (0.75 m to the left of the mid-plane); (c) Vertical right-plane (0.75 m to the right of the mid-plane).

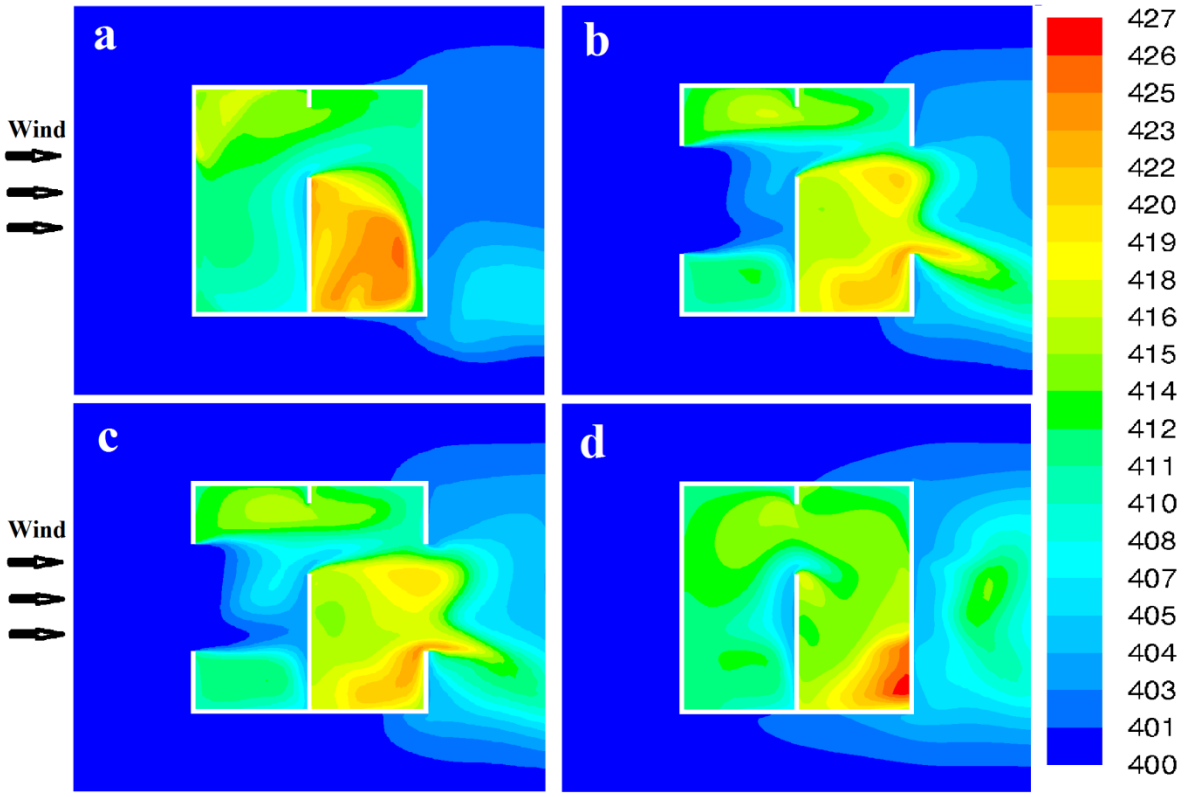

Figure 53 CO_2 concentration on the standard building depth with a door near the left side wall: (a) Horizontal 0.1 m plane; (b) Horizontal 1.1 m plane; (c) Horizontal mid-plane (1.2 m); (d) Horizontal 1.7 m plane.

6.3.2. 2.5 times the building height

The results of the 2.5 H building depth can be seen in chapter 6.2.2.

6.3.2.1. Door opening in the center of the building

In Figure 54 the velocity vector field on the vertical mid-plane is shown. It can be seen that the air enters in the room and accelerates with a downwards direction as in the building without partition. Although, when the main jet gets closer to the door it decelerates and starts to flow in the outlet direction parallel to the ground. When it enters in the second room it is directed to the outlet window, leaving the outlet opening with an upward direction. In the inlet room is also possible to observe a small recirculation zone near the ground and close to the door opening and a bigger one above the main jet. On the outside of this recirculation zone is possible to observe that part of the flow flushes to the inlet wall going down and subsequently joining the main jet. The other part flushes to the upper part of the door opening entering in the second room directing upwards. In the second room this jet is directed to the top of the building till the middle of the room, starting then to be directed to the outlet opening where it leaves the room.

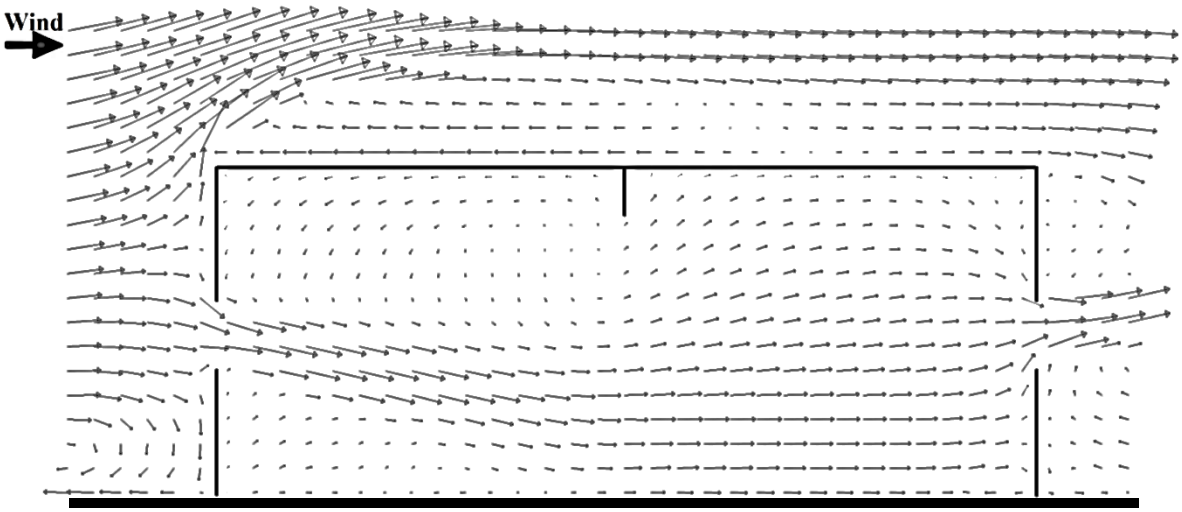

Figure 54 Velocity vector field on the vertical mid-plane of the 2.5 H building depth with a door in the center of the building.

The velocity vector field on the horizontal mid-plane can be seen in Figure 55. It can be seen that the flow is asymmetric (maybe due to the oscillatory behavior of the flow) like in the case without any partitions and unlike the similar case with the standard building depth. The flow accelerates when enters the room and is directed predominantly to the right side of the building till it reaches the partition. At this point the flow is directed to the door opening entering in the second room. After it enters in the second room, it flushes straight to the outlet opening where it leaves the room, tending to the right side of the building. In the inlet room the flow that is directed to the right side and does not leave the room, travels to the partition wall and then is directed to the inlet wall, forming a recirculation zone. On the right side the flow has low velocities, being observed a small recirculation zone just after the inlet opening and another one close to the partition wall.

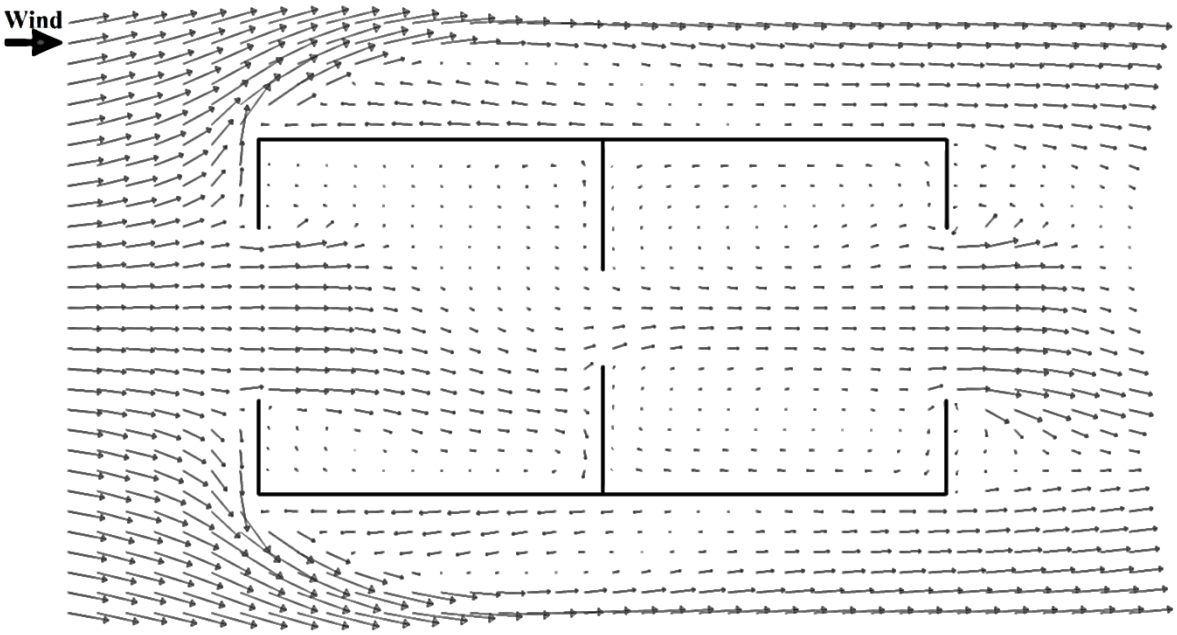

Figure 55 Velocity vector field on the horizontal mid-plane (h = 1.2 m) of the 2.5 H building depth with a door in the center of the building.

The volume flow rate registered on the inlet opening was 0.523 m^3 s^{-1}, corresponding to an air exchange rate of 48 ACH, which is equal to the values registered in the case without any partition. The average mean age of air registered was 47.7 s, 81.1 s and 64.4 s in the inlet room, outlet room and entire building, respectively. The area-weighted average of the outlet opening was 70.4 s, which leads to an air exchange efficiency of 54.7%. The maximum concentration of CO_2 registered in the building was 458 ppm. The average recorded in the inlet room was 422 ppm, in the outlet room 437 ppm and the average of the building 429 ppm. In Figure 56 the CO_2 concentration in different planes of the building is shown. It is possible to observe that the highest concentration values are found on the left side of the second room near the ground plane (Figure 56d). On the other hand the lowest values are right after the inlet opening at mid-height (Figure 56e,f). It is interesting to observe that the right side has lower concentration values, except on the top of the inlet room (Figure 56g). It is visible that lower concentrations of CO_2 are found on the center of the lower planes, which is due to the effect of the downward direction of the jet that enters in the building.

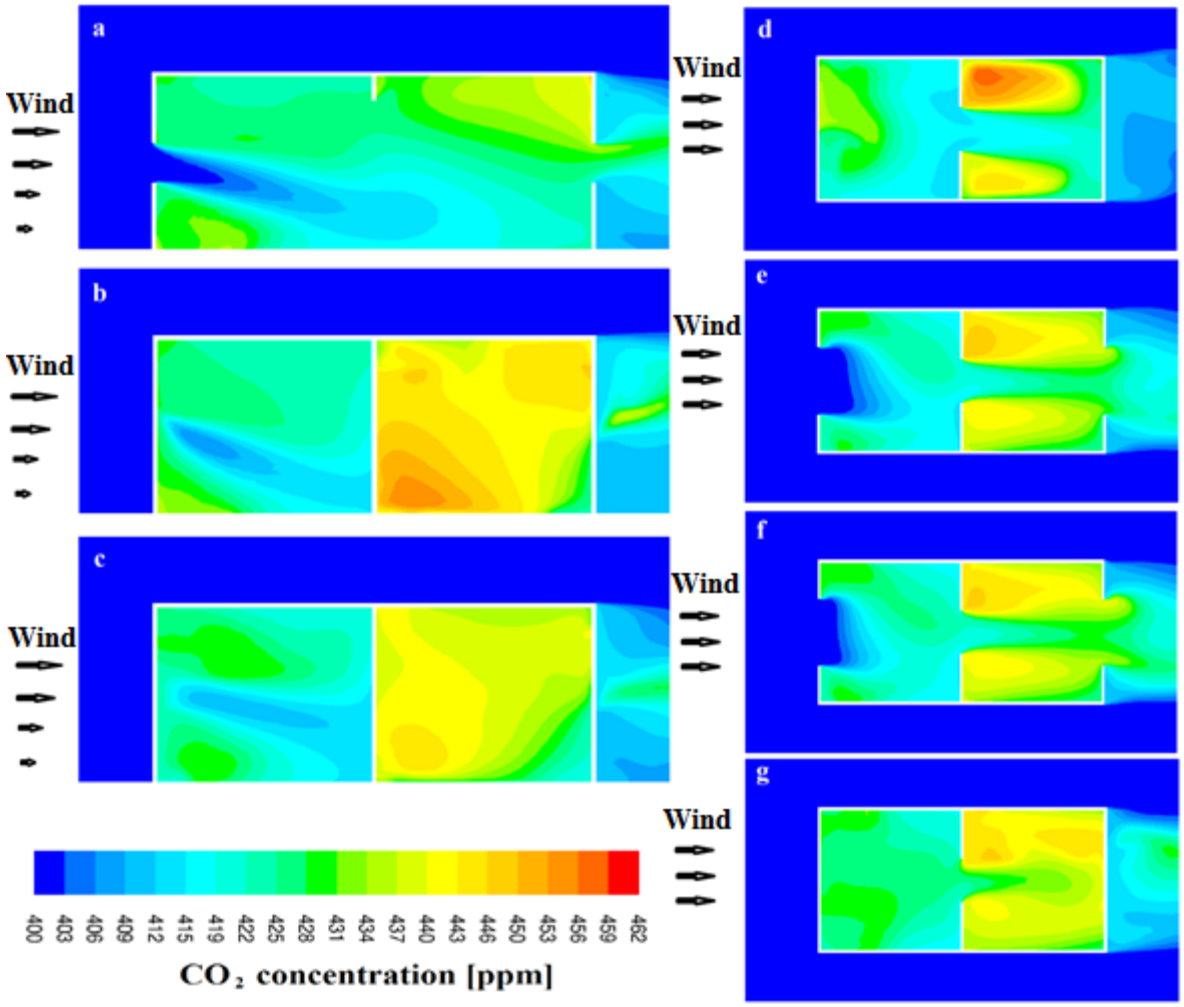

Figure 56 CO_2 concentration on the 2.5 H building depth with a door in the center of the building: (a) Vertical center mid-plane; (b) Vertical left-plane (0.75 m to the left of the mid-plane); (c) Vertical right-plane (0.75 m to the right of the mid-plane); (d) Horizontal 0.1 m plane; (e) Horizontal 1.1 m plane; (f) Horizontal mid-plane (1.2 m); (g) Horizontal 1.7 m plane.

6.3.2.2. Door opening near the inlet opening

The velocity vector field on the vertical mid-plane is shown in Figure 57. The flow enters in the room with a downward direction accelerating till it is close to the door opening (located 1.5 m after the inlet opening). After the opening, this main jet suffers again acceleration and continues to flow with a downward direction till it gets near the outlet wall. At this point, the jet is directed to the leeward opening where it leaves the room with an upward direction. In the inlet room below the main jet a recirculation zone is visible. On the top of the inlet room, near the inlet wall, low velocities are visible. From this point the flow accelerates with a downward direction joining the main jet, passing through the opening door, and is also directed to the partition wall. When it is close to the wall it reduces its velocity and is directed downward passing through the top of the opening with really low velocities. After the opening, this flow is directed to the top of the building where really low velocities are found once again. On the top of the second room, closer to the outlet wall a recirculation zone is found.

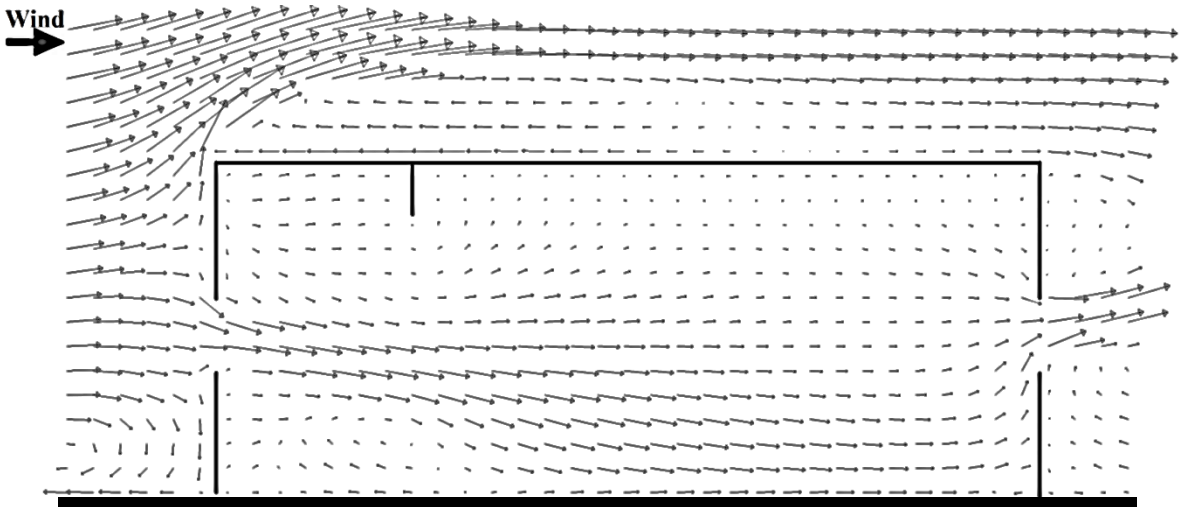

Figure 57 Velocity vector field on the vertical mid-plane of the 2.5 H building depth with a door near the inlet of the building.

In Figure 58 the velocity vector field on the vertical mid-plane is represented. It is visible that the flow in the first room is symmetric while in the second is asymmetric. When the air enters through the inlet window it travels in the leeward direction. At the partition, part of the flow flushes through the opening, while other part strikes against the wall and is directed to the sides, where two recirculation zones are created. After the opening door, the flow flushes in the outlet direction although slightly directed to the left side of the building. On the left side, closer to the wall, is visible a big recirculation zone with low velocities. Just on the right side, where the flow is steered to the left, a recirculation zone is formed. Further to the right, closer to the left side wall, even lower velocities are seen. After outlet opening, the flow is flushed with higher velocities to the right side of the building. While on the left side, just after the opening, a small recirculation zone is visible.

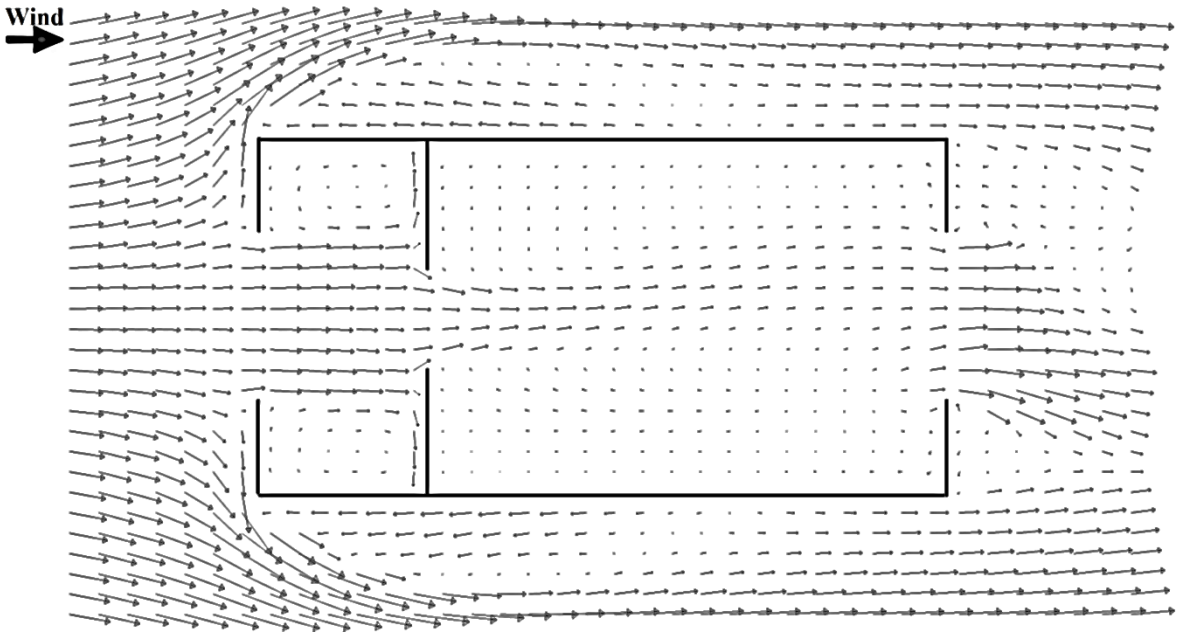

Figure 58 Velocity vector field on the horizontal mid-plane (h = 1.2 m) of the 2.5 H building depth with a door near the inlet of the building.

On the inlet opening a volume flow rate of 0.517 $m^3 s^{-1}$ was registered, corresponding to a total air exchange rate of 47 ACH. The average mean age of air in the inlet room was 38.0 s, in the outlet room was 81.4 s and in the building 70.8 s. The area-weighted average registered on outlet opening was 70.7 s, hence the air exchange efficiency of the building was 49.9%. The average CO_2 concentration recorded was 418 ppm, 437 ppm and 432 ppm, for the inlet room, outlet room and for the whole building, respectively. The maximum concentration value was 527 ppm, which was substantially higher than the values found for the other cases with this building depth. For this reason in Figure 59 the range of the color map is different from the other four cases with this building depth. It can be seen that the lowest concentration values are on the center plane at mid-height of the building just after the inlet opening (Figure 59e,f) and the highest are found in the outlet room on right side close to the partition wall near the ground plane (Figure 59d). It is possible to observe the symmetry of the concentration on the first room and the asymmetry on the second room, explained by the different flow patterns existent in the two rooms. In the first room, the highest concentration values are found on the top of the room. In the second, near the top, the CO_2 concentration is in general higher than in the rest of the building (Figure 59g). Although, the highest concentration values are found on the bottom right corner near the partition wall.

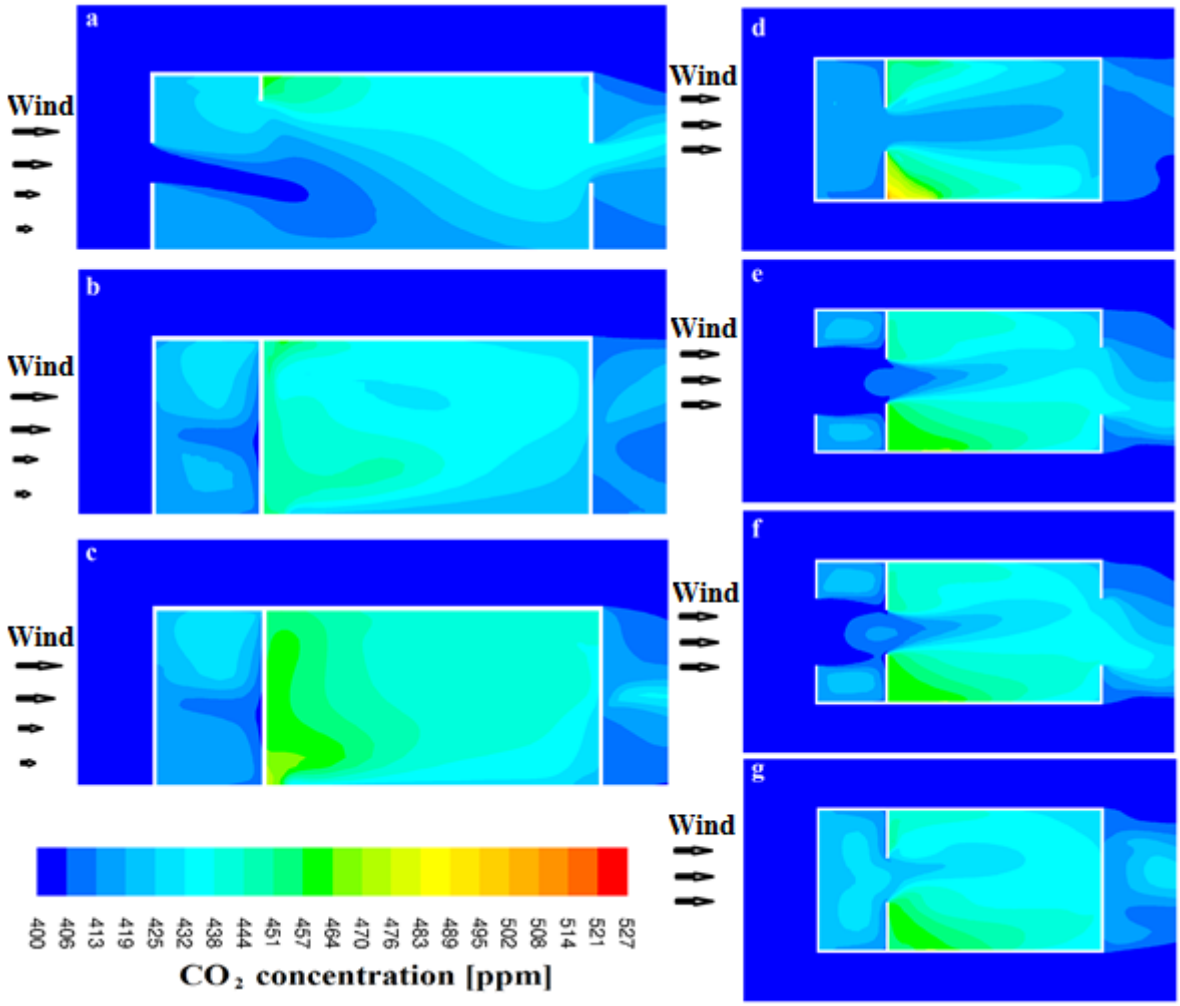

Figure 59 CO_2 concentration on the 2.5 H building depth with a door near the inlet of the building: (a) Vertical center mid-plane; (b) Vertical left-plane (0.75 m to the left of the mid-plane); (c) Vertical right-plane (0.75 m to the right of the mid-plane); (d) Horizontal 0.1 m plane; (e) Horizontal 1.1 m plane; (f) Horizontal mid-plane (1.2 m); (g) Horizontal 1.7 m plane.

6.3.2.3. Door opening near the left side wall

In Figure 60 the velocity vector field on the vertical mid-plane of the building is shown. It can be seen that the flow enters the opening and is accelerated with a downward direction till the center of this room. It then starts to decelerate till it reaches the partition wall where it is divided. Part of the flow is directed upwards creating a big recirculation zone over the jet entering the room, and the other part is directed to ground surface where a recirculation zone is formed bellow the main jet. The flow patterns observed in this first room are identical to the ones observed on the corresponding case with standard building depth. In the outlet room near ground and close to the outlet wall a small recirculation zone can be seen. Over this it is visible a small zone with low velocities. From this point the flow accelerates and is directed into different directions. Part of it is directed upwards in the direction of the outlet opening and the other part flows in the direction of the partition wall. When it reaches the partition wall it is directed upwards and circulated all over

the room being directed to the outlet opening. It is still observed a small recirculation zone close to the ceiling.

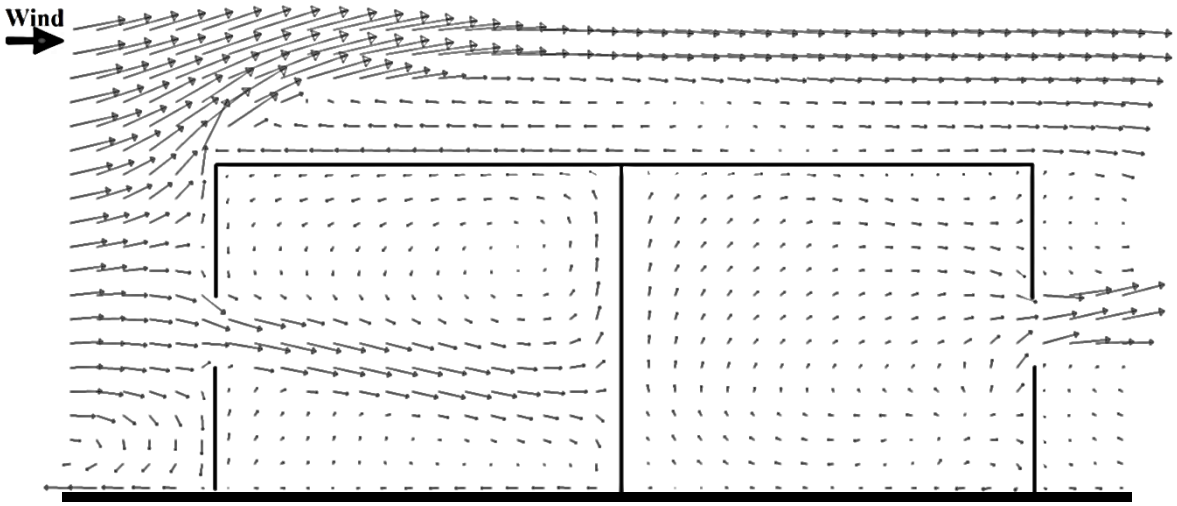

Figure 60 Velocity vector field on the vertical mid-plane of the 2.5 H building depth with a door near the left side wall.

In Figure 61 is represented the velocity vector field on the horizontal mid-plane of the building. The flow enters through the inlet opening and is directed to the partition wall. When it reaches the partition, part of the flow is directed to the right side of the building where a recirculation zone is formed and the other part flushes to the left side leaving the room through the door opening. On the right side of the inlet opening higher velocities are observed and on the left side just after the inlet opening a small recirculation zone can be seen. This recirculation causes the flow to flush with lower velocities and close to the left side wall. When the flow passes to the outlet room it is accelerated and tend to the left side of the building, flushing close to the side wall in the direction of the leeward opening. On the center-right of the second room a big recirculation zone can be seen. A small recirculation zone can also be seen on the left side of the second room just after the door opening. When the flow leaves the room is flushes with higher velocities to the right side of the building.

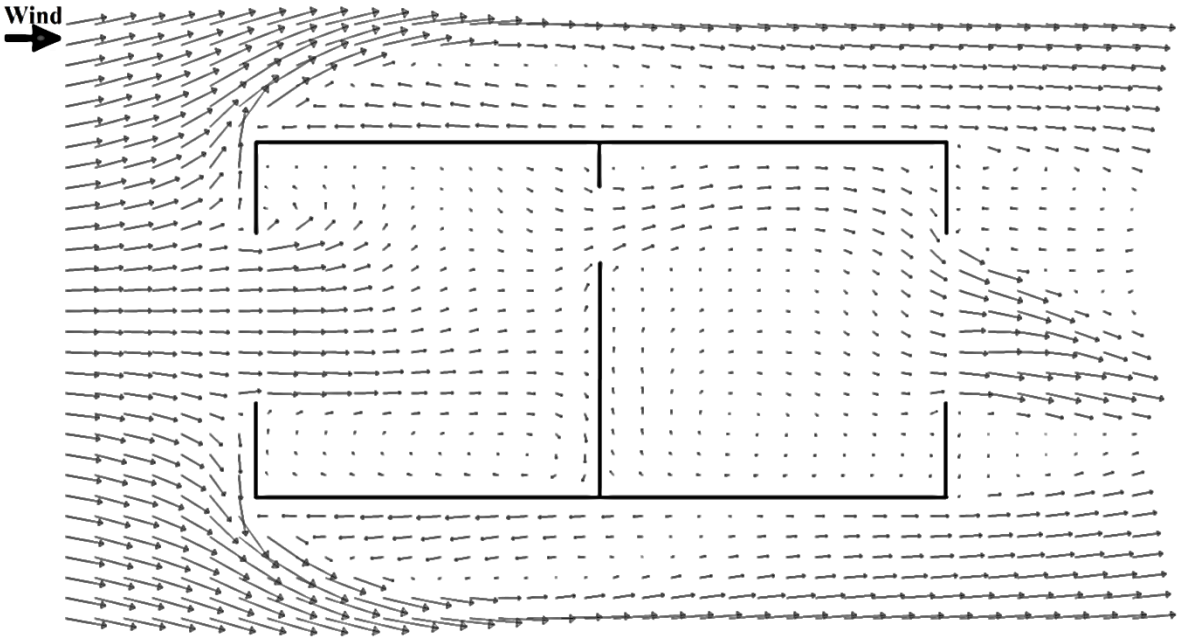

Figure 61 Velocity vector field on the horizontal mid-plane (h = 1.2 m) of the 2.5 H building depth with a door near the inlet of the building.

On the inlet opening a volume flow rate of 0.504 $m^3 s^{-1}$ was registered leading to an air exchange rate of 46.1 ACH. The average mean age of air in the inlet room was 41.1 s, in the outlet room 78.6 s and in the entire building 59.8 s. The area-weighted average in the outlet opening was 72.2 s, thus the air exchange efficiency was 60.8%. The average CO_2 concentration in the inlet room was 419 ppm, 435 ppm in the outlet room and 427 ppm in the whole building. The maximum concentration value registered was 455 ppm. The CO_2 concentration in different planes of the building can be seen in Figure 62. It can be seen that on the center and on the right side of the building higher concentrations are present. The lowest concentrations are found just after the inlet opening at mid-height and on the left side of the building where the door opening is present. The flow entering in the inlet opening has a higher depth of penetration, entering by the right side of the opening compared to the one entering by the left side. In the inlet room the lowest values are found before the door opening on the left side of the building. It is interesting to notice that the highest values are found just in front of the outlet opening at mid-height of the building (Figure 62e,f).

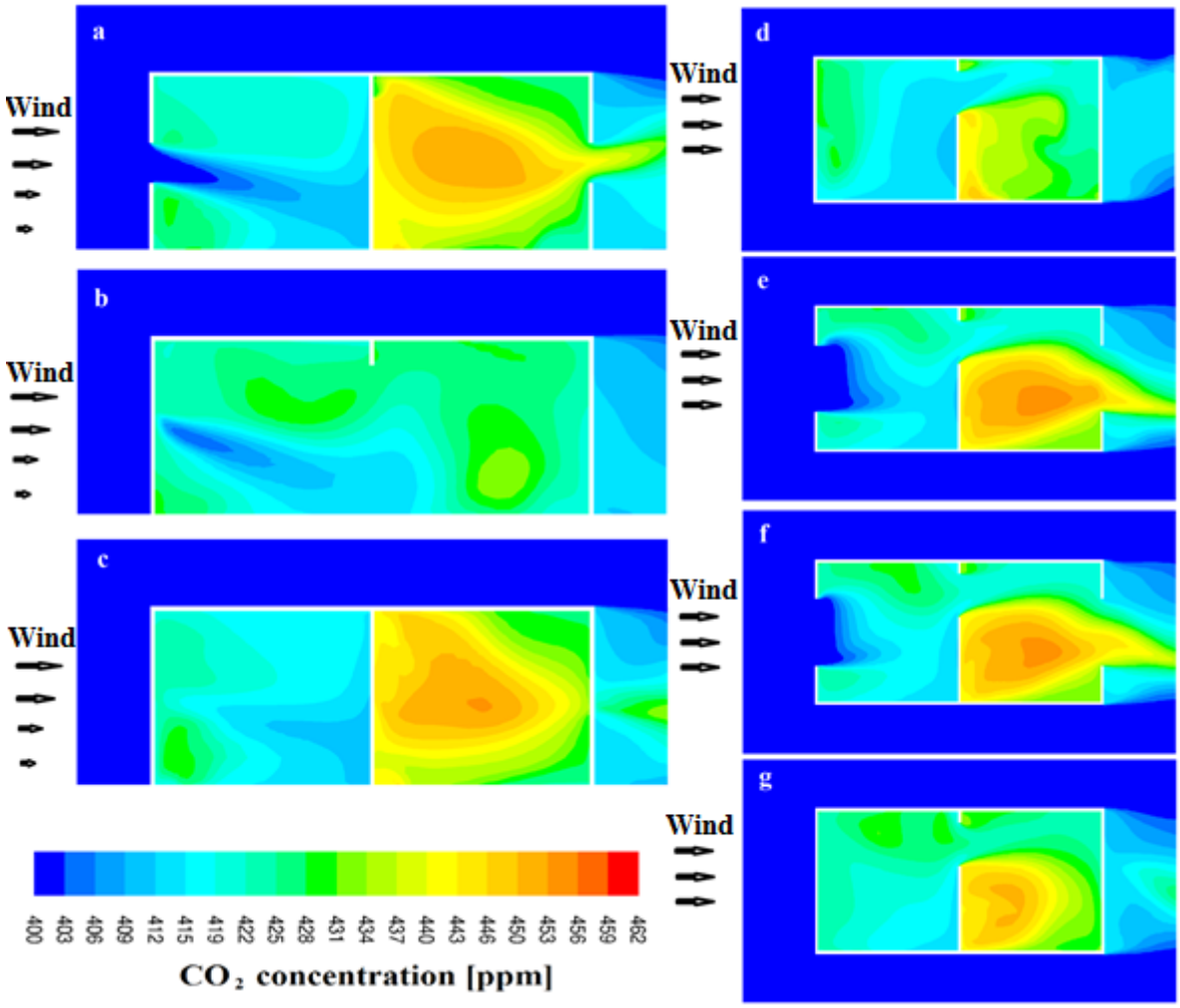

Figure 62 CO_2 concentration on the 2.5 H building depth with a door near the left side wall: (a) Vertical center mid-plane; (b) Vertical left-plane (0.75 m to the left of the mid-plane); (c) Vertical right-plane (0.75 m to the right of the mid-plane); (d) Horizontal 0.1 m plane; (e) Horizontal 1.1 m plane; (f) Horizontal mid-plane (1.2 m); (g) Horizontal 1.7 m plane.

6.3.3. Discussion and conclusions

Four different building configurations for two different building depths were simulated and a resume of the results obtained during the post processing of the simulations can be seen in Table 8. Different results were obtained for the two different building depths. The maximum space-averaged mean age of air was obtained for the case with the door in the center on the standard building depth and for the case with the door near the inlet opening on the 2.5 *H* building depth. The simple case on the two different depths obtained the second highest mean age of air value. The second minimum value was obtained for the case with the door near the inlet opening on the standard building depth and for the case with the door in the center on the 2.5 *H* building depth. The minimum mean age of air was found for the same case for the two different depths, being this minimum values registered for the cases with the door opening on the side of the building. The air exchange efficiency and the average CO_2 concentration results followed the same pattern of the mean age of air results. It is interesting to notice that the buildings with the door opening on the

side were the ones with the lowest volume flow rate of the four different configurations, despite having better performance results concerning the mean age of air, air exchange efficiency and average CO_2 concentration. The highest volume flow rate was recorded for the door opening in the center of the building on the standard building depth, which is the case with the lowest performance results. The CO_2 concentration and the air exchange rate for the different cases are represented in Figure 63.

Regarding the flow patterns observed in the building, it is visible that different patterns exist for the same configurations with different building depths. In the standard building depth, the flow is symmetric on the vertical mid-plane for the first three cases. In the 2.5 *H* building depth, the flow is asymmetric for all the four cases, although the flow is symmetric in the second room for the case with the door in the center and in the first room for the case with the door near the inlet opening. The asymmetry visible in the different cases can be caused by the oscillatory behavior of the flow (seen in the residuals) and if the results were collected at a different iteration, the results could have been different. In future studies, averaging of the results in such cases is highly recommended. The highest values of CO_2 are found in different parts of the building depending on the case and on the building depth. In the simple case of the standard building depth, the highest values are found on the top left of the building. In the case with the door in the center of the building, the highest values are found on the sides near the outlet opening and at the top of the building. In the case with the door near the inlet opening, the highest values are found on the left side near the outlet wall and on the top of the building. In the case with the door on the side it is found on the right side (opposite to the door opening) near the top and ground of the building. In the 2.5 *H* building depth, in the simple case it is found on the left side near the inlet wall at the top and at the bottom of the building. In the case with the door in the center it is found in the second room on the left side at the ground level and near the partition wall. In the case with door near the inlet opening the highest values are also found on the second room near the ground and close to the partition wall but on the right side of the building. In this case it is important to note that the maximum CO_2 value was much higher than in the other cases. Finally, in the case with the door on the side of the building the highest values are found on the center-right at mid-height of the building. The local maximum and the average CO_2 concentrations can be seen in Figure 64. It can be noticed that for the standard building depth the highest local concentration value is found on the same case in which the lowest average concentration value is found (door on the side of the building). For the cases with the building depth equal to 2.5 times the building height the lowest local value and lowest average value are found for the case with the door opening on the side. On the other hand, the maximum values are both found on the case with the door opening close to the inlet wall.

According to the results presented it is important to note the fact that the volume flow rate has a reduced impact on the ventilation performance of the building. It can be seen by the fact that the lowest volume flow rate gave the best performance results (door on the side in both depths) and due to the fact that the highest volume flow rate value gave the worst results (standard building with door in the center). It can also be seen that a case that performs good at one of the indicators

(mean age of air, air exchange efficiency and CO_2 concentration) also has a good performance at the others. The cases with the door on the sides have really good results due to the higher mixing of the exterior and interior air compared to the other cases. This can be seen by the really good results obtained in the inlet room (almost similar to the ones obtained for the case with the door near the inlet opening, which has half of the volume). As expected, the highest concentration values are found on the outlet room, although in different parts of the room. They are mainly found on the top of the building and the highest concentrations tend to be close to a surface, where recirculation zones exist and where the flow gets trapped.

Table 8 Mean age of air, air exchange efficiency, CO_2 concentration, volume flow rate and air exchange rate of the different building configurations.

			Mean Age of air [s]	Air exchange efficiency [%]	CO_2 [ppm]	Volume flow rate [$m^3 s^{-1}$]	Air exchange rate [ACH]
Standard	Simple		34.4	50%	415	0.539	100
	Door	Center	36.7	45%	416	0.560	105
		Inlet	30.5	55%	414	0.557	105
		Side	29.7	60%	413	0.514	97
2.5 H	Simple		68.1	51%	431	0.528	48
	Door	Center	64.4	55%	429	0.523	48
		Inlet	70.8	50%	432	0.517	47
		Side	59.8	61%	427	0.504	46

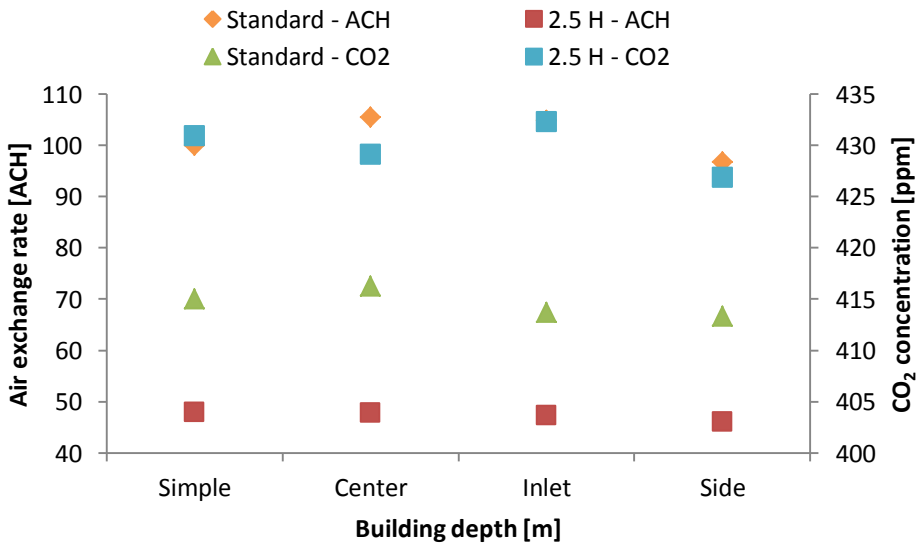

Figure 63 Air exchange rate and average CO_2 concentration of the different building configurations.

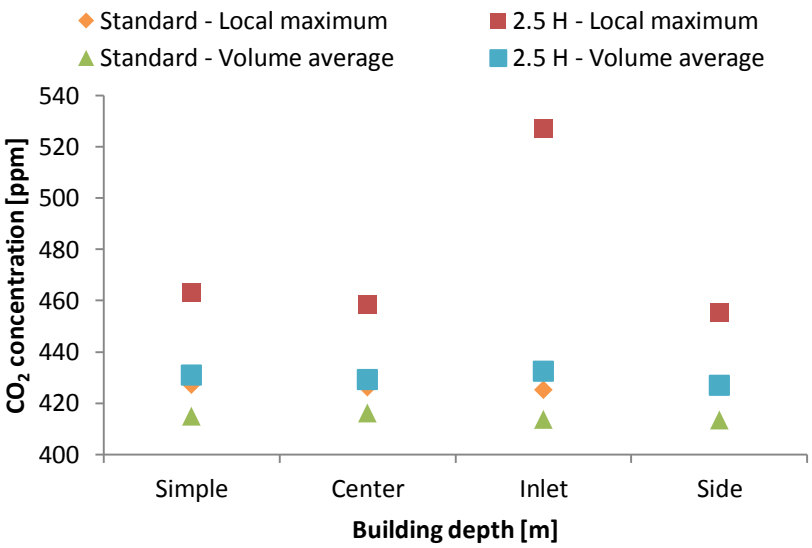

Figure 64 Local maximum and volume average CO_2 concentration for of the different building configurations.

7. Conclusions and recommendations

In the present work different building geometries were tested to better understand how cross-ventilation is affected. To do so four different building depths and four different building geometries were tested. To evaluate the performance of the different buildings the volume flow rate through the inlet window, the mean age of air and the CO_2 concentration inside the building were collected and through it the air exchange rate and the air exchange efficiency were assessed.

Firstly, a validation study was performed to ensure that the computational domain and grid resolution, the boundary conditions and the computational parameters and settings were correctly chosen. The results obtained were compared with the wind tunnel PIV experiments performed by (Karava 2008; Karava et al. 2011) and due to the existence of a good match between those two the numerical model was validated. The model used during the validation study was then used to perform the simulations of the different building geometries.

The second part of the numeral analysis was the simulation of the different building geometries, in a real scale and with a reduced wind velocity compared to the one used during the validation study. Initially the depth of the building was constantly increased to twice the previous one. Four different building depths were analyzed: standard (equal to the one used in the validation study), 2.5, 5 and 10 times the building height. The results obtained for the standard building depth were similar to the ones obtained in the validation study, despite the fact that both the computational domain and wind profile were scaled. Therefore, these scaling was correctly done. The volume flow rate was very similar for the four cases and consequently the air exchange rate decreased proportionally with the increasing depth. The mean age of air and the CO_2 concentration values increased with the increasing depth although at a smaller rate. For this reason the air exchange efficiency was higher in the deepest buildings. The flow patterns were different from case to case as was seen in the velocity vector fields. The only constant characteristics were the downward direction of the flow after it passes the inlet opening (caused by the existence of a standing vortex near the ground on the outside of the building, which is visible in all the cases) and the upwards direction of the flow after it leaves the building (due to the existence of a recirculation zone on the wake region of the building). In the two smallest building depths the highest concentrations values are found close to the inlet façade, while in the two biggest it is found near the leeward façade. From the results obtained it can be concluded that cross-ventilation is still effective in a building with a building depth equal to ten times the building height, at least in this particular case.

Subsequently three new geometries were tested. These geometries had a partition with a door opening dividing the building in two different rooms. The first geometry had a door in the center of the building. The second had the partition and the door opening on the center of the inlet plane but was located between the first and second quartiles of the building depth. The third one had the door on the left side of the building, with its center between the first and second quartiles, starting from the left side wall. For each of these geometries two different building depths were tested: the standard depth and the depth equal to 2.5 times the building height. Different results were obtained for the two different depths. Although, the case with door on the side of the building outperformed the other three cases (the cases with a partition and the case without

partition) in both building depths. The door on the side cases had the lowest values of mean age of air, CO_2 concentration and volume flow rate, consequently having the lowest values of air exchange efficiency and air exchange rate. The cases with the worst performances were the door in the center for the standard building depth and the door near the inlet opening for the 2.5 *H* building depth. The flow patterns were different from case to case, with the exception of the two characteristics pointed out in the previous paragraph. Unlike the cases without any partition, the highest CO_2 concentrations were found on the second room (closer to the outlet façade) in all the cases.

Concluding, the existence of a limit of 5 *H* for cross-ventilation (Awbi 2003) was not verified for this particular case, as can be seen by the results obtained by the 5 *H* and 10 *H* building depths. Due to the fact that the volume flow rate stays relatively constant, the air exchange rate diminishes proportionally with the increasing building depth. For this reason, it is expected that at some building depth there will be a limit to the effectiveness of cross-ventilation. It is also important to notice that velocities over 1 m s^{-1} were registered inside the building and if lower velocities existed the impact of the building depth would probably increase. The existence of a partition dividing the building in two has a significant impact in the performance of cross-ventilation. The partition can cause the appearance of a zone with almost no air movement causing high pollutant concentrations in that zone or have the opposite impact leading to a better mixing of all the air inside the building. To a better performance of a building with partition, the door opening should be located on the sides of the building enabling a higher mixing of the interior air in both partitions. The volume flow rate in buildings with the same building depth but with different geometries seems to have no impact in the ventilation performance of the building. The zones where the highest velocities are found, in general, are the regions with the lowest concentration values. It can also be concluded that the different assessment parameters used had the same qualitative results.

In order to continue the present work, other geometries could be tested by changing the height and the length of the building and by changing the window opening areas and positions in the partitioned buildings. It could be interesting to introduce obstacles inside the building in order to better simulate a working/living environment. The introduction of the buoyance effect, by changing the internal and external temperatures, in the computational model, should also be considered in future work. Different wind profiles could be tested to better understand the effect of reduced velocities on the performance of cross-ventilated buildings. A sensitivity study on the impact of the oscillations of the flow field (seen in the residuals) on the vector fields and CO_2 concentration presented in this thesis should also be performed. Lastly, the influence of surrounding buildings on the ventilation flow should be assessed.

8. References

Alexander, D., Jenkins, H. & Jones, P., 1997. Investigating the effects of wind on natural ventilation design of commercial buildings. In *Proceedings, Sustainable Building*. Abingdon, Oxfordshire, UK, pp. 141–148.

ANSI/ASHRAE, 2007. Standard 55. Thermal environmental conditions for human occupancy. In *American Society of Heating, Refrigeration, and Air Conditioning Engineers*. Atlanta, GA.

Ansys, I., 2009. ANSYS FLUENT theory guide. *Knowledge Creation Diffusion Utilization*, 15317, pp.724–746.

ASHRAE Standard 62-1999, 1999. Ventilation for acceptable indoor air quality. In *American Society of Heating, Refrigeration and Air-Conditioning Engineers*. Atlanta, GA.

Awbi, H., 2003. *Ventilation of buildings* 2nd editio., London: Taylor and Francis.

Balaras, C.A., Gaglia, A.G., Georgopoulou, E., Mirasgedis, S., Sarafidis, Y. & Lalas, D.P., 2007. European residential buildings and empirical assessment of the Hellenic building stock, energy consumption, emissions and potential energy savings. *Building and Environment*, 42, pp.1298–1314.

Bangalee, M.Z.I., Miau, J.J., Lin, S.Y. & Yang, J.H., 2013. Flow visualization, PIV measurement and CFD calculation for fluid-driven natural cross-ventilation in a scale model. *Energy and Buildings*, 66, pp.306–314.

Bartzanas, T., Kittas, C., Sapounas, A.A. & Nikita-Martzopoulou, C., 2007. Analysis of airflow through experimental rural buildings: Sensitivity to turbulence models. *Biosystems Engineering*, 97, pp.229–239.

Beranek, W.J. & Van Koten, H., 1979. Beperken van windhinder om gebouwen, deel 1. *Stichting Bouwresearch no. 65*.

Blocken, B., 2014. *CFD in building engineering: Fundamentals and applications in urban physics and wind engineering. Course book* Version 3., Eindhoven.

Blocken, B., Carmeliet, J. & Stathopoulos, T., 2007. CFD evaluation of wind speed conditions in passages between parallel buildings - Effect of wall-function roughness modifications for the atmospheric boundary layer flow. *Journal of Wind Engineering and Industrial Aerodynamics*, 95, pp.941–962.

Blocken, B., Stathopoulos, T. & Carmeliet, J., 2007. CFD simulation of the atmospheric boundary layer: wall function problems. *Atmospheric Environment*, 41(2), pp.238–252.

BPIE, 2011. *Europe's buildings under the microscope, A country-by-country review of the energy performance of buildings*, Brussels.

Carrilho da Graça, G. & Linden, P.F., 2003. Simplified modelling of cross-ventilation airflow. *ASHRAE Transactions*, 109(1), pp.4605–4619.

Cebeci, T. & Bradshaw, P., 1977. *Momentum transfer in boundary layers.*, New York: Hemisphere Publising Corp.

Chen, Q., 2009. Ventilation performance prediction for buildings: A method overview and recent applications. *Building and Environment*, 44(4), pp.848–858.

Chu, C.-R. & Chiang, B.-F., 2013. Wind-driven cross ventilation with internal obstacles. *Energy and Buildings*, 67, pp.201–209.

Chu, C.R., Chiu, Y.-H. & Wang, Y.-W., 2010. An experimental study of wind-driven cross ventilation in partitioned buildings. *Energy and Buildings*, 42(5), pp.667–673.

Etheridge, D. & Sandberg, M., 1996. *Building ventilation: theory and measurement*, Chichester: John Wiley & Sons.

Evola, G. & Popov, V., 2006. Computational analysis of wind driven natural ventilation in buildings. *Energy and Buildings*, 38, pp.491–501.

Fanger, P.O., Lauridsen, J., Bluyssen, P. & Clausen, G., 1988. Air pollution sources in offices and assembly halls, quantified by the olf unit. *Energy and Buildings*, 12, pp.7–19.

Franke, J., Hellsten;, A., Schlünzen;, H. & Carissimo, B., 2007. *Best Practice guideline for the CFD simulation of flows in the urban environment.*, Brussels: COST Office.

Gan, G., 2000. Effective depth of fresh air distribution in rooms with single-sided natural ventilation. *Energy and Buildings*, 31(1), pp.65–73.

Hang, J. & Li, Y., 2011. Age of air and air exchange efficiency in high-rise urban areas and its link to pollutant dilution. *Atmospheric Environment*, 45(31), pp.5572–5585.

Hang, J., Sandberg, M. & Li, Y., 2009. Age of air and air exchange efficiency in idealized city models. *Building and Environment*, 44(8), pp.1714–1723.

Van Hooff, T., 2012. *Experimental and numerical analysis of mixing ventilation at laminar , transitional and turbulent slot Reynolds numbers*. PhD Thesis: Eindhoven University of Technology and Katholieke Universiteit Leuven.

Van Hooff, T. & Blocken, B., 2010. Coupled urban wind flow and indoor natural ventilation modelling on a high-resolution grid: A case study for the Amsterdam ArenA stadium. *Environmental Modelling and Software*, 25(1), pp.51–65.

Van Hooff, T., Blocken, B., Aanen, L. & Bronsema, B., 2011. A venturi-shaped roof for wind-induced natural ventilation of buildings: Wind tunnel and CFD evaluation of different design configurations. *Building and Environment*, 46(9), pp.1797–1807.

Jiang, Y., Alexander, D., Jenkins, H., Arthur, R. & Chen, Q., 2003. Natural ventilation in buildings: measurement in a wind tunnel and numerical simulation with large-eddy simulation. *Journal of Wind Engineering and Industrial Aerodynamics*, 91(3), pp.331–353.

Karava, P., 2008. *Airflow Prediction in Buildings for Natural Ventilation Design: Wind Tunnel Measurements and Simulation*. Concordia University Montreal, Quebec, Canada.

Karava, P., Stathopoulos, T. & Athienitis, A.K., 2011. Airflow assessment in cross-ventilated buildings with operable façade elements. *Building and Environment*, 46(1), pp.266–279.

Kobayashi, T., Sagara, K., Yamanaka, T., Kotani , H., Takeda, S. & Sandberg, M., 2009. Stream tube based analysis of problems in prediction of cross-ventilation rate. *Int J Vent*, 7, pp.321–24.

Launder, B.E. & Spalding, D.B., 1974. The numerical computation of turbulent flows. *Computer Methods in Applied Mechanics and Engineering*, 3, pp.269–289.

Meiss, A., Feijó-Muñoz, J. & García-Fuentes, M. a., 2013. Age-of-the-air in rooms according to the environmental condition of temperature: A case study. *Energy and Buildings*, 67, pp.88–96.

Mistriotis, A., Bot, G.P.A., Picuno, P. & Scarascia-Mugnozza, G., 1997. Analysis of the efficiency of greenhouse ventilation using computational fluid dynamics. *Agricultural and Forest Meteorology*, 85, pp.217–228.

NEN 1824:2010, 2010. Ergonomic Requirements For The Surface Of (Workplaces In) Administration And Office Spaces.

Novoselac, A. & Srebric, J., 2003. Comparison of air exchange efficiency and contaminant removal effectiveness as IAQ indices. *TRANSACTIONS-AMERICAN SOCIETY …*, 109(4663), pp.1–11.

Ramponi, R. & Blocken, B., 2012a. CFD simulation of cross-ventilation flow for different isolated building configurations: Validation with wind tunnel measurements and analysis of physical and numerical diffusion effects. *Journal of Wind Engineering and Industrial Aerodynamics*, 104-106, pp.408–418.

Ramponi, R. & Blocken, B., 2012b. CFD simulation of cross-ventilation for a generic isolated building: Impact of computational parameters. *Building and Environment*, 53, pp.34–48.

Robertson, A., Burge, P. & Hedge, A., 1985. Comparison of health problems related to work and environmental measurements in two office buildings with different ventilation systems. *Br. Med. J*, 291, pp.373–6.

Sandberg, M., 1981. What is ventilation efficiency? *Building and Environment*, 16, pp.123–135.

Spindler, H.C. & Norford, L.K., 2009. Naturally ventilated and mixed-mode buildings-Part II: Optimal control. *Building and Environment*, 44, pp.750–761.

Stathopoulos, T., 1984. Design and fabrication of a wind tunnel for building aerodynamics. *Journal of Wind Engineering and Industrial Aerodynamics*, 16, pp.361–376.

Sundell, J., 1982. Guidelines for Nordic building regulations regarding indoor air quality. *Environment International*, 8, pp.17–20.

Tominaga, Y., Mochida, A., Yoshie, R., Kataoka, H., Nozu, T., Yoshikawa, M. & Shirasawa, T., 2008. AIJ guidelines for practical applications of CFD to pedestrian wind environment around buildings. *Journal of Wind Engineering and Industrial Aerodynamics*, 96(10-11), pp.1749–1761.

Tzempelikos, A., Athienitis, A.K. & Karava, P., 2007. Simulation of façade and envelope design options for a new institutional building. *Solar Energy*, 81, pp.1088–1103.